Screen-printed aluminum-doped p^+ emitters for the application to n-type silicon solar cells

Von der Fakultät für Mathematik und Physik
der Gottfried Wilhelm Leibniz Universität Hannover
zur Erlangung des Grades

Doktor der Naturwissenschaften

Dr. rer. nat.

genehmigte Dissertation

von

Dipl.-Ing. Robert Bock

geboren am 01.01.1977 in Loben

2011

Referent: Prof. Dr. Jan Schmidt
Korreferent: Prof. Dr. Rolf Haug
Tag der Promotion: 12.05.2011

Abstract

This work focuses on the characterization of electrical and morphological properties of screen-printed Al-p^+ regions. Furthermore, this work demonstrates for the first time surface passivation of screen-printed highly aluminum-doped p^+ regions and its application as rear emitter to n-type silicon solar cells.

The origin of a hitherto unexplained apparent concentration peak which is typically measured at the surface of aluminum-doped p^+ regions is investigated. The structural investigations of this work provide clear experimental evidence that the concentration peak is due to the microscopic structures formed on the silicon surface during the firing process. To characterize the microscopic nature of the islands and line networks of self-assembled nanostructures several electron microscopy methods are combined. Aluminum inclusions are detected near to the surface of the islands and crystalline aluminum nano-precipitates are found within the bulk of the islands. In addition, aluminum inclusions are found within the bulk of the self-assembled line networks. The obtained results reveal that these Al inclusions are the cause for the apparent concentration peak.

Internal quantum efficiency measurements on specially designed test structures show that recombination lifetimes measured on Al-p^+ regions fabricated by means of screen-printing and firing are three orders of magnitude larger than the lifetimes expected from the extrapolation of the lifetime data measured on aluminum-doped Czochralski-grown silicon wafers. These results prove that the efficiency potential of screen-printed Al-p^+ emitters for the application to rear-junction n-type silicon solar cells is much higher than it was traditionally assumed.

It is found that the lifetime in highly aluminum-doped silicon regions experiences a pronounced degradation during thermal treatment at temperatures above 850°C. The defect formation is shown to be directly linked to the simultaneous presence of oxygen and aluminum and thus it can be attributed to the formation of aluminum-oxygen complexes. Temperature-dependent measurements of the defect generation rate provide evidence that the formation of the Al-O complex is thermally activated.

For the first time aluminum-doped p^+ emitters fabricated by means of screen-printing and firing are effectively passivated by amorphous silicon (a-Si), aluminum oxide (Al_2O_3), and thermally grown silicon dioxide (SiO_2) as well as Al_2O_3/SiN_x stacks. The applied surface passivation to the p^+ emitter reduces the saturation current density by a factor of 3-4. Moreover, the Al_2O_3 as well as the Al_2O_3/SiN_x stacks show an excellent firing stability and hence are suited for the implementation into an industrial solar cell process.

In addition to the characterization and passivation of the Al-p^+ emitter, this work presents a successful technological implementation of the developed passivated Al-p^+ emitter into an n^+np^+ solar cell structure, the so-called ALU$^+$ solar cell. An independently confirmed conversion efficiency of 20% is achieved with this solar cell, clearly demonstrating the high-efficiency potential of the ALU$^+$ cell concept. The applicability of this easy-to-fabricate p^+ emitter to a back-junction back-contact solar cell is demonstrated where an energy conversion efficiency of 19.0% is achieved. A realistic efficiency limit of 21.6% is determined for this novel cell type using two-dimensional device simulation. Finally, two types of industrial-type large-area *n*-type Cz-Si solar cells with an Al-p^+ emitter at the rear are introduced, one featuring a selective front surface field and a second featuring a screen-printed and passivated Al-p^+ emitter at the rear.

The results of this work suggest that the quality of a screen-printed Al-p^+ emitter and the efficiency potential of screen-printed solar cells on *n*-type silicon have been strongly underestimated in the past and that the screen-printed Al-p^+ emitter is a competitive alternative to the high-temperature boron diffusion.

Kurzzusammenfassung

Das Thema dieser Arbeit ist die Charakterisierung der elektrischen und morphologischen Eigenschaften von siebgedruckten Al-p^+ Gebieten. Ferner demonstriert die vorliegende Arbeit erstmalig die Oberflächenpassivierung von hochdotierten siebgedruckten Al-p^+ Gebieten und ihre Anwendung als Emitter auf n-Typ Siliciumsolarzellen.

Im Rahmen dieser Arbeit wird eine vor der Arbeit ungeklärte scheinbare oberflächennahe Al-Konzentrationserhöhung in gemessenen Dotierprofilen von siebgedruckten Al-p^+ Gebieten untersucht. Die Ergebnisse der strukturellen Untersuchungen liefern experimentelle Anhaltspunkte, dass charakteristische Oberflächeninseln, welche während des Feuerprozesses gebildet werden, die Ursache für die scheinbare Al-Konzentrationserhöhung darstellen. Um die mikroskopischen Eigenschaften der Oberflächeninseln sowie der gefundenen selbstorganisierten linienartigen Nanostrukturen zu charakterisieren, werden unterschiedliche elektronenmikroskopische Verfahren angewendet und kombiniert. Im Ergebnis werden oberflächennahe Aluminiumeinschlüsse sowie nanometergroße kristalline Aluminiumausscheidungen im Volumen der Oberflächeninseln detektiert.

Zusätzlich zu diesem Befund werden auch Aluminiumeinschlüsse im Volumen der selbstorganisierten linienartigen Nanostrukturen gefunden. Die experimentellen Resultate dieser Untersuchungen zeigen, dass die gefundenen Al-Einschlüsse die Ursache der scheinbaren Konzentrationserhöhung in den Dotierprofilen der siebgedruckten Al-p^+-Gebiete sind.

Messungen der internen Quantenausbeute von speziell hergestellten Probenstrukturen zeigen, dass die Ladungsträgerlebensdauer in siebgedruckten und gefeuerten Al-p^+ Gebieten drei Größenordnungen höher ist, als die in aluminiumdotiertem und im Czochralski-Verfahren hergestelltem Silicium. Unsere Ergebnisse zeigen, dass das Wirkungsgradpotential der siebgedruckten Al-p^+ Emitter für die Anwendung als Rückseitenemitter auf n-Typ Silicium-Material deutlich höher ist als bislang vermutet wurde.

Weiterhin zeigt sich, dass die Ladungsträgerlebensdauer eines siebgedruckten Al-p^+ Emitters bei Temperaturen oberhalb von 850°C stark degradiert. Ein gleichzeitiges Vorliegen von Sauerstoff und Aluminium im Material hat sich als besonders förderlich für die Degradation der Lebensdauer herausgestellt. Dieses Ergebnis führt zu der Modellvorstellung, dass rekombinationsaktive Al-O Komplexe gebildet werden. Aus temperaturabhängigen Messungen der Defektgenerationsrate wird geschlossen, dass der Bildungsmechanismus der Al-O Komplexe thermisch aktiviert ist.

In dieser Arbeit werden aluminiumdotierte siebgedruckte p^+-Emitter erstmalig erfolgreich mit amorphem Silicium (a-Si), Aluminiumoxid (Al_2O_3), thermisch gewachsenem Siliciumdioxid - (SiO_2) sowie mit Al_2O_3/SiN_x-Doppelschichten passiviert. Durch die Oberflächenpassivierung wird die Sperrsättigungsstromdichte der p^+-Emitter um den Faktor 3-4 verringert. Ferner zeigen Al_2O_3 und Al_2O_3/SiN_x-Doppelschichten eine sehr gute Feuerstabilität und eignen sich damit gut für eine Implementierung in einen industriellen Solarzellenprozess.

Die in dieser Arbeit entwickelten siebgedruckten und passivierten Al-p^+-Emitter werden erstmals in eine n^+np^+ Solarzellenstruktur implementiert, was zu einem unabhängig bestätigten

Wirkungsgrad von 20% führt. Auch die Eignung des siebgedruckten und passivierten Al-p^+-Gebietes als Emitter in einer rückseitenkontaktierten Solarzelle wird erstmals demonstriert, wobei ein Wirkungsgrad von 19% erreicht wird. Zweidimensionale Bauelementsimulationen liefern ein realistisches Wirkungsgradpotential von 21.6% für diese Rückseitenkontaktsolarzelle. Schließlich werden zwei industriehnahe großflächige n-Typ Solarzellen mit einem Al-p^+-Emitter auf der Zellrückseite präsentiert. Im ersten Solarzellentyp ist ein selektives Vorderseitenfeld implementiert und im zweiten ein siebgedruckter und passivierter Al-p^+-Emitter.

Die Ergebnisse dieser Arbeit zeigen, dass die Qualität von siebgedruckten Al-p^+ Emittern und das Wirkungsgradpotential von Siebdrucksolarzellen auf n-Typ Silicium bisher stark unterschätzt wurden und dass der siebgedruckte Al-p^+ Emitter eine gute Alternative zur Hochtemperatur-Bordiffusion ist.

Schlagwörter: Silizium, Siebdruck-Emitter, Oberflächenpassivierung
Keywords: silicon, screen-printed-emitter, surface passivation

Contents

Introduction

In today's mono crystalline silicon solar cell production lines boron-doped crystalline silicon (Si) material is predominantly used as base material since solar cell technology for *p*-type boron-doped silicon wafers is well established in industrial production. In particular, the simplicity of the phosphorus diffusion process for the *pn*-junction formation, which simultaneously acts as a gettering step, is a major driving force towards the usage of *p*-type silicon. During recent years, *n*-type silicon materials have moved into the focus of interest as they are promising candidates for future generations of high-efficiency Si solar cells. Switching form boron-doped *p*-type Czochralski-grown Si (Cz-Si) to phosphorus-doped *n*-type Cz-Si material has several advantages which have to be taken into consideration. *n*-type Cz-Si provides superior electrical properties over *p*-type Cz-Si. First, *n*-type Cz-Si has a much higher carrier lifetime than boron-doped *p*-Si material at the same level of metal impurity concentrations. The higher carrier lifetimes are mainly due to very asymmetric capture cross sections for electrons and holes, $\sigma_n > \sigma_p$, for frequent contaminants such as interstitial iron. Second, the carrier lifetime instability due to the formation of highly recombination-active boron-oxygen complexes under illumination, as known from single-crystalline boron-doped Cz-Si, is not an issue in *n*-type Cz-Si due to the negligible boron content.

Despite the huge advantages of *n*-type Cz-Si today only two companies, SunPower [1, 2] and Sanyo [3], use *n*-type Cz-Si wafers in their production lines. The main reason for this is the *pn*-junction formation on *n*-type Si material, where a p^+-region is required. In laboratory-type solar cells, this is typically done by a high-temperature boron diffusion. However, the high-temperature boron diffusion is technologically challenging as it can lead to a severe degradation of the electronic bulk properties of the Si due to defects which may be introduced during the high-temperature boron diffusion process. Thus, *n*-type Cz-Si plus a boron diffusion are still predominantly used in the lab.

During recent years, aluminum alloying has become a promising alternative for the p^+-emitter formation of *n*-type back-junction Si solar cells. This type of p^+-emitter formation is based on a simple screen-printing plus short firing process, which is well established solar cell technology as it is used for decades in industrial production lines for the formation of the back surface field (BSF) in *p*-type silicon solar cells.

A combination of these benefits, the high and stable carrier lifetimes of *n*-type Cz-Si material and the simple and cost effective screen-printing process for the junction formation, is very attractive for the production of industrially-feasible high-efficiency *n*-type silicon solar cells. This work focuses on the fundamental physical limitations of screen-printed Al-doped p^+ (Al-p^+) regions with respect to the applicability as rear emitter in n-type Si solar cells. In order to evaluate the applicability of the screen-printed Al-p^+ rear emitter to high-efficiency solar cells, the Al-p^+ emitter is passivated for the first time and it is applied to several types n-type Si solar cells.

Chapter 1 gives as a motivation and provides a review to state-of-the art n-type Si technologies. In detail, it presents the benefits of phosphorus-doped n-type over boron-doped p-type Czochralski-grown silicon material. An overview on common methods for the p^+ emitter formation is given. Finally, the main aspects of the fabrication and the basic physics behind the formation of the Al-p^+ region are described.

Chapter 2 deals with the characterization of electrical and morphological properties of the screen-printed Al-p^+ region. The origin of a concentration peak in doping profiles measured on screen-printed Al-p^+ regions is analyzed. The carrier lifetime in the bulk of the screen-printed Al-p^+-region is determined for the first time. As the carrier lifetime is limited by Al-O-related defects in the bulk in the Al-p^+ region, the formation kinetics of the Al-O complexes is examined.

Chapter 3 examines different methods for the surface passivation of screen-printed Al-p^+ regions. The successful passivation of the Al-p^+ region using plasma-enhanced chemical vapor deposited (PECVD) amorphous silicon (a-Si), PECVD silicon nitride (SiN_x), atomic layer deposited (ALD) aluminum oxide (Al_2O_3) and thermally grown silicon dioxide (SiO_2) is characterized by means of saturation current density measurements. Based on this experimental study, the potential of surface-passivated Al-p^+ emitters with regard to the application to n-type Si solar cells is assessed.

Chapter 4 describes the successful application of the optimized screen-printed and passivated Al-p^+ region as an emitter to several n-type silicon solar cell structures.

Chapter 5 summarizes this work. **Annex A** describes an improved evaluation method of the electrochemical capacitance voltage (**ECV**) technique which has been used for the measurement of doping profiles in this work.

1. Review of *n*-type Si technologies

In this work, the electrical and morphological properties of screen-printed aluminum-doped p^+ (Al-p^+) regions in crystalline silicon wafers are investigated. Furthermore, for the first time, the surface of a screen-printed Al-p^+ region is passivated and the passivation quality of several passivation methods such as amorphous silicon (a-Si), silicon nitride (SiN_x), thermally grown silicon dioxide (SiO_2) and aluminum oxide (Al_2O_3) is investigated by means of saturation current density measurements. Finally, the passivated and screen-printed Al-p^+ region is applied as emitter to the rear of *n*-type Si solar cells.

In order to motivate the topic of this work, the current Chapter gives an overview of the advantages of *n*-type over *p*-type Cz-Si material and of the main technologies for the formation of p^+ emitters on *n*-type silicon. On the basis of carrier lifetime measurments, Section 1.1 discusses why *n*-type Cz-Si is better suited for high-efficiency solar cells than conventional *p*-type Si. In Section 1.2, several approaches for the formation of a p^+-emitter on *n*-type Si are reviewed and compared: (i) the high-temperature boron diffusion, (ii) the a-Si:H/c-Si hetero-junction, and (iii) the screen-printed aluminum-doped p^+ region. As the screen-printed Al-p^+ region is the main topic of this work, the screen-printing process and the physics behind the formation of the Al-p^+ region are explained in detail in Section 1.2.3. The Chapter closes with a summary.

1.1. Czochralski-grown silicon: *n*-type vs. *p*-type

Today's Si solar cells are largely fabricated on boron-doped *p*-type silicon material [4–6], which is mainly due to the technological simplicity of the phosphorus diffusion process for the n^+ emitter formation. However, solar cells fabricated on boron-doped *p*-type silicon suffer from light-induced degradation due to the activation of a recombination-active boron-oxygen complex under illumination [7]. This in fact leads to a significant reduction in cell efficiency by 10% relative due to a reduced bulk carrier lifetime [7–11]. The following approaches for an effective suppression of light-induced degradation have been successfully tested in the past: (i) a reduction of the oxygen content in the boron-doped silicon by the magnetic-field-assisted Czochralski-growth technique (MCz-Si) [12–14], where the oxygen content is reduced by damping the melt flows with strong magnetic fields, (ii) a substitution of the dopant species boron by gallium, (iii) the deactivation of B-O complexes by additional anealing steps after solar cell processing [15, 16], and (iv) the use of phosphorus-doped *n*-type Si material instead of *p*-type boron-doped material.

Approach (i) leads to enhanced production costs as the manufacturing equipment has to be modified with additional equipment for the generation of very high magnetic fields. The energy consumption during crystal growth is also much higher. However, due to a reduced oxygen concentration, MCz-Si shows a nearly vanishing degradation effect and stable bulk lifetimes in the range of oxygen-lean high-purity float zone (FZ) Si. In approach (ii), where gallium is used as dopant instead of boron, the resistivity of the Cz-Si crystal varies widely over the length of the grown crystal. This is due to the smaller equilibrium segregation coefficient k_0 of Ga (k_0 = 0.008) compared to that of boron (k_0 = 0.7 - 0.8) [17]. Such a small segregation coefficient results in a low production yield of the Si crystal due to the specification of a limited resistivity range required by solar cell manufacturers. Approach (iii) is also related to additional costs as the finished solar cells have to be annealed for ∼15 minutes under illumination or even longer [15,16]. However, with this technique the degraded bulk lifetime can be regenerated up to its initial value. Approach (iv) is based on stable phosphorus-doped *n*-type Si material and thus it does not need additional equipment during crystal growth to suppress the B-O complex formation as it is inherently not present. The finished solar cells also do not need any post annealing steps to regenerate the bulk material. The segregation coefficient of phosphorus in Si of k_0 = 0.35 is not as high as that of boron in silicon but still much higher than that of gallium. This results in a much lower variation of the resistivity over the length of the grown crystal and thus, compared to gallium-doped Cz-Si, in a much higher production yield.

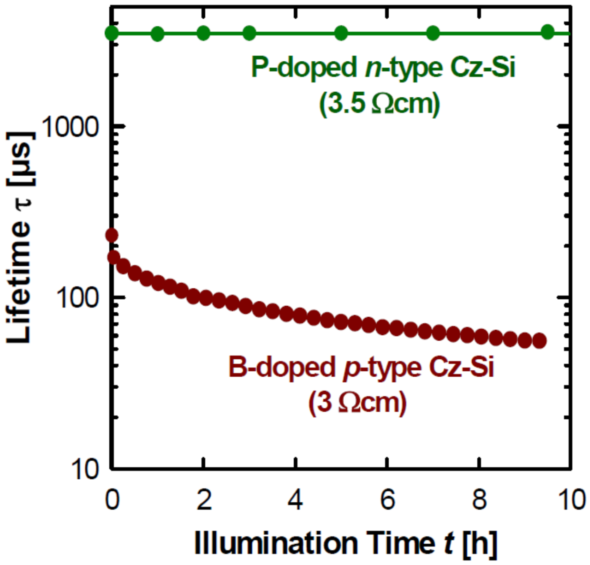

Figure 1.1.: *Measured lifetime of a boron-doped p- vs. a phosphorus-doped n-type Cz-Si wafer as a function of illumination time (halogen lamp, 100 mW/cm^2 intensity) [6].*

Phosphorus-doped *n*-type Cz-grown silicon material has also a clear advantage over boron-doped *p*-type Cz silicon material in terms of carrier lifetimes. Lifetimes measured on boron-doped *p*-type Cz-Si wafers are typically one to two orders of magnitude below that of phosphorus-doped *n*-type Cz-Si.

Figure 1.1 shows the measured lifetimes of a silicon-nitride-passivated *n*-type vs. that of a typical *p*-type Cz-Si wafer of similar resistivities ($\sim$3 Ωcm) under illumination with the white light of a halogen lamp (light intensity 100 mW/cm^2). Characteristic lifetime instabilities found in boron-doped Cz wafers under illumination due to the formation of boron-oxygen complexes are not observed in the phosphorus-doped material [4]. However, even before light-induced degradation, the lifetime of the *n*-type wafer is still one order of magnitude larger than the lifetime measured on the *p*-type Cz-Si material. Typical lifetimes of *n*-type Cz-Si wafers are in the millisecond range, making this material an excellent choice for high-efficiency solar cells [1, 18–20]. If the *n*-type material is overcompensated and thus contains some boron in addition to phosphorus, boron-oxygen centers can also form under illumination [21], however, they are less detrimental in *n*- than in *p*-type Cz material, which is mainly due to the strongly asymmetric capture cross section ratio of σ_n/σ_p = 10 of the boron-oxygen center, where σ_n is the capture cross section for electrons and σ_p that for holes. These fundamental advantages of *n*- over *p*-type Cz-Si make *n*-type Cz-Si an excellently suited material for high-efficiency Si solar cells.

1.2. Emitter formation on *n*-type silicon

For solar cells processed on *n*-type Cz-Si bulk material, a p^+-emitter is needed for the formation of the *pn*-junction. The main technologies for the p^+-emitter formation, such as the boron diffusion, the a-Si/c-Si heterojunction and the screen-printed aluminum-doped p^+-emitter, are introduced and compared to each other in the following Sections.

1.2.1. Boron-diffused p^+-emitters

The most common approach for the formation of a p^+-emitter on *n*-type Si base material is the boron diffusion. Figure 1.2 shows a schematic of a quartz tube used in diffusion processes [22]. A typical boron-diffusion process consists of two sequences. The first one is the deposition and the second one the drive-in sequence. During deposition a gas mixture enters the heated quartz tube where the silicon wafers are positioned in a silica boat. The gas mixture consists of three gases: oxygen (O_2), nitrogen (N_2) and boron tribromide (BBr_3). The gases are at ambient temperature before they enter the quartz tube. As the quartz tube is heated (typical temperatures for a boron diffusion range from 900°C up to 1100°C) the gas mixture heats up and a reaction between the O_2 and the BBr_3 takes place according to the following reaction equation [23, 24]:

$$4BBr_3(g) + 3O_2(g) \rightarrow 2B_2O_3(l) + 6Br_2(g). \tag{1.1}$$

The liquid B_2O_3 condenses on the silicon wafer surface and a chemical reaction takes place, resulting in SiO_2 plus elemental boron:

$$2B_2O_3(l) + 3Si(s) \rightarrow 4B(s) + 3SiO_2(s). \tag{1.2}$$

A mixed phase B_2O_3-SiO_2 system forms, where the SiO_2 is dissolved in the liquid B_2O_3. This mixed phase is called borosilicate glass (BSG). During the following diffusion step, the drive-in is performed, where the elemental boron diffuses into the silicon wafer as well as into the BSG. Typically, a very high boron concentration is formed at the surface of the wafer, this is the so-called *boron pile up* [25–27]. This high boron concentration at the silicon surface transforms a thin surface layer into a Si-B compound, the so-called boron rich layer (BRL). Recently, it has been found that the formation of the BRL has a strong impact on the bulk carrier lifetime of the silicon wafer [28]. In Ref. [28] it was conjectured that the lifetime degradation occurs during the cool-down ramp at the end of the diffusion process. The lifetime degradation has been attributed to the creation of crystal defects by mechanical stress due to different thermal expansion coefficients of the silicon and the BRL. The formation of the BRL can be avoided by performing the drive-in under an oxidizing atmosphere. This was shown to avoid lifetime degradation [28]. In addition, the high temperatures (900-1100°C) during diffusion can induce defects in the silicon bulk, degrading the carrier lifetime as well [28–30].

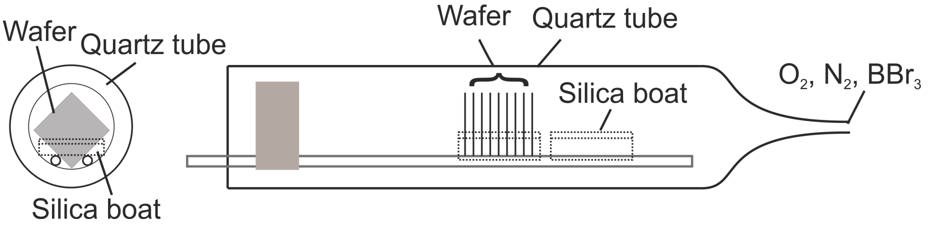

Figure 1.2.: *Schematic of a quartz tube in a typical diffusion furnace.*

Thus, the boron diffusion process is capable of providing p^+-emitters of very high quality, however, it is technologically demanding and has a high thermal budget and thus it is mainly used in laboratory high-efficiency cell processes. In the industry, currently only the US-based company Sunpower is using the boron diffusion in their production lines.

A. Back-junction solar cells with boron-diffused p^+-emitters

1. De Couster et al. [1] reported an energy conversion efficiency of 22.7% for Sunpower´s A-300 back-junction back-contact (BJBC) solar cell on *n*-type Cz-Si material [1]. A high-volume production of the A-300 BJBC cells with an average efficiency of 22.4% on a cell area of 144 cm^2 was introduced in 2007 [1]. A schematic of Sunpower´s back-junction back-contact solar cell is shown in Figure 1.3. Recently, Cousins et al. [2] reported a

peak conversion efficiency of 24.2% for Sunpower´s latest generation (GEN III) *n*-type back-junction back-contact solar cell fabricated on a cell area of 155.1 cm^2.

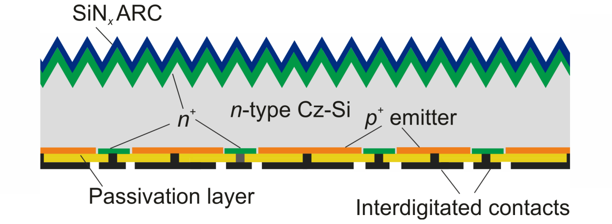

Figure 1.3.: *Schematic of the back-junction back-contact n-type silicon solar cell produced by the US-based company Sunpower after Ref. [1].*

2. Guo et al. [31] reported a laser-grooved interdigitated backside buried contact (IBBC) cell (see Fig. 1.4). On a cell area of 8 cm^2 a conversion efficiency of 19.2% was achieved using 1 Ωcm *n*-type FZ-Si and 16.8% on *n*-type Cz-Si.

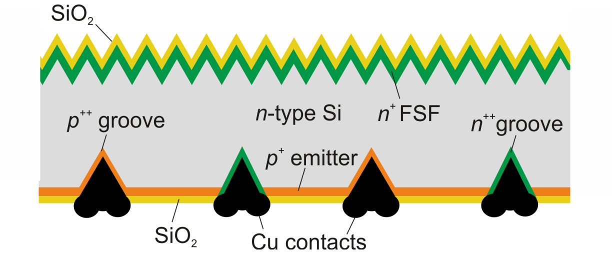

Figure 1.4.: *Schematic of the laser-grooved IBBC solar cell presented by Guo et al. [31].*

3. Zhao et al. [29, 32] reported a rear-junction passivated emitter and rear totally diffused (re-PERT) solar cell (see Fig. 1.5). They achieved a maximum conversion efficiency of 22.7% on 1 - 2 Ωcm *n*-type FZ-Si and 20.8% for 4.5 - 5.5 Ωcm *n*-type Cz-Si wafers, both on a cell area of 22 cm^2.

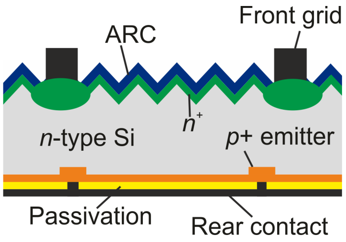

Figure 1.5.: *Schematic of the re-PERT solar cell presented by Zhao et al. [29, 32].*

4. Large-area (149 cm^2) screen-printed n-type Cz-Si solar cells with a boron-diffused rear emitter (see Fig.1.6) demonstrating cell efficiencies of 17.4% were presented by Froitzheim et al. [33].

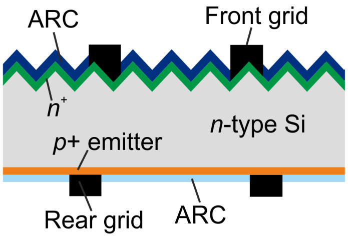

Figure 1.6.: *Schematic of the n-type Cz-Si solar cell with a boron-diffused rear emitter and screen-printed contacts at the front and the rear presented by Froitzheim et al. [33].*

Table 1.1 summarizes the solar cell parameters of the various back-junction n-type Si solar cells with boron-diffused p^+-emitters.

TABLE 1.1.
SOLAR CELL PARAMETERS OF THE BACK-JUNCTION n-TYPE SI SOLAR CELLS FEATURING A BORON-DIFFUSED p^+-EMITTER.

Published by	n-Si (ρ) [Ωcm]	Area [cm^2]	V_{oc} [mV]	J_{sc} [mA/cm^2]	FF [%]	η [%]
Cousins et al. [2] (2010)	Cz (-)	155.1	721.0	40.5	82.9	24.2
De Couster et al. [1] (2007)	Cz (-)	144.0	-	-	-	22.7
Guo et al. [31] (2006)	FZ (1)	8.0	664.0	37.9	76.5	19.2
Guo et al. [31](2006)	Cz (1)	8.0	665.0	32.6	77.6	16.8
Zhao et al. [29, 32] (2006)	FZ (1 - 2)	22.0	702.0	40.1	80.5	22.7
Zhao et al. [29, 32] (2006)	Cz (4.5 - 5.5)	22.0	659.0	39.9	78.7	20.8
Froitzheim et al. [33] (2005)	Cz (-)	149.0	632.0	35.1	78.0	17.4

B. Front junction solar cells with boron-diffused p^+-emitters

1. Mihailetchi et al. [34] achieved a champion efficiency of 18.3% for screen-printed 1.5 Ωcm *n*-type Cz-Si solar cells with a boron-diffused front emitter (see Fig. 1.7) on a cell area of 156 cm^2.

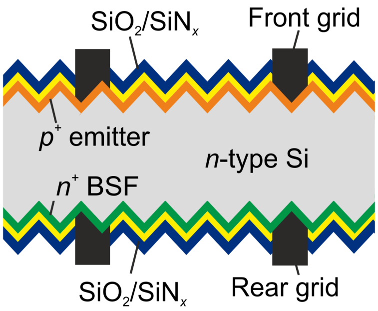

Figure 1.7.: *Schematic of the solar cell with boron-diffused front emitter and screen-printed contacts presented by Mihailetchi et al. [34].*

2. An *n*-type silicon solar cell featuring a boron-diffused front junction (see Fig. 1.8) on 144 cm^2 2 Ωcm Cz-Si was presented by Buck et al. [35] who reported a maximum efficiency of 17.1%.

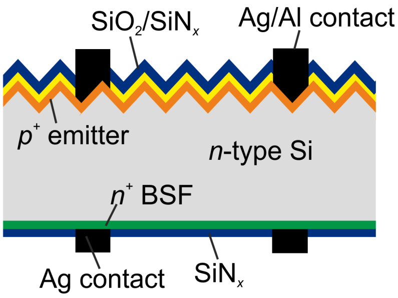

Figure 1.8.: *Schematic of the solar cell with a boron-diffused front junction and screen-printed contacts reported by Buck et al. [35].*

3. Recently, Benick et al. [19] achieved a conversion efficiency of 23.2% for an *n*-type cell on an aperture cell area of 4 cm ^{2}. This passivated emitter with rear locally diffused (PERL) solar cell (see Fig. 1.9) was fabricated using photolithography on 1 Ωcm *n*-type FZ-Si material.

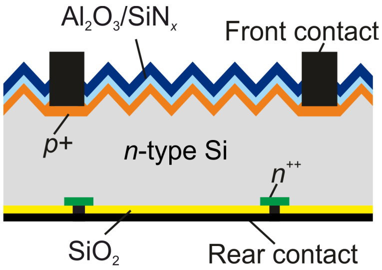

Figure 1.9.: *Schematic of a passivated emitter and rear locally diffused (PERL) solar cell on n-type silicon with a boron-diffused emitter at the front [19].*

Table 1.2 summarizes the solar cell parameters of the various front-junction n-type Si solar cells with boron-diffused p^+-emitters.

TABLE 1.2.
SOLAR CELL PARAMETERS OF FRONT-JUNCTION n-TYPE SI SOLAR CELLS FEATURING A BORON-DIFFUSED p^+-EMITTER.

Published by	n-Si (ρ) [Ωcm]	Area [cm^2]	V_{oc} [mV]	J_{sc} [mA/cm^2]	FF [%]	η [%]
Mihailetchi et al. [34] (2008)	Cz (1.5)	156	-	-	-	18.3
Buck et al. [35] (2006)	Cz (2)	144.0	620	36.3	76	17.1
Benick et al. [19] (2009)	FZ (1)	4	703.6	41.5	80.2	23.4

The compiled cell results demonstrate that a well-controlled boron-diffusion process is capable of providing an excellent p^+ emitter quality allowing for conversion efficiencies above 20%. Nevertheless, the boron-diffusion process is still an issue due to defect formation in the silicon bulk [28–30]. Thus, it is still mainly used for laboratory-type high-efficiency solar cells, except the outstanding BJBC solar cells from Sunpower Corp.

1.2.2. a-Si/c-Si heterojunction emitters

A technological alternative to high-temperature-diffused boron p^+-emitters is the deposition of a doped amorphous hydrogenated silicon (a-Si:H) thin film on top of the crystalline silicon (c-Si) wafer, the so-called a-Si:H/c-Si heterojunction emitter. Figure 1.10 shows a schematic representation of a HIT (**H**eterojunction with **I**ntrinsic **T**hin Layer) solar cell with an a-Si:H p^+ emitter on an n-type c-Si silicon substrate as it has been successfully developed by the Japanese company Sanyo [3, 36]. Electrical contacting of this solar cell is performed by low-temperature screen-printing of a silver paste onto the TCO (Transparent Conductive Oxide). The process-

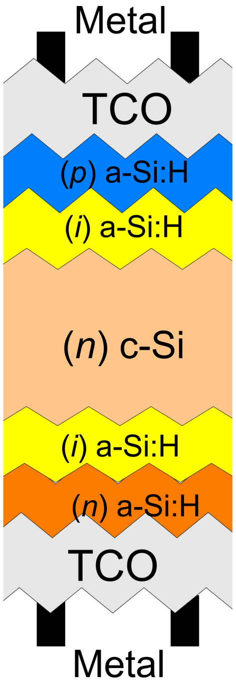

Figure 1.10.: *Schematic representation of a symmetric HIT solar cell which has been developed by Sanyo [36] including a passivating intrinsic a-Si:H layer at the front and at the rear side of the solar cell.*

ing of a-Si:H/c-Si heterojunction solar cells is relatively simple, as the *pn*-junction is formed by deposition of a highly boron-doped a-Si:H layer deposited by plasma-enhanced chemical vapor deposition (PECVD) on top of the *n*-type c-Si silicon substrate at temperatures of 200°C or even below [36].

However, the apparent simplicity and the low thermal budget of the heterojunction process is somewhat misleading. There is a huge parameter range which has to be taken into account in order to achieve conversion efficiencies above 20%. To give an impression what the main challanges in the fabrication of heterojunction solar cells are, a few are briefliy discussed in the following.

One of the main challenges is the reduction of optical losses. This can be realized by: (i) the introduction of textured surfaces, which is an issue as the deposition of a uniform and homogeneous a-Si:H layer onto a textured c-Si surface is not straightforward [37]. (ii) The absorption of sun light within the TCO and the a-Si:H layers has to be minimized. New materials for transparent conductive layers have to be developed which combine low carrier densities with high carrier mobilities. (iii) A high aspect ratio of the metalization grid at the front side is needed due to the high sheet resistivity of the TCO layer. Thus, an optimization of the viscosity and rheology of the silver screen-printing pastes and of the printing parameters are required in order to achieve fine lines with a high aspect ratio [38].

Another challenge is to reduce the recombination losses at the interfaces. This can be realized by: (i) an optimized pre-cleaning of the silicon wafer in order to remove impurities from the surface, (ii) hydrogen termination to saturate dangling bonds at the Si surface using H_2 or HF, and (iii) producing a high-quality, homogeneous and well-passivating undoped (*i*)a-Si:H layer.

The ohmic losses have also to be taken into account. As a consequence, (i) the TCO has to be highly conductive, and (ii) a good ohmic contact has to be realized between the different layers.

Furthermore, the conversion efficiency, particularly the short-circuit current density J_{sc}, is strongly dependent on the thickness of the (*i*)a-Si:H and the doped a-Si:H layers. The thickness of the intrinsic layer has a strong influence on J_{sc} (due to light absorption within the (*i*) layer) and on the *FF* (due to the sheet resistance of the doped a-Si layer) [39]. Thus, the a-Si:H layers have to be homogeneous and well passivating, simultaneously they have to be as thin as possible (less then 10 nm). In order to achieve an abrupt *pn*-junction, the epitaxial growth during deposition of the a-Si:H layer has to be avoided. This can be achieved by optimization of the rf-power density during the PECVD process and the a-Si:H deposition temperature [40].

a-Si/c-Si heterojunction solar cells on *n*-type Si

Using the solar cell structure shown in Figure 1.10, Sanyo has achieved a record-high conversion efficiency of 23.0% on 100.4 cm^2 *n*-type Cz-Si [41]. In order to achieve a conversion efficiency $\geq$23%, Sanyo has developed and optimized their processes for more than 20 years. Most other research groups still have not reached the 20% efficiency level.

Conrad et al. [42] have fabricated a 19.8% efficient a-Si:H/c-Si cell without additional passivating intrinsic layer on 1 cm^2 *n*-type FZ-Si. Descoeudres et al. [43] reported a conversion efficiency of 20.3% for a p^+nn^+ heterojunction solar cell fabricated on 4 cm^2 *n*-type FZ-Si, where a very high frequency (40.68 MHz) (VHF) parallel-plate PECVD reactor was used for the a-Si:H deposition. Fujiwara et al. [44] reported a conversion efficiency of 17.5% for an a-Si:H/c-Si solar cell fabricated on 0.2 cm^2 *n*-type Cz-Si. Wang et al. [45] have reported a conversion efficiency of 17.2% for an a-Si:H/c-Si solar cell fabricated on 0.9 cm^2 *n*-type Cz-Si. The heterojunction approach is a promising and potentially cost-saving technology without any high-temperature processing steps, however, the high complexity of this technology is still an issue, which is not completely resolved yet. Table 1.3 shows a summary of the the solar cell parameters of heterojunction solar cells reported in the literature.

TABLE 1.3.
SOLAR CELL PARAMETERS OF *n*-TYPE SI HETEROJUNCTION SOLAR CELLS.

Published by	*n*-Si	Area [cm^2]	V_{oc} [mV]	J_{sc} [mA/cm^2]	*FF* [%]	η [%]
Sanyo [41] (2009)	Cz	100.4	729.0	39.5	80.0	23.0
Conrad et al. [42] (2006)	FZ	1.0	639.0	39.3	79.0	19.8
Descouedres et al. [43] (2010)	FZ	4	717.0	38.2	74.2	20.3
Fujiwara et al. [44] (2009)	Cz	0.2	656.0	35.5	75.0	17.5
Wang et al. [45] (2008)	Cz	0.9	664.0	35.3	74.5	17.2

1.2.3. Screen-printed aluminum-doped (Al-p^+) regions

In this Section, a description of the processing and the physics behind the formation of an Al-p^+ emitter in silicon using screen-printing technology is given.

The screen-printing process

Screen-printing is a technique where a viscous metal paste (Al paste) is applied to the Si surface through a screen consisting of a stainless steel mesh which is covered with a resist. The resist serves as a mask which defines the geometry to be printed on the sample. Figure 1.11 shows a schematic of the steps of one single screen-printing sequence. First, the Al paste is placed on top the screen (1). Second, by moving the flood bar over the screen surface without applying any force to the screen the Al paste is dispensed over the screen and the mesh is filled by the paste at positions where the resist is open, the screen is now flooded (2). During this flooding process the screen is separated from the sample by the so-called snap-off distance (in this work 1-1.5 mm). Third, by applying a force (in this work ~60 N) the squeegee is pressed on the screen (3). The screen tension is lower than the force applied to the screen by the squeegee, thus the screen is bended and brought in contact with the sample at the position of the squeegee. Fourth, as the screen is under tension it snaps off while the squeegee is moved over the screen (4). Fifth, due to adhesion forces the Al paste is unhinged from the screen and is transfered to the sample through the mesh (5).

The paste is an important ingredient which has a crucial impact on the result. Hence, some details about the composition and the physical properties of an Al paste should be mentioned. Usually, a metalization paste for the rear side of a silicon solar cell consists of small-grained Al particles plus a small amount of a glass frit, which are both suspended in an organic solvent.

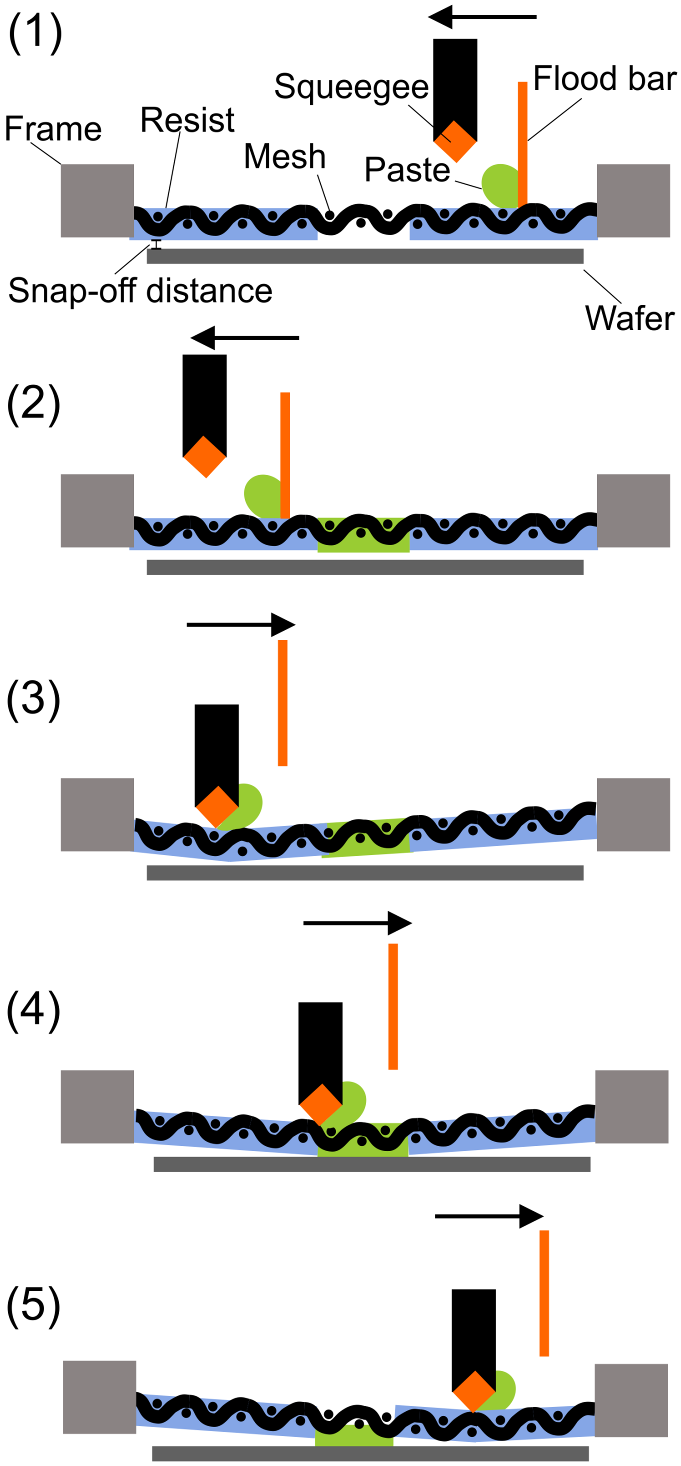

Figure 1.11.: *Schematic of a screen-printing sequence.*

The organic solvent is used to keep the powders in the paste (Al particles and the glass frit) in suspension and it is mainly responsible for the rheology of the paste. The organic components are based on a resin (e.g., terpineol or ethylcellulose) which acts as a binder for the particles in the paste and it is dissolved in a thinner (e.g., Diethylenglycolmonobutylether, Dibutylphthalat). The viscosity of the paste is tuned by the ratio between the several components, where 10-20 wt% of the complete paste are the organic components. The metal component consists of small-grained particles, mostly spheres (Al: 1-5 μm). About 70-80 wt% of the complete paste are given by the metal. The third component is optional and is made of powdered glass. The glass frit enhances the sintering and forms a good mechanical contact of the metal to the silicon. Typically, the glass used for the pastes has a relatively low glass transition temperature of $\sim$ 600°C and it consist e.g. of lead-boron-silicate-glass or zinc-boron-silicate-glass with additives such as lead oxide (PbO) or silicon dioxide (SiO_2). About 2-5 wt% of the complete paste is due to the glass frit.

In order to achieve a homogeneous Al-p^+ region after firing, the Al paste needs to be printed with a homogeneous layer thickness over the entire sample area. The quality of the print and finally of the Al-p^+ region depends on several factors, such as:

- the type of the screen-printer used,
- the mesh parameters (thickness of the wire, knitting per inch, thickness of the resist, tension of the mesh),
- the printability of the paste (composition, viscosity, particle size),
- the squeegee (material, geometry, hardness),
- the printing parameters (squeegee pressure, squeegee speed, snap-off distance, parallelism between screen and sample),
- the surface properties of the sample (surface roughness, oxides, crystallographic orientation),
- the weather (temperature and air humidity have a crucial impact on the viscosity of the paste).

The huge variety of parameters and the influence of these parameters on the printing result will not be discussed in this work and are explained in detail in Refs. [46–49].

The morphological and electrical properties of a screen-printed Al-p^+ region at a given printed amount of Al are mainly influenced by the firing process. The temperature as well as the exposure of the sample to a given temperature are the predominant parameters which have a strong influence on the homogeneity of doping concentration and thickness of the Al-p^+ region. In this work, the samples as well as the solar cells are fired in a conveyor-belt furnace. Hence, the duration of exposure at a given temperature is set by the belt speed, which is typically provided in mm/min. The firing process can be divided into three sub-processes: (i) the burnout of the organic solvents and softening of the glass frit, (ii) the alloying of the Al and Si at the interface, and (iii) solidification of the Al-Si melt during cooling. Figure 1.12 shows a measured firing profile which has been applied to the samples of this work to form the Al-p^+ region. The differently marked sections are related to the sub-processes (i), (ii), and (iii).

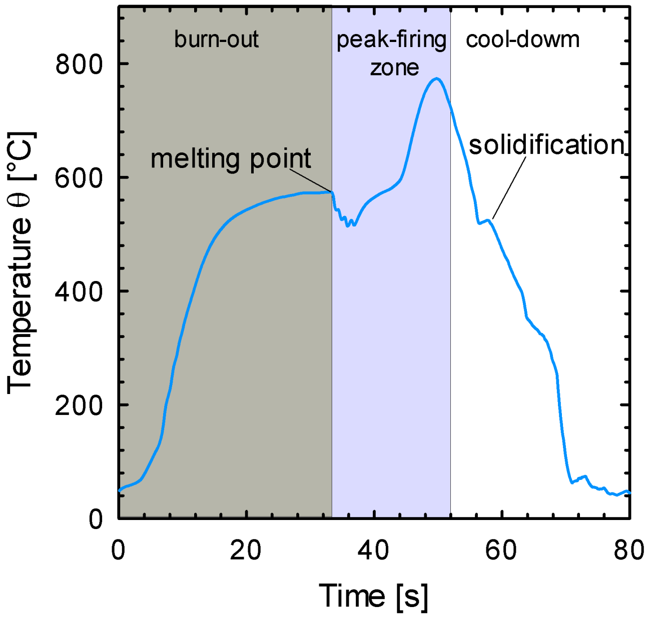

Figure 1.12.: *Typical firing profile in a conveyor-belt furnace (Centrotherm DO-FF-8.600-300) used for the formation of the Al-p^+ regions in this work. The profile was measured using a Datapaq DQ1860 data logger.*

Formation mechanism of the Al-p^+ region

Figure 1.13 (a) shows a binary phase diagram of Al and Si [50], (b) the solid solubility of aluminum in silicon as a function of the applied temperature, and (c) a schematic representation and corresponding cross-sectional SEM images of characteristic steps during the formation of the screen-printed Al-p^+ region. The SEM images originated from this work.

According to the phase diagram the melting point of Si decreases -starting at 1410°C for 100 at% Si- along the liquids line with increasing Al concentration. At a Si at% ratio of about 12%, and thus of 88% Al, the melt solidifies at 577°C [point (5) in Fig. 1.13 (a)] which is well below the solidification point of any other Al-Si composition. This so-called *eutectic point* represents the lowest solidification temperature a binary system can have, which simply means that the liquid and the two solid solutions coexist and are in chemical equilibrium. In other words: the Gibbs free energy equals zero at that point.

During firing of the Al-coated Si sample the sample runs through a temperature profile as

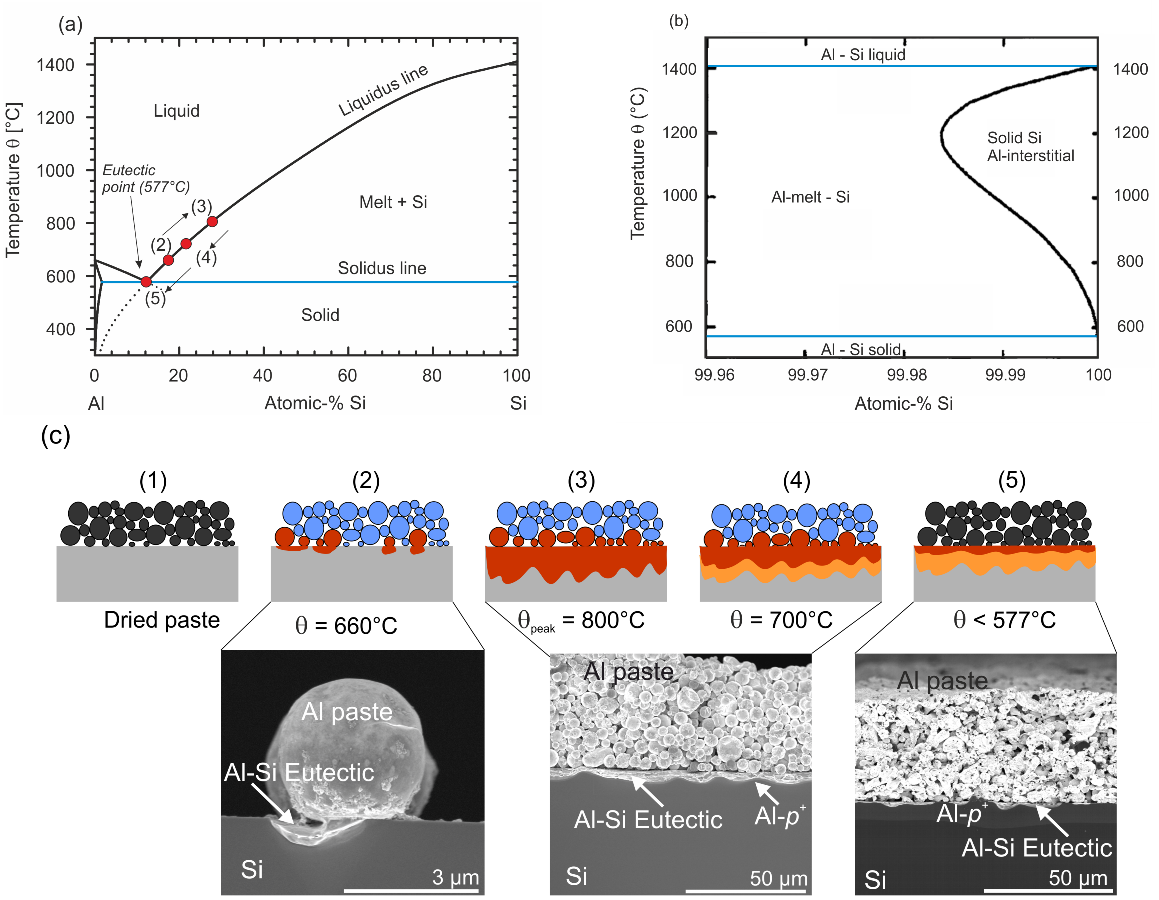

Figure 1.13.: *(a) Binary phase diagram of aluminum and silicon showing a eutectic point at 577°C. (b) Solid solubility of aluminum in silicon as a function of the applied temperature. (c) Schematic representation and cross-sectional SEM images of the single steps during formation of the Al-p^+ region.*

it is shown in Figure 1.12. In the first firing region (temperatures of 450-600°C), the organic solvents are burned. The Al-p^+ regions forms in the second and third firing region, where the peak temperature of about 750-850°C is reached. The optimum firing temperature depends on the printed amount of Al paste, the wafer thickness, the paste type (with glass frit or not) and on the exposure time (belt speed). Typically, the firing profile needs to be optimized in accordance with the given sample/paste system and the desired result. In order to obtain an $\sim$8 μm thick and homogeneous Al-p^+ region, a peak firing temperature of θ_{peak} = 770°C at a belt speed of 2000 mm/min has been applied in this work. Figure 1.13 (c) shows a schematic of the several steps during formation of the Al-p^+ region. The sequence starts with the screen-printed and dried paste (1). When the temperature rises above the melting point of the Al (660°C) the Al particles start to melt, the reaction of the Al with the Si starts and a liquid composition of Al and Si forms (2). At the peak temperature of 770°C a closed film of an Al-Si liquid (at θ_{peak} = 770°C: 27 at% Si and 73 at% Al) forms at the Si surface (3). During cooling, the Al-Si liquid starts to undercool, thus, the Si concentration in the melt is decreasing in accordance with the liquidus line in Fig. 1.13 (a). During this process the excess amount of Si is rejected from the melt and Si grows epitaxially at the solid-Si/liquid-Al-Si interface (4). The epitaxially grown Si layer is now doped with Al in accordance with the solid solubility of Al in Si at a given temperature [see Figure 1.13 (c)]. In this work, a peak doping concentration of (3-4)$\times 10^{18}$ cm^{-3} is obtained. If the system is cooled down to the eutectic temperature (577°C), a sudden solidification of the residual Al-Si liquid and of the Al particles starts (5). The solid Al-Si eutectic (12.2 at% Si and 87.8 at% Al) covers the entire Al-doped p^+ region. The resulting thickness of the Al-doped p^+ region $W_{\text{Al-}p^+}$ is to a good approximation determined by the amount of the Si dissolved in the Al-Si melt at the peak temperature and can be estimated by the following equation which has been empirically determined by Alamo et al. [51]:

$$W_{\text{Al-}p^+} = \frac{t_{\text{Al}} \times \rho_{\text{Al}}}{\rho_{\text{Si}}} \left(\frac{F(T)}{1-F(T)} - \frac{F(T_0)}{1-F(T_0)} \right), \tag{1.3}$$

where t_{Al} represents the screen-printed Al thickness, ρ_{Al} and ρ_{Si} are the mass densities of Al and Si, $F(T)$ is the Si atomic weight percentage of the molten phase at the peak alloying temperature T and $F(T_0)$ is the Si atomic weight percentage at the eutectic temperature T_0. $F(T) = 22$ at% and $F(T_0) = 12.2$ at% are obtained from the Al-Si phase diagram shown in Fig. 1.13.

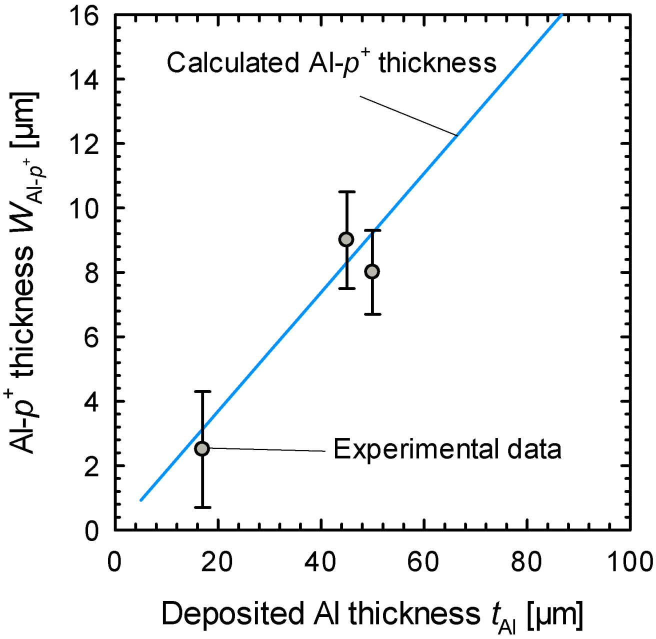

Figure 1.14.: *Calculated thickness of the Al-doped p^+ region (blue line) according to Eq. (1.3) in comparison with the experimental data (circles) measured in this work.*

The blue line in Fig. 1.14 shows the calculated Al-p^+ thickness $W_{\text{Al-}p^+}$ as a function of the deposited Al thickness t_{Al} according to Eq. (1.3) at a measured peak firing temperature of 770°C (see Figure 1.12). As can be seen from Fig 1.12, the experimental data from this work are in a good agreement with the calculated thickness.

However, the electrical quality of the Al-p^+ region depends also on its homogeneity. In particular, the Al-p^+ region must be closed over the entire solar cell area if the Al-p^+ region is used as an emitter on n-type Si material.

1.3. The use of the screen-printed Al-p^+ region as back surface field (BSF)

The last Section explained the screen-printing technology and the firing process itself as well as the basic physics behind the formation of the Al-p^+ region and the influencing parameters during firing. In this Section, the application of such Al-p^+ regions to p-type solar cells as a BSF is demonstrated as this is the predominant industrial application of such screen-printed Al-p^+ regions today.

Typically, the rear contact of an industrial p-type silicon solar cell is formed in a screen-printing process, where an Al paste is screen-printed on the Si wafer and subsequently fired in a conveyor-belt furnace. The Al-p^+ region is formed during this firing step. In conventional industrial-type p-type Si solar cells, this screen-printed aluminum-doped p^+-region serves as the back surface field, reducing the effective surface recombination velocity at the rear side of the cell.

Figure 1.15 shows a numerical PC1D [52] simulation of the open-circuit voltage V_{oc} of two types of p-type Si solar cells: (1) with BSF (blue line) and (2) with passivated rear side without any BSF (red line). For cell type (1) V_{oc} is plotted as a function of the Al-BSF depth W_{BSF} and for cell type (2) as a function of the rear surface recombination velocity S_{rear}. For this calculation a 50 $\Omega/\square$ n^+ emitter is assumed at the textured front side of the solar cell. The front side is also assumed to be passivated by a 70 nm thick SiN_x layer with a refractive index of $n = 2.05$ at a wavelength of $\lambda = 631$ nm. An emitter saturation current density $J_{0\text{e}}$ of 300 fA/cm^2 is assumed for the front side. At the rear the Al-BSF is assumed to have a realisic J_{BSF} value of 750 fA/cm^2 for case (1). Alternatively, in case (2), S_{rear} is varied from 1 cm/s (perfectly passivated rear surface) to 10^6 cm/s (unpassivated rear side). As can be seen from Fig. 1.15, if a BSF is applied to the rear of the cell the BSF thickness W_{BSF} has only a minor impact on V_{oc} for $W >$ 2 μm, even if the rear side is fully metalized, where we have assumed a surface recombination velocity of $S_{\text{metal}} = 10^6$ cm/s. This can be explained by the potential barrier between the p-type base ($N_{\text{dop}} = 1 \times 10^{16}$ cm^{-3}) and the p^+-type Al-BSF ($N_{\text{dop}} = 3 \times 10^{18}$ cm^{-3}) which hinders the minority charge carrier to reach the highly recombination active metalized Si surface and to recombine there. Thus, the Al-BSF lowers the recombination underneath the metal contacts drastically, which increases the V_{oc} and thus the solar cell efficiency as well. Without BSF the contacts are directly connected to the lowly doped Si base and hence the recombination at the metalized region is extremely high ($S_{metal} = 10^6$ cm/s). In order to achieve at least the same V_{oc} as with BSF, the non-metalized surface needs to be very well passivated. In our example, S_{rear} has to be at least 100 cm/s to achieve nearly the same passivating effect as it is achieved by applying a full-area metalized screen-printed Al-BSF. This simple simulation shows how effective the application of a simple Al-BSF can be. Technologically, the formation of the Al-BSF is a quite simple and robust process and hence it is routinely used in industrial cell production.

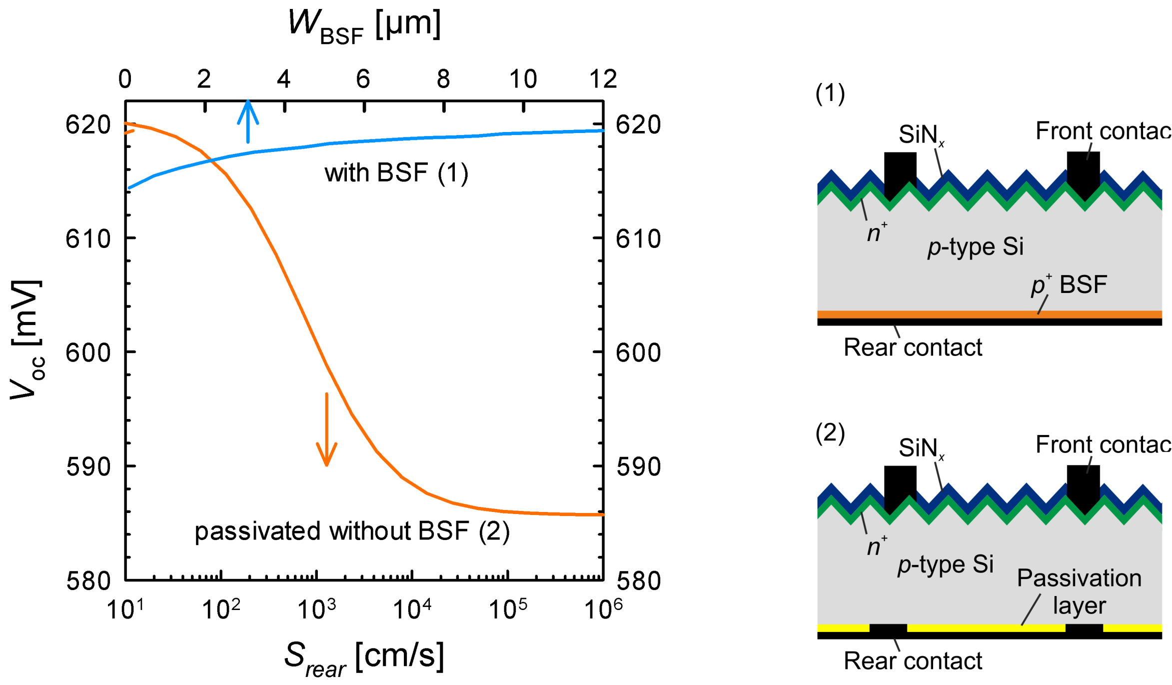

Figure 1.15.: *PC1D simulation: V_{oc} of an industrial-type p-type Si solar cell as a function of the Al-BSF thickness W_{BSF} (1) and as a function of the surface recombination velocity S_{rear} at the rear without a BSF (2). The schematic of the corresponding solar cell structures (1) and (2) are shown on the right.*

1.4. Solar cells with screen-printed Al-p^+ emitters

In contrast to the industrial application of the screen-printed Al-p^+ region as BSF, it has also been used in the laboratory as emitter at the rear of n-type Si solar cells. The status of solar cell results featuring a screen-printed Al-p^+ emitter until the beginning of this work is summarized in the following.

Meier et al. [53] from the US-based company Ebara Solar introduced the so-called *PhosTop* solar cell in 2001 as a new solar cell structure in which the *pn*-junction is formed at the rear of an *n*-type silicon wafer by alloying aluminum with the *n*-type Si. A phosphorus diffusion at the front side of the cell acts as front surface field (FSF). Meier summarized the benefits of such a structure in the following way [53]: no shunting of the *pn*-junction, effective front surface field due to the strong phosphorus diffusion at the front, high minority carrier lifetime in the base and immunity to light-induced degradation. Using 100 μm thick antimony-doped 20 Ωcm dendritic web silicon substrates, a maximum cell efficiency of 14.2% was obtained [53].

In 2003, Cuevas et al. [54] formed an Al-p^+ emitter at the rear side of an 80 Ωcm *n*-type FZ-Si wafer by annealing evaporated high-purity aluminum. With this technique a conversion efficiency of 16.9% was achieved on 4 cm^2. Cuevas et al. also determined an upper limit of the open-circuit voltage V_{oc} to be 641 mV [54] for such a type of Al-p^+ emitter. Using laser-fired local Al emitters (LFE) at the rear of a 100 Ωcm FZ-Si wafer Glunz et al. obtained a 19.4% efficiency on a cell ara of 4 cm^2 [55].

Applying a full-area screen-printed Al-p^+ emitter to a 4 Ωcm *n*-type Cz-Si material, at the ISFH Schmiga et al. [56] demonstrated an efficiency of 18.9% on 4 cm^2.

Some results for industrial-type *n*-type Si solar cells with screen-printed front and rear contacts were also published. Hacke et al. [57] presented in 2004 an efficiency of 15% on a cell size of 100 cm^2 on 1 Ωcm *n*-type FZ-Si. Buck et al. [58] achieved an efficiency of 16.4% on 4 cm^2 sized 5 Ωcm *n*-type Cz-Si wafers. Using 20 Ωcm *n*-type FZ-Si wafers Kopecek et al. [59] reported on a 16.4% efficiency on 150 cm^2. At ISFH Schmiga et al. [60] fabricated a 17% efficient cell on 100 cm^2 using 4 Ωcm *n*-type Cz-Si material.

Mihailetchi et al. [61] achieved a cell efficiency of 17.4% on a cell area of 140 cm^2 using 31 Ωcm *n*-type FZ-Si material. However, most of these solar cells - apart of the LFE solar cell by Glunz et.al. [55] - are limited by the fully metalized rear emitter surface. To overcome this limitation and to achieve higher efficiencies using Al-p^+ emitters, we propose in this work a surface-passivated screen-printed emitter as a possible solution, as it would decrease the surface recombination velocity of the rear-sided Al-p^+ emitter.

TABLE 1.4.
SOLAR CELL PARAMETERS OF n-TYPE SI SOLAR CELLS FEATURING A SCREEN-PRINTED AL-p^+ EMITTER.

Published by	n-Si (ρ) [Ωcm]	Area [cm^2]	V_{oc} [mV]	J_{sc} [mA/cm^2]	FF [%]	η [%]
Cuevas et al. [54] (2003)	FZ (80)	4.0	617.0	34.5	79.2	16.9
Glunz et al. [55] (2004)	FZ (100)	4.0	646.0	39.8	75.1	19.4
Schmiga et al. [56] (2006)	Cz (4)	3.9	627.0	38.6	78.2	18.9
Hacke et al. [57] (2004)	FZ (1)	100.0	-	-	-	15
Buck et al. [58] (2004)	Cz (5)	4.0	623.0	31.4	77.9	15.3
Kopecek et al. [59] (2004)	FZ (20)	156.0	618.0	34.0	77.9	15.4
Schmiga et al. [60] (2006)	Cz (4)	100.0	625.0	34.8	78.3	17.0
Mihailetchi et al. [61] (2007)	FZ (31)	148.5	632.0	35.5	77.4	17.4

1.5. Chapter summary

This Chapter started with a brief review of the benefits of n-type Cz-Si material over p-type Cz-Si in terms of higher and stable carrier lifetimes under illumination due to the absence of recombination-active B-O complexes in boron-doped Cz-Si which form during illumination.

Furthermore, three common technologies for the p^+-emitter formation and the main problems of these technologies were briefly reviewed: (i) The high-temperature boron diffusion which tends to induce crystallographic defects in the Si bulk, reducing its recombination lifetime drastically. (ii) The a-Si:H/c-Si heterojunction solar cell technology which offers promising potential compared to conventional c-Si solar cells in terms of lower production cost, better thermal stability and higher yield. However, the challenges to fabricate high-efficiency heterojunction Si solar cells are clean and textured c-Si surfaces, abrupt heterojunctions with low interface defect densities and optimum a-Si:H and TCO deposition conditions and layer thicknesses. (iii) As an alternative to the technologically demanding technologies (i) and (ii) the screen-printed Al-p^+ region was introduced, which is a readily available process for the formation of back surface fields (BSFs) in industrial p-type silicon solar cells and has also been successfully applied as rear emitter in n-type Si solar cells. In order to achieve higher efficiencies than those reported in the literature, the fundamental limitations of the screen-printed Al-p^+ region have to be examined and a suitable surface passivation scheme adapted to Al-p^+ emitters has to be developed.

2. Characterization of the screen-printed Al-doped p^+ region

This Chapter deals with the characterization of the electrical and morphological properties of the screen-printed Al-p^+ region. In Section 2.1, the origin of a pronounced concentration peak close to the surface in doping profiles measured on screen-printed Al-p^+ regions is analyzed. The carrier lifetime in screen-printed Al-p^+ regions is determined in Section 2.2 from quantum efficiency measurements on specially designed test structures. The thermal activation of specific defects and their impact on the carrier lifetime within the Al-p^+ regions is the topic of Section 2.3.

2.1. Electron-microscopy analysis of the Al-p^+ emitter surface

From electrochemical capacitance-voltage (ECV) measurements and secondary ion mass spectroscopy (SIMS) measurements it is known that screen-printed Al-p^+ regions show a doping concentration peak close to the surface, which is not consistent with the solid solubility data of Al in Si [17, 50]. During processing of Al-p^+ regions from a screen-printed Al film, the abrupt solidification of the eutectic Al-Si composition forms crystalline silicon structures on the Al-p^+ surface. From energy-dispersive X-ray analysis (EDX), where an enhanced Al signal was measured on these surface structures [62], it was conjectured that the observed concentration peak at the surface probably originates from these residual aluminum-rich silicon structures [62–64], however, the physical reason for the observed peak was never investigated in detail. In this Section, various electron microscopy techniques are combined to reveal the nature of the formed surface islands and line networks, which can be observed on screen-printed Al-p^+ regions after the removal of the Al and the eutectic layer.

2.1.1. Experimental

Single-crystalline shiny-etched (100)-oriented 300 μm thick p-type FZ-Si wafers of 200 Ωcm resistivity are used for the sample preparation. The Al-p^+ region is fabricated on one side of the wafer. The other surface of the sample is passivated by PECVD-SiN$_x$. The processing sequence is as follows: (i) After RCA cleaning a 100 nm thick SiN_x layer is deposited on one side. (ii) Subsequently, a non-fritted Al paste is screen-printed on the opposite surface of the wafer with an amount of 8 mg/cm^2. (iii) To vaporize the organic solvents in the Al paste, the screen-printed samples are dried at 150°C for 10 min using the *Centrotherm DO-HTO-5.200-210* belt dryer. (iv) Finally, the Al-doped p-type region is formed in an *LT-310* infrared conveyor belt furnace from *Radiant Technologies Corporation* at 900°C set temperature for $\sim$13 seconds.

In order to characterize the surface of the Al-doped p^+-region by scanning electron microscopy (SEM) and to perform doping profile measurements of the Al-p^+ region with the electrochemical capacitance voltage (ECV) method, the residual Al paste and the Al-Si eutectic are removed from the Al-p^+ surface in a boiling 37% solution of hydrochloric acid (HCl). Details on the ECV method can be found in the Apendix.

For the advanced microscopic analysis of the islands and line networks remaining on the Al-doped p^+-surface after solidification of the Al-Si eutectic liquid, we apply different electron microscopy techniques including scanning transmission electron microscopy (STEM) in combination with EDX, transmission electron microscopy (TEM), and high-resolution transmission electron microscopy (HRTEM). Sample cross sectioning is performed by focused ion beam (FIB) thinning. The islands and the line networks on the Al-p^+ surface are studied in cross-sectional geometry. For the TEM investigations, conventional cross section sample preparation is carried out, where the samples undergo a mechanical thinning step down to a thickness of 20 μm followed by ion milling with Argon ions. To prepare TEM and HRTEM cross-sectional samples of one specific silicon island, FIB preparation is applied, in which the region of interest is cut out of the sample. The high-resolution TEM images are recorded at an electron acceleration voltage of 200 kV using a *Philips CM200-FEG-UT* electron microscope. Elemental composition of the surface structures is analyzed by energy dispersive X-ray spectra using a Si:Li detector (*Oxford Instruments Link ISIS*) attached to the transmission electron microscope. For the SEM investigations of the Al-p^+ region an ultra-high resolution *Hitachi S-4800* field emission SEM was used. Finally, for the ECV measurements of the genuine Al-p^+ doping profiles, the islands were etched off in a solution composed of nitric acid (39 % HNO_3 in H_2O), acetic acid (99% CH_3COOH in H_2O) and hydrofluoric acid (40 % HF in H_2O) in a 6:1:1 ratio.

TEM sample preparation

The FIB preparation method is applied to the samples in order to investigate the bulk and the surface of the islands in detail. For the specific preparation of one single surface island a *FEINanolab 600* dual-beam system is used where a field emission gun (FEG) SEM and an ion microscope are combined in one vacuum chamber which allows to localize regions of interest and to extract a piece of material from the bulk using a Ga ion beam. This results in a very thin lamella (100 nm) which is readily mounted on the TEM sample holder.

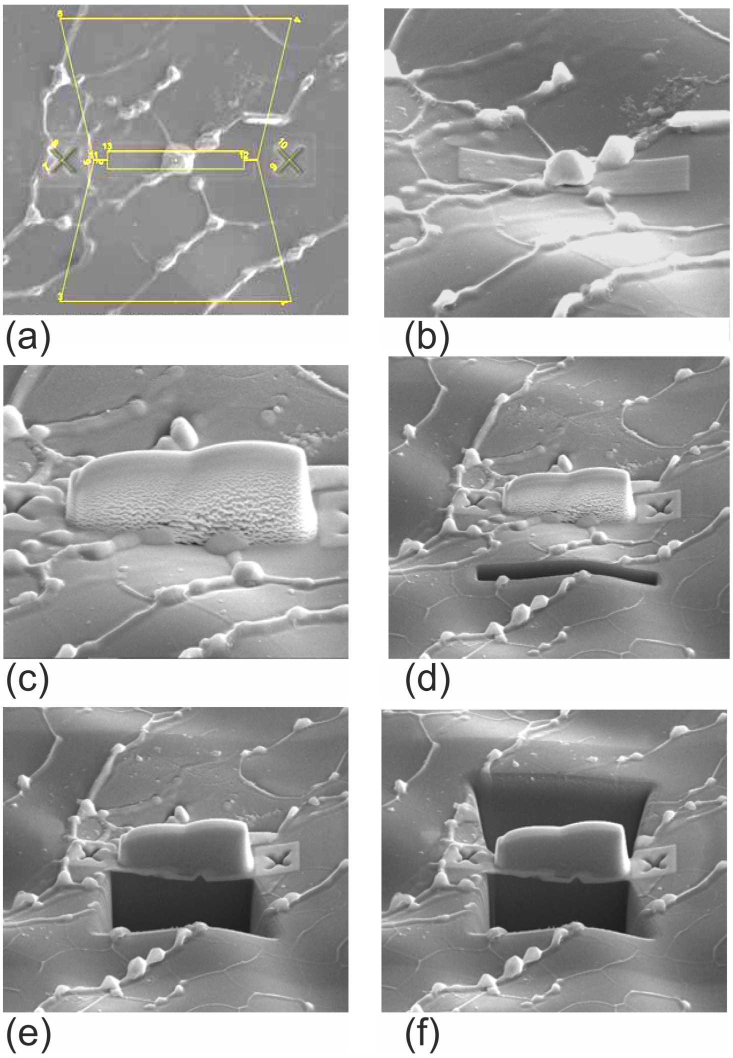

Figure 2.1.: *Preparation of a FIB-lamella. (a) SEM plan view image of the sample surface. Surface islands and line networks are visible. The marking defines the region of interest. (b) Tilted plan view SEM image of the surface island chosen for the FIB preparation. A thin Pt-layer has been deposited by the electron beam on the surface island. (c) A thick Pt-layer has been deposited by using the ion beam. (d)-(f) Using the ion beam the thin lamella is separated from the bulk by removing material in front of and behind the lamella.*

The detailed representation of the single preparation steps is shown in Figs. 2.1 (a-f). First, one single surface island is chosen by the SEM and the island is then coated by a thin platinum (Pt) layer [see Fig. 2.1 (a)]. Second, a thick Pt layer is deposited on top of the thin layer as shown in Figs. 2.1 (b-c). The entire surface island is now coated by the Pt which serves as sample holder for the TEM. Finally, with the aid of the ion beam, Si material is removed from both sides of the deposited Pt film until a 100 nm thick lamella is separated from the bulk Si material [Figs. 2.1

(d-f)].

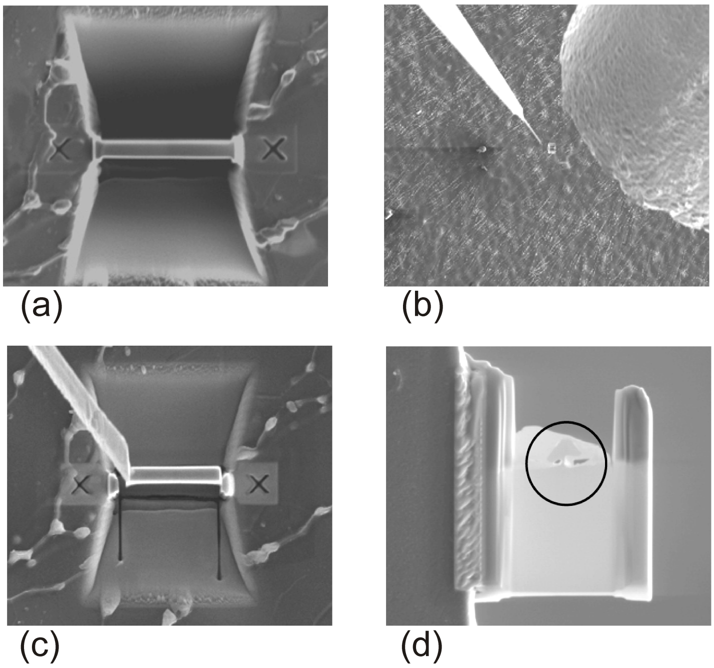

Figure 2.2.: *Lift-out process of the FIB lamella. (a) Plan view SEM image of the already separated lamella. (b) Approaching of the micro manipulator. (c) Sticking of the micro manipulator to the lamella. (d) Cross-sectional view of the TEM lamella mounted to the sample holder of the TEM. The single surface island is visible within the black circle.*

Figure 2.2 (a) shows a plan view SEM image of the separated and free-standing lamella prepared as described above. Figure 2.2 (b) shows the approach of the micro manipulator to the lamella. (c) Sticking of the micro manipulator to one side of the lamella. The separation of the lamella from the sample is not shown here. Finally, Figure 2.2 (d) shows the finished TEM lamella mounted on a TEM sample holder where one single surface island is enclosed [see black circle in Figure 2.2 (d)]. A second cross section TEM sample of the line networks which are also present at the Al-doped p^+ surface has been conventionally prepared by mechanical polishing down to a thickness of 10-20 μm and finally by ion milling with Ar ions at energies of 3-5 keV down to electron transparency (sample thickness $\leq$ 100 nm).

2.1.2. Results

Figure 2.3 shows a cross-sectional SEM image of a screen-printed Al-p^+ sample. The Al-doped p^+-region appears brighter than the high-resistivity bulk of the silicon wafer due to the potential contrast [65]. From this image the Al-p^+ depth is determined to be (7 ± 1) μm. In addition, the

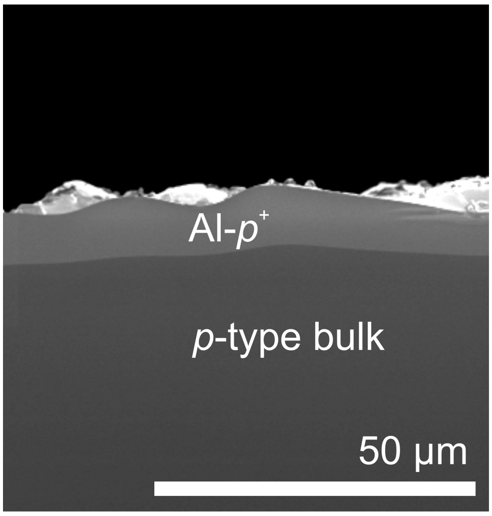

Figure 2.3.: *Cross-sectional SEM image of an Al-p^+ emitter. Due to the potential contrast, the Al-p^+ region appears as bright contrast. The emitter depth is determined from this micrograph to be (7 ± 1) μm.*

SEM image shows also an abrupt junction between the Al-p^+ layer and the silicon bulk, which is characteristic for an epitaxially formed junction from a liquid phase.

Figure 2.4 shows a doping profile of a screen-printed Al-p^+ region measured by the ECV method. The apparent doping concentration peak close to the surface has a depth of 1 - 2 μm. An apparent peak doping concentration between 6×10^{18} and 1.5×10^{19} cm^{-3} was observed on the samples measured in this work. In the junction region, the doping profile shows a second very

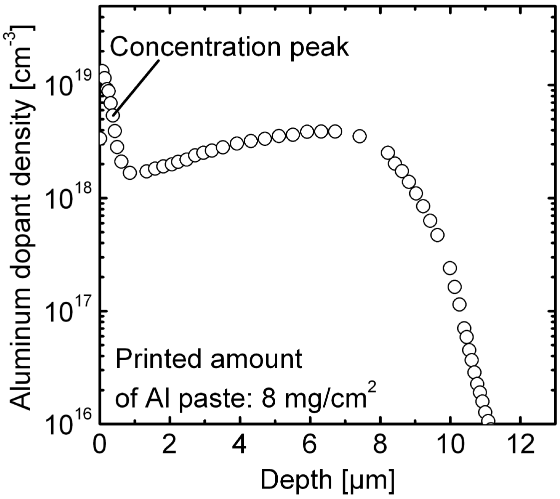

Figure 2.4.: *Aluminum doping profile of an Al-p^+ region measured with the ECV method. The apparent concentration peak at the surface is clearly visible.*

broad concentration peak of (4 - 5)$\times 10^{18}$ cm^{-3} at a depth of ~7 μm, which is attributed to the temperature dependence of the solid solubility of Al in crystalline Si during solidification from the liquid phase [54, 66].

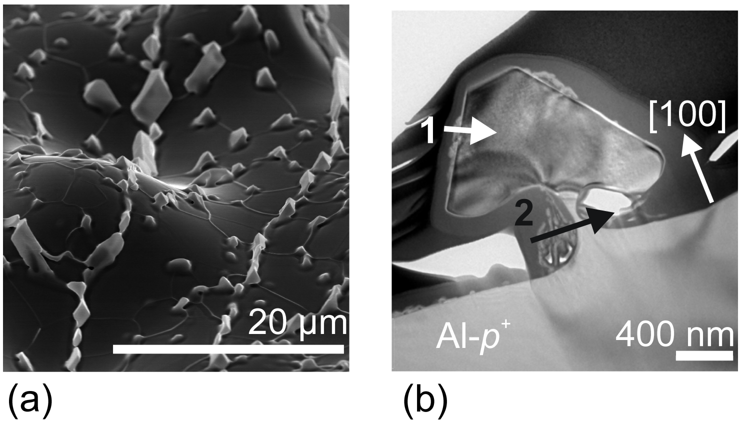

Figure 2.5.: *(a). SEM tilted plan-view image of an Al-p$^+$ Si surface after the residual Al-paste and the Al-Si eutectic have been removed. Islands and line networks appear as bright contrast. (b) Cross-sectional TEM bright-field image of one individual island. The sample is prepared using the focused ion beam method. Lines labeled 1 and 2 indicate positions of EDX line scans shown in Figure 2.7 (a) and (b).*

Figure 2.5 (a) shows a tilted plan-view SEM secondary electron image of the Al-p^+ surface after the residual Al paste and the Al-Si eutectic have been removed in boiling 37% HCl solution. Islands and line networks appear as bright contrast on top of the dark Al-p^+ surface. The typical lateral dimension of the islands is in the range between 1 and 3 μm. The islands are arranged along a line network of nanostructures (lateral dimension ~50 nm). Almost all surface structures show crystallographic facets with a pyramid-like geometry.

Figure 2.5 (b) shows a cross-sectional TEM bright field image of an island, prepared by the FIB method. From this image no defects such as dislocations or grain boundaries or other crystallographic defects can be found within the bulk of the island. The island is completely defect-free and of the same crystallographic orientation as the Al-p^+ bulk and thus epitaxially grown. For a detailed investigation of the Al-rich regions, an EDX line scan analysis is performed along the lines 1 and 2 in Figure 2.5 (b). Figures 2.6 (a-g) show EDX elemental mappings of Si, Al, and Pt measured on the surface island depicted in Figure 2.5 (b). An increased aluminum signal at three positions labeled 1 and 2 in Figure 2.5 (b) can be observed. A closer look at position 2 shows a clear aluminum signal [see Figure 2.6 (g)] underneath the silicon signal [see Figure 2 (f)] indicating a thin silicon capping layer on top of residual Al-rich material. The observed platinum signal surrounding the silicon island shown in Figs. 2.6 (c) and (e) stems from the FIB preparation method. For a detailed investigation of the Al-rich regions, an EDX line scan analysis is performed along the lines 1 and 2 in Figure 2.5 (b).

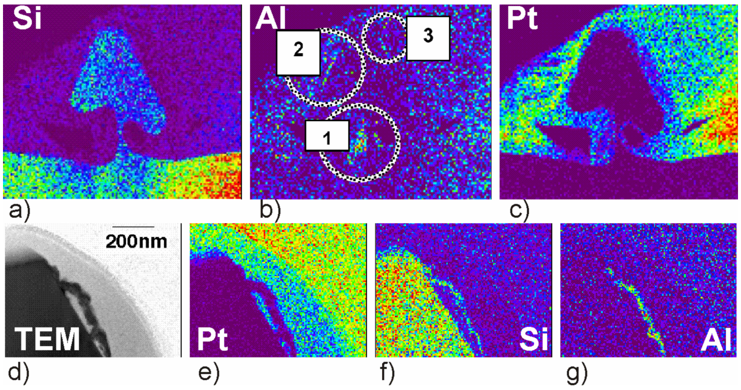

Figure 2.6.: *(a-c) EDX elemental mappings of the Si, Al and the Pt intensity measured on the surface island shown in Figure 2.5 (b). (d) Cross-sectional dark-field STEM image of position 3. (e - g) Elemental mappings of the Pt, Si and the increased Al intensity at position 3.*

Figure 2.7 (a) shows the EDX line scan 1 of Figure 2.5 (b). An Al signal 50 nm underneath the silicon signal is clearly visible. From this finding it is concluded that Al-rich material is covered by a thin layer of Si-rich material. Figure 2.7 (b) shows the EDX line scan 2, in which four Al peaks are visible. The TEM bright-field image shows a lamellar geometry at the Al-rich positions.

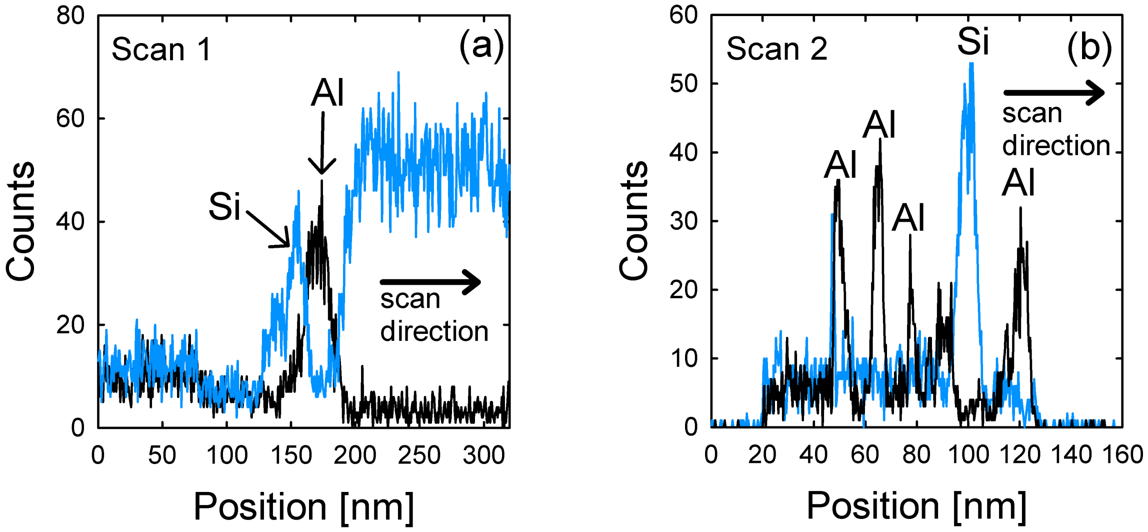

Figure 2.7.: *(a) EDX line scan along line 1 of Figure 2.5 (b). A clear aluminum signal can be identified on the left-hand side of the silicon island; the Al layer is covered by a further silicon layer as indicated by the left-most silicon peak. (b) EDX line scan along line 2 of Figure 2.5 (b). Four Al peaks are visible revealing the lamellar microstructure reminiscent of the Al:Si eutectic.*

This leads to the conclusion that these small Al-rich inclusions can be attributed to a residual Al-Si eutectic phase, which could not be removed in boiling HCl, because it is covered by a thin layer of crystalline Si (see line scan 1) or by the surface island itself (see line scan 2). Figure 2.8 shows a cross-sectional STEM image of one line of the self-assembled line network on the Al-p^+ surface. From this image the structure width is determined to be ~50 nm and the height to be ~26 nm. The EDX line scan along line 3 of Figure 2.8, which is depicted in Figure 2.9 (a), shows an Al signal underneath the Si signal. Again, it is observed that there is Al-rich material

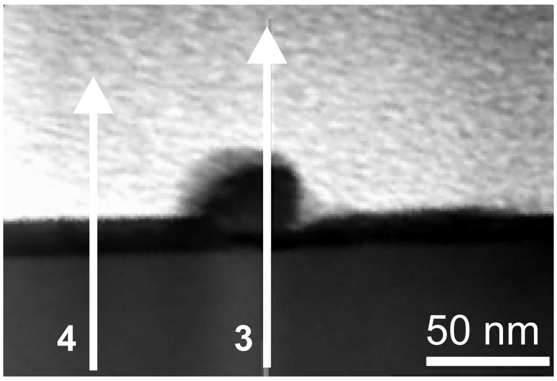

Figure 2.8.: *Cross-sectional STEM bright-field image of a nano-line structure on top of the Al-p^+ Si surface. Lines labeled 3 and 4 indicate positions of EDX linescans shown in Figures 2.9 (a) and (b), respectively.*

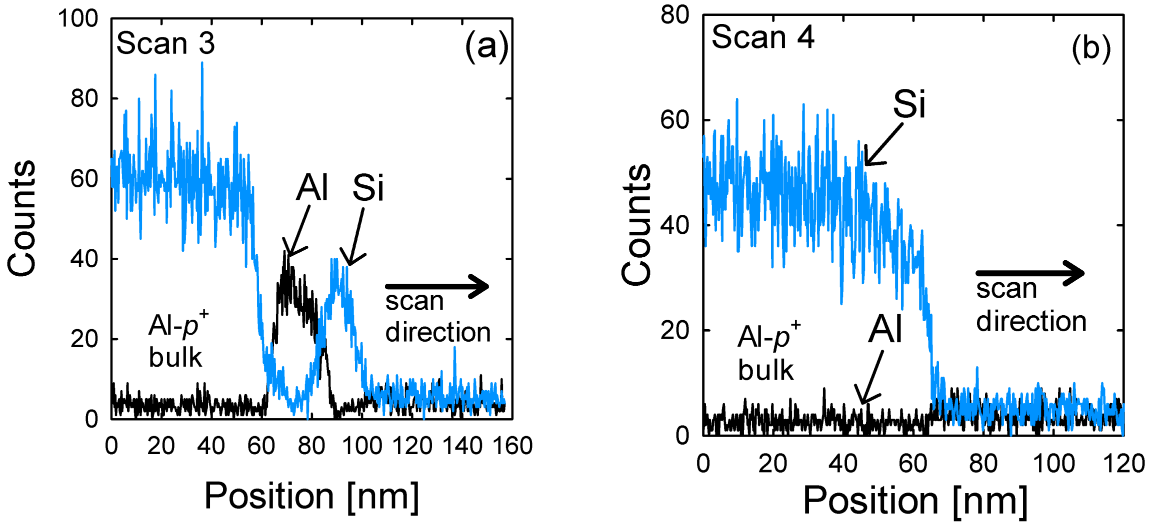

Figure 2.9.: *EDX line scan along line 3 in Figure 2.8, indicating that Al-rich material is covered by a thin layer of Si. (b) Reference EDX line scan along line 4, where no Al-signal can be detected.*

covered by a thin Si layer, which prevents the Al-rich material to be etched in boiling HCl. A reference EDX line scan [Figure 2.9 (b)] on the left side of the surface structure along line 4 of Figure 2.8 shows no aluminum signal at all.

In summary, Al-rich inclusions of about 50 nm in diameter at the surface of the islands covered by a 10-20 nm thick Si layer were found. Al-rich inclusions of lamellar geometry typical for eutectic microstructures are identified in cavities below the island. The self-assembled network of line nanostructures also shows Al-rich inclusions covered by a thin layer of Si. All detected Al-rich inclusions can be attributed to residual Al-Si eutectic, which could not be etched off in boiling HCl due to its protected location.

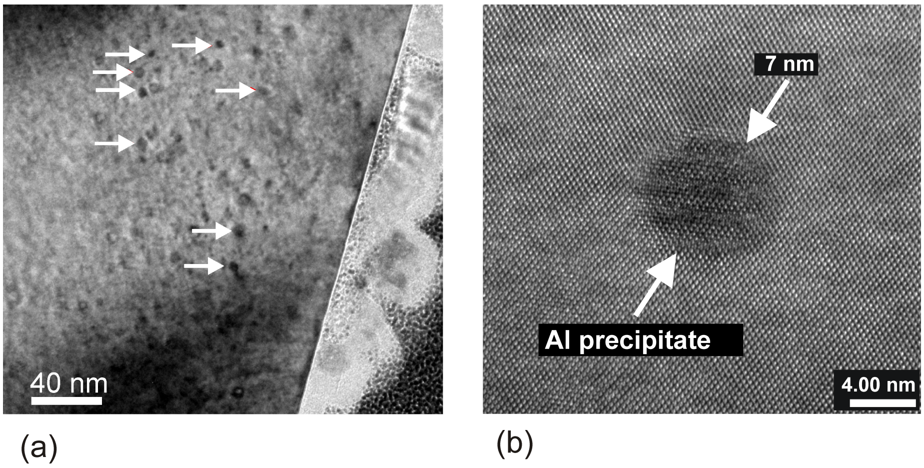

Figure 2.10.: *(a) Cross-sectional TEM bright-field image showing precipitates as dark dots within the crystalline silicon bulk of the island; some of the precipitates are marked by arrows. (b) Cross-sectional HRTEM image of a crystalline Al precipitate within the crystalline Si matrix of an island on the Al-*p^+ *surface. The precipitate is fully embedded into the silicon matrix and shows a Moiré contrast due to different lattice parameters.*

Figure 2.10 (a) shows a bright-field TEM image taken near the surface of an island as shown in Figure 2.5 (b). Numerous dark spots (white arrows) can be observed within the silicon matrix. From the high resolution TEM image of one selected dark spot, as depicted in Figure 2.10 (b), a clear Moiré pattern can be identified, which is attributed to the lattice mismatch between the Al precipitate and the Si matrix, thus the precipitates are crystalline and fully incorporated into the silicon matrix. From the HRTEM micrograph the diameter of the precipitates is determined to be $\leq$ 7 nm. The precipitates are also analyzed by EDX measurements proving their aluminum content. The nano-precipitates are only present within the bulk of the islands but cannot be observed in the bulk of the Al-p^+ region, which indicates that the Al-p^+ region is completely defect-free.

Figure 2.11 shows a cross-sectional STEM dark-field image of two precipitates appearing as bright spots which were analyzed with the EDX method. The corresponding EDX line scan along

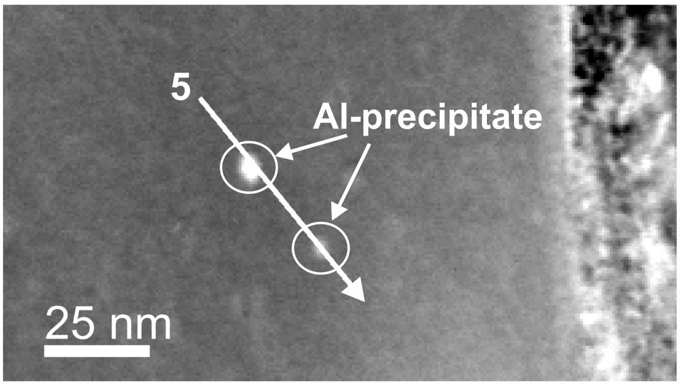

Figure 2.11.: *Cross-sectional dark-field STEM image of two crystalline Al precipitates appearing as bright spots. The line labeled 5 indicates the position of the EDX line scan shown in Figure 2.12.*

line 5 of Figure 2.11 is shown in Figure 2.12 indicating an enhanced Al-signal at positions of the bright spots of the STEM signal. From this correlation it can be concluded that the precipitates are highly Al-rich. However, this analysis does not show chemical compositions, particularly the precipitates are fully embedded into the silicon matrix making a quantitative EDX analysis more difficult if not impossible in that case, and hence it is not clear if this is metallic aluminum, a silicate or any other crystalline Al-rich composition. Figure 2.13 (a) shows a typical aluminum

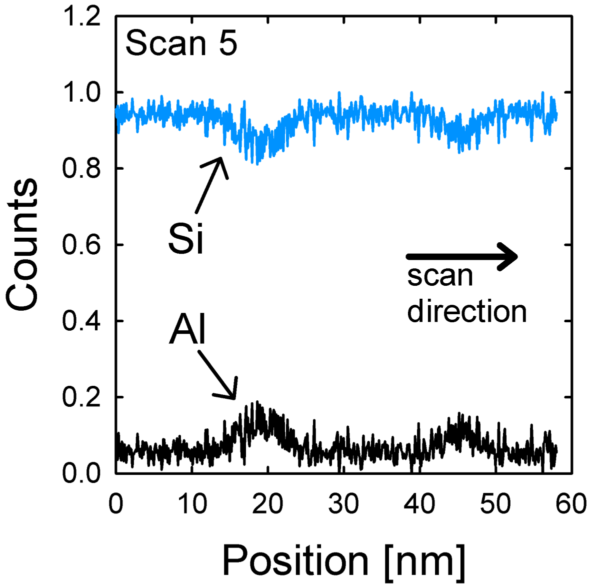

Figure 2.12.: *EDX line scan along line 5 of Figure 2.11 showing an enhanced Al signal at positions of the Al precipitates depicted in Figure 2.11.*

doping profile measured by ECV after the residual Al paste and the Al-Si eutectic have been removed in boiling HCl. In addition, an aluminum doping profile after a 15 s etching step in an $HNO_3/CH_3COOH/HF$ (6:1:1) solution is shown.

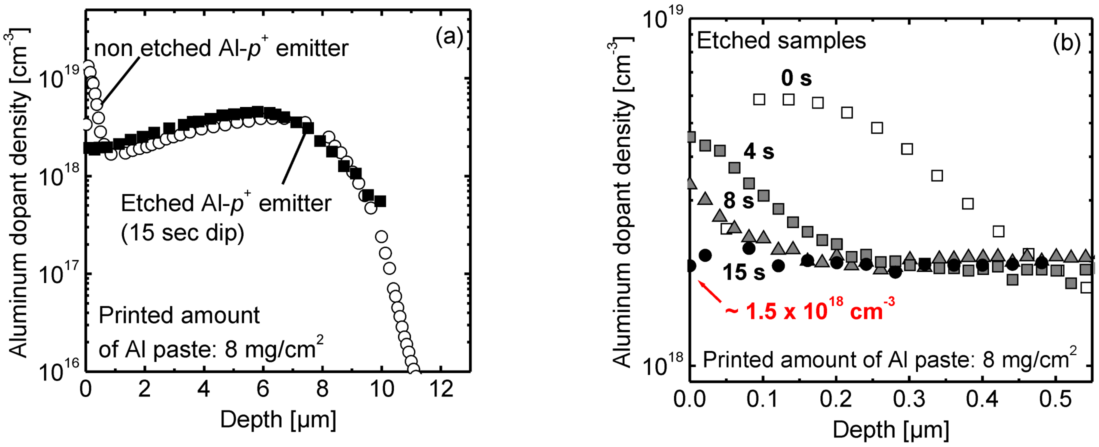

Figure 2.13.: *(a) Comparison of the Al doping profile before and after a 15 s etching step of an Al-p^+ region measured by the ECV method. During the etching, the Al-rich islands and line networks on the surface are removed. The profile after etching shows no concentration peak at the surface. (b) The doping profiles after 0, 4, 8, and 15 s etching show a gradual disappearance of the apparent doping concentration peak at the surface.*

The surface concentration peak is completely removed by the short etching step, whereas the total profile depth and concentration characteristics are the same as before the etching. Figure 2.13 (b) shows the dependence of the concentration peak characteristics after etching times of 0 s, 4 s, 8 s, and 15 s, where the original concentration peak shows a maximum dopant concentration of 6×10^{18} cm^{-3}. The doping profiles at 4, 8, and 15 seconds show a gradual disappearance of the aluminum peak close to the surface. Finally, after 15 s of etching, the apparent concentration peak is completely removed and the surface doping concentration of the screen-printed Al-p^+ region is determined to be 1.5×10^{18} cm^{-3}. The second peak of the doping concentration in the junction region is, as determined from Figure 2.13 (a), 4.5×10^{18} cm^{-3} at a depth of 6 μm.

2.1.3. Discussion

In order to measure Al doping profiles of screen-printed Al-p^+ regions by SIMS or ECV profiling, the residual Al paste with the Al-Si eutectic is removed, which is typically done in a boiling solution of HCl, leaving the Al-rich surface islands and line networks unaltered. An aluminum doping profile from such samples measured with the ECV or SIMS method shows a concentration peak at the surface [54, 66, 67], whereas a doping profile measured with the Spreading Resistance (SR) method does not show this concentration peak [68]. In the case of the SR measurement technique, the resistance measurement is taken from the beveled surface along a line perpendicular to the original sample surface where the islands and line networks are. Thus, the SR measurement does not always end within a small Al-rich surface island. Moreover, the small Al-rich surface islands do not affect the measured overall sheet resistance and thus have no influence on the SR measurement. For the SIMS measurement method, where the total aluminum content is measured, the doping concentration measured from the surface is a mixture of the doping concentration from the Al-p^+ surface and of the Al concentration from the surface islands and line-networks on top of the Al-p^+ surface. Due to the high concentration of electrically inactive aluminum in this region, the profile shows a significantly higher Al concentration than what is electrically active in the Al-p^+ region. In the case of the ECV measurement method, where the electrically active doping concentration is measured, the concentration is assumed to be correct and not affected by the high Al content in the surface islands, however, the doping concentration analysis is always performed assuming a fixed etch area, which is defined by the sealing ring geometry of the measurement equipment. Hence, the enhanced Al signal at the surface can be attributed to the enlarged surface area due to the additional surface of the islands and line networks. From calculations using the surface island geometry of Figure 2.5 (b) a surface area enlargement of $\sim$60% is estimated. A reevaluation of the ECV data assuming a surface area enlargement of 60% results in a surface doping concentration of $\sim 2.3\times10^{18}$, which is in good agreement with the measured doping concentration of $\sim 1.5\times10^{18}$ after the islands have been removed from the surface. During electrochemical etching of the Al-p^+ surface, and thus of the islands, the measured overall surface area becomes gradually smaller until all islands and the line-networks have been removed and the measurement results in the true Al-p^+ doping profile.

Based on the experimental results of this work it can unambiguously be concluded that Al inclusions found within the islands and line-networks on top of the Al-p^+ surface are the cause for the observed apparent Al doping concentration peak at the surface of screen-printed Al-p^+ regions typically detected in SIMS and ECV measurements. For our investigations a frit-free paste was used to form the Al-p^+ region. However, doping profiles measured from Al-p^+ regions fabricated using pastes including frits show similar doping profile characteristics with an apparent concentration peak at the surface, thus our results also apply for pastes with frits.

2.2. Recombination lifetimes in screen-printed Al-doped p^+ regions

Very low carrier lifetimes are typically measured in aluminum-doped Czochralski-grown silicon (Al-doped Cz-Si) wafers. The low lifetimes have been attributed to a very recombination-active defect complex composed of aluminum and oxygen [69]. The defect properties of this Al-O complex were recently determined using temperature- and injection-dependent lifetime spectroscopy (TIDLS) in combination with deep-level transient spectroscopy (DLTS) [70, 71]. The dependence of the low-injection lifetime τ_n in Al-doped (p-type) Cz-Si as a function of the Al doping concentration N_{dop} has, however, not been reported so far. Figure 2.14 shows the inverse lifetime $1/\tau_n$ as a function of doping concentration N_{dop} measured on Al-doped Cz-Si wafers of different doping concentrations (circles). A fit to the measured data results in the following expression:

$$\frac{1}{\tau_n} = 2.8339 \times 10^{-24} {N_{\text{dop}}}^{1.5048}, \tag{2.1}$$

where N_{dop} is given in units of cm^{-3} and τ_n is given in units of μs.

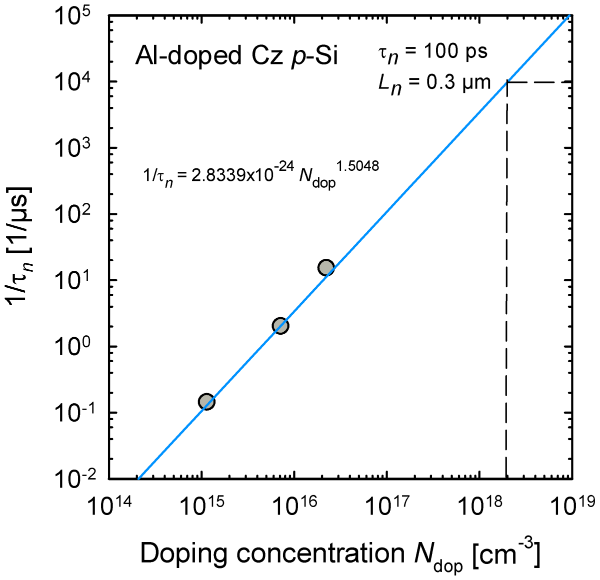

Figure 2.14.: *Inverse lifetime $1/\tau_n$ as a function of doping concentration N_{dop} measured on Al-doped Cz-Si wafers of different doping concentrations (circles). The line shows the fit of a power law to the measured data.*

The inverse lifetime $1/\tau_{\text{n}}$, which is directly proportional to the concentration of the Al-O complex, increases with ${N_{\text{dop}}}^{1.5}$. Extrapolating this dependence to a doping concentration of N_{dop} = 2×10^{18} cm^{-3}, which is typical for screen-printed Al-p^+ regions (used as back surface field in

p-type silicon solar cells and as p^+ rear emitter in n-type cells [54]), a lifetime of τ_n = 100 ps is obtained, which corresponds to an extremely low minority-carrier diffusion length of only L_n = 0.3 μm within the Al-p^+ region. According to Figure 2.14, a lifetime of only 100 ps in the Al-p^+ emitter of an n-type silicon solar cell limits the open-circuit voltage V_oc of the cell to a value below 580 mV! This value is well below the V_oc of 649 mV, which has been experimentally realized in this work [see Chapter 4], suggesting that the lifetime in the screen-printed Al-p^+ silicon region is much larger than expected from the extrapolation of the lifetime data measured on Al-doped Cz-Si. In this Section, the recombination lifetime in Al-p^+ regions is determined from internal quantum efficiency (*IQE*) measurements on specially designed test structures combined with numerical simulations.

2.2.1. Experimental

In order to verify the latter hypothesis, the test device shown in Figure 2.15 has been developed. The main idea is to diffuse a highly phosphorus-doped n^{++} emitter into the screen-printed Al-p^+ silicon region and evaluate the internal quantum efficiency of the n^{++}/Al-p^+ junction. As substrate a 250 μm thick n-type float-zone silicon wafer with a low doping concentration of 4.5×10^{14} cm^{-3} is used.

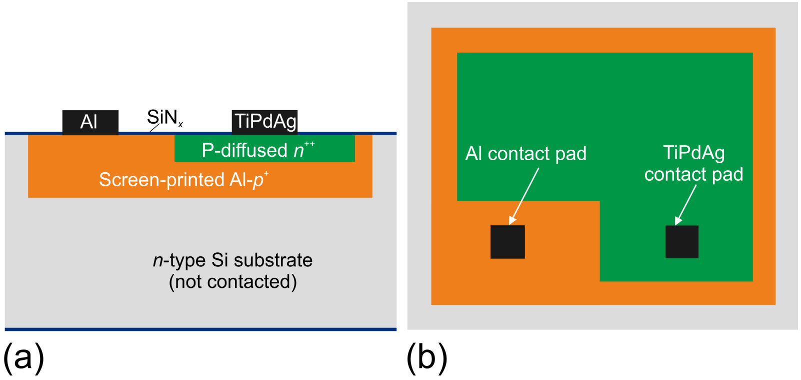

Figure 2.15.: *(a) Cross-sectional view and (b) top view of the test device developed to determine the lifetime in the screen-printed Al-p$^+$ region from measurements of the internal quantum efficiency.*

Figure 2.16 shows the ECV doping profile of the test device after phosphorus diffusion of the n^{++} emitter. The Al-p^+ region has a thickness of W = 6 μm after removing the remaining aluminum paste from the surface and etching off about 2 μm of silicon. The sheet resistance of the Al-p^+ region after etching is $\sim$70 $\Omega/\square$. Note that due to the temperature dependence of the solid state solubility of aluminum in silicon, there is a doping gradient within the Al-p^+ region leading to the formation of an advantageous electric field, which has to be taken into account in the device simulations below. The largest Al doping concentration of 4×10^{18} cm^{-3} is measured at the interface with the n-type silicon substrate, whereas the lowest aluminum concentration of 1.7 $\times$ 10^{18} cm^{-3} is obtained at the surface. The phosphorus diffusion is performed in an open quartz-tube furnace at 860°C using POCl3 gas. The n^{++} emitter at the front surface of the test device has a depth of 300 nm and a surface doping concentration of 2 $\times$ 10^{20} cm^{-3}, overcompensating the Al doping concentration of 1.7 $\times$ 10^{18} cm^{-3}. The resulting sheet resistance of the n^{++} emitter is 60-80 $\Omega/\Box$.

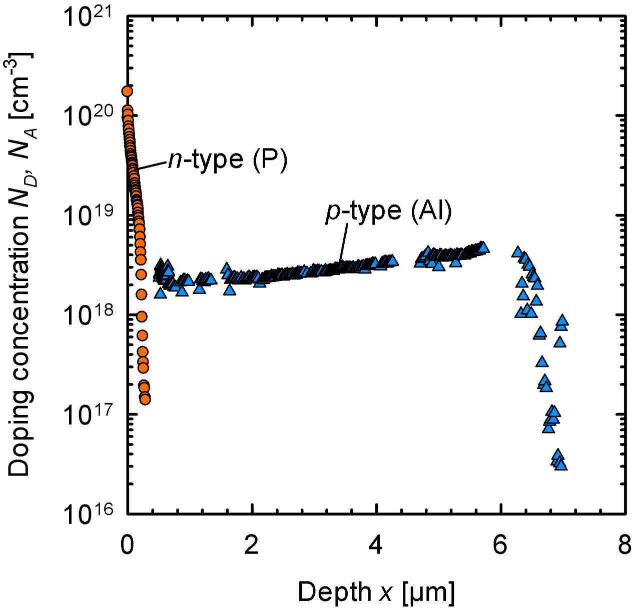

Figure 2.16.: *Doping profile of the n^{++}/Al-p^+ junction measured by the ECV technique.*

2.2.2. Internal quantum efficiency (*IQE*) analysis

Figure 2.17 shows the measured internal quantum efficiency IQE as a function of wavelength λ (symbols). The lines are calculated using PC1D by varying the Shockley-Read-Hall (SRH) lifetime τ_{Alp^+} in the Al-p^+ region. In order to include the impact of the electric field in the Al-p^+ region, which amounts to ~2.7 kV/m, the measured Al doping profile is implemented into the PC1D simulations. Also the doping profile of the n^{++} region is taken into account using the ECV-measured profile. For the n-type float-zone silicon substrate it is assumed that the lifetime is limited only by Auger and radiative recombination, i.e., a bulk lifetime τ_b of 37 ms [72] is assumed. Front and rear surfaces of the substrate wafer are passivated by PECVD-SiN$_x$ films with a refractive index of 2.4 (i.e., well-passivating silicon-rich SiN$_x$ [73]). For the surface recombination velocity S_{rear} at the device rear a value of 13 cm/s is used, which has been determined from lifetime measurements on a separate n-type float-zone silicon wafer of the same doping concentration.

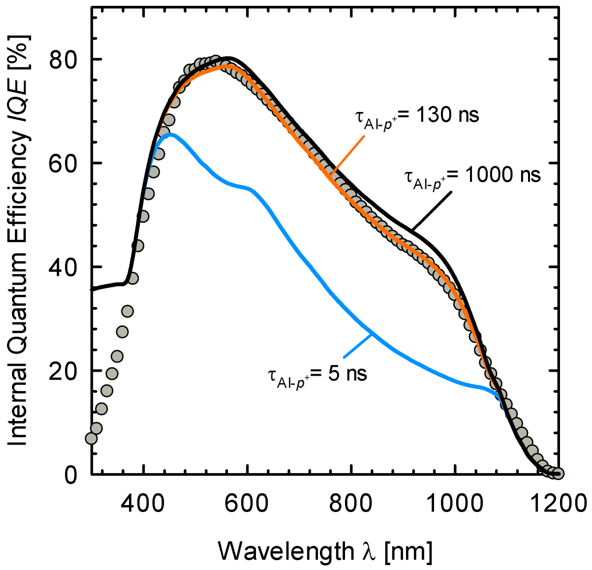

Figure 2.17.: *Measured internal quantum efficiency IQE as a function of wavelength* λ *(symbols) of the test device shown in Figure 2.15. The lines are PC1D simulations for different SRH lifetimes* τ_{Alp^+} *in the Al-*p^+ *region.*

The measured $IQE(\lambda)$ curve (symbols in Figure 2.17) shows a *shoulder* in the wavelength range between 800 and 1100 nm, which is also well reproduced by the PC1D simulation. This shoulder is due to excess electrons generated in the n-type substrate, which are injected from the substrate into the Al-p^+ region and hence contribute to the measured short-circuit current. To verify this, the bulk lifetime in the substrate has been varied in the simulation. A strong decrease in the quantum efficiency for decreasing substrate bulk lifetime is observed in the wavelength range between 800 and 1100 nm corresponding to an absorption depth above 10 μm in silicon. On the other hand, for wavelengths below 600 nm (absorption depth $<$ 2.5 μm) the IQE is completely independent of the substrate properties and depends only on the Al-p^+ recombination properties.

As can be seen by comparing the simulated curves (lines) in Figure 2.17 with the measured *IQE* data (symbols), experiment and simulation agree best for a SRH lifetime in the Al-p^+ region of $\tau_{Alp^+} = 130$ ns. This lifetime can be regarded as a lower limit to τ_{Alp^+} since the *IQE* can also be well fitted for higher lifetimes (i.e., $\tau_{Alp^+} > 130$ ns) assuming a reduced bulk lifetime $\tau_\text{b} <$ 37 ms in the n-type silicon substrate. In addition to the SRH lifetime, Auger recombination has to be taken into account in the highly doped Al-p^+ region. As a consequence of the depth-dependent Al doping concentration, this results in a depth-dependent total lifetime $\tau_{\text{Al}p^+\text{.tot}}(x)$. For the maximum Al doping concentration of $N_\text{Al}(W) = 4\times10^{18}$ cm^{-3}, as it is measured at the interface of the Al-p^+ region with the n-type substrate at x=W, a minimum total lifetime of $\tau_{\mathrm{Al}p^+\mathrm{.tot}}(W)$ = 107 ns corresponding to a minority-carrier diffusion length of 8 μm, is determined. At the interface of the Al-p^+ region with the n^{++} emitter (i.e., at x=0), $N_{\mathrm{Al}}(0) = 1.7\times10^{18}$ cm^{-3} and $\tau_{\mathrm{Al}p^+\mathrm{.tot}}(0)$ = 125 ns, which corresponds to a minority-carrier diffusion length of 9.6 μm. Obviously, the diffusion length is much larger than the thickness of the Al-p^+ region. As an additional advantage, due to the presence of the electric field in the Al-p^+ region, there is a drift field pushing the electrons towards the n^{++} emitter. Note that the doping dependence of the band gap narrowing, which is also taken into account in the simulations, leads to a small reduction of the electric field in the Al-p^+ region. The presence of the electric field in the Al-p^+ region leads to an increase in the *IQE*, as can be seen from Figure 2.18, demonstrating the impact of the electric field as a consequence of the Al doping gradient. The blue solid curve shows the simulated curve which best fits the experimental data including the doping gradient. The orange curve was calculated using the same simulation parameters, but assuming a constant Al doping concentration of $N_{\mathrm{Al}} = 3\times10^{18}$ cm^{-3} throughout the Al-p^+ region. Obviously, the electric field leads to a pronounced increase in the *IQE* over the entire relevant wavelength range between 500 and 1000 nm. One may define an "effective" diffusion length in the Al-p^+ region, which includes the positive effect of the doping gradient. This effective diffusion length exceeds the value of 10

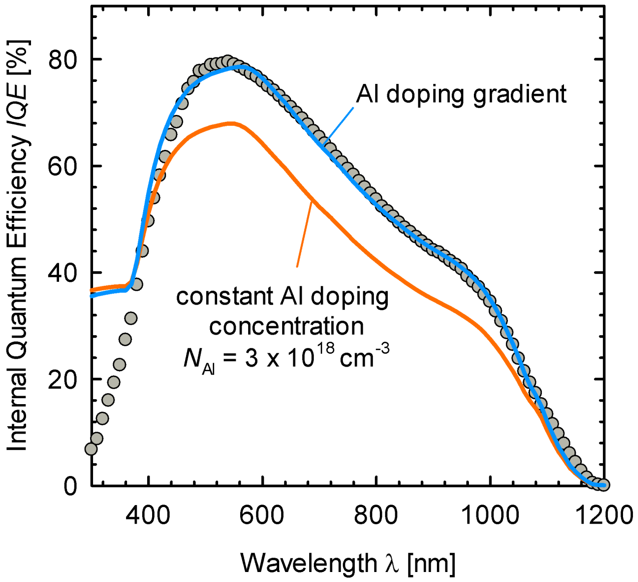

Figure 2.18.: *Measured internal quantum efficiency IQE as a function of wavelength λ (symbols) of the test device shown in Figure 2.15. The lines are PC1D simulations for a SRH lifetime of* τ_{Alp^+} *= 130 ns in the Al-p*$^+$ *region. The blue line is simulated including the ECV-measured Al doping gradient in the Al-p*$^+$ *region, while the orange line is calculated assuming a constant Al doping concentration of* $N_{Al} = 3\times10^{18}$ *cm*$^{-3}$ *and hence no doping gradient.*

μm for the screen-printed Al-p^+ region investigated in this study.

2.2.3. Simulation results and discussion

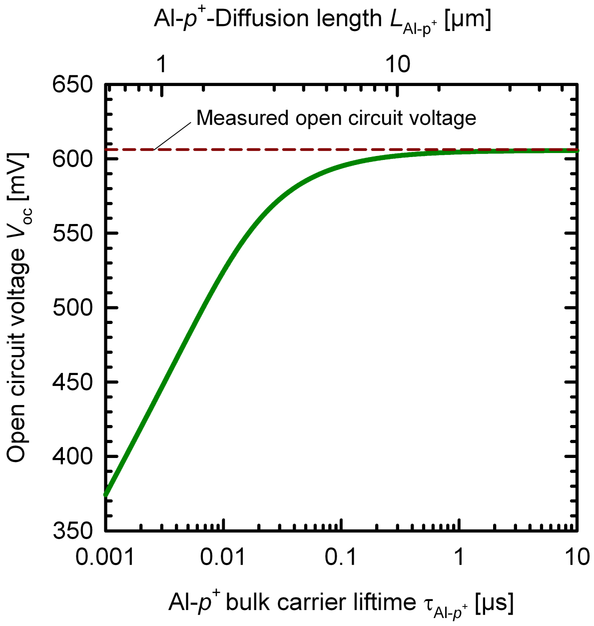

Figure 2.19.: *Simulated open-circuit voltage V_{oc} as a function of the carrier lifetime in the Al-p^+ region τ_{Alp^+} of the test structure shown in Figure 2.15 with a doping concentration of the Al-p^+ region of $N_{Alp^+} = 3\times10^{18}$ cm^{-3}. The dashed line represents the measured V_{oc} of the n^{++}/Al-p^+ junction.*

Figure 2.19 shows the simulated open-circuit voltage V_{oc} and the measured V_{oc} under illumination with a halogen lamp of the n^{++}/Al-p^+ junction. At a temperature of 25°C and a light intensity of 100 mW/cm^2 an open-circuit voltage of $V_{\text{oc}} = (607 \pm 5)$ mV is measured. According to PC1D device simulations, the lower limit to $\tau_{\text{Al}p^+}$ of 130 ns determined from our *IQE* analysis presented in Section 2.2.2 allows to achieve a $V_{\text{oc}} > 600$ mV, which is in agreement with the measured V_{oc} of (607 ± 5) mV. Note that the relatively high V_{oc} measured at the n^{++}/Al-p^+ junction also suggests that the phosphorus-diffused and SiN$_x$-coated surface provides a good level of surface passivation on Al-p^+ regions.

2.2.4. Efficiency limits

Figure 2.20 shows a sketch of the simulated solar cell structure featuring a passivated Al-p^+ region as rear emitter (the so-called ALU$^+$ solar cell concept, see Chapter 4). The n^+ front surface field is assumed to be well passivated (front surface recombination velocity $S_{\text{front}} = 1000$

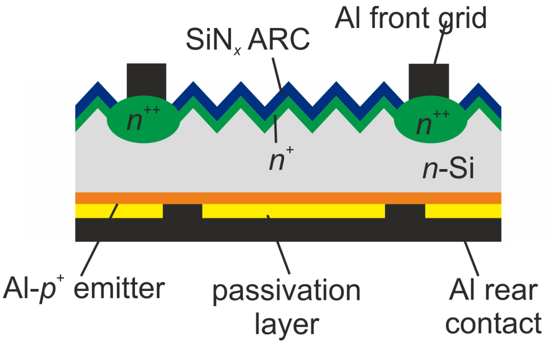

Figure 2.20.: *High-efficiency n-type silicon solar cell with passivated screen-printed Al-p^+ rear emitter (ALU$^+$ cell).*

cm/s) and a deep n^{++} diffusion is implemented under the metal contact grid lines. The rear is completely covered by a passivated Al-p^+ emitter. The dielectric passivation layer is locally opened and the rear is fully metalized. A rear surface recombination velocity of S_{rear} = 800 cm/s is assumed, which has been experimentally realized for an amorphous silicon-passivated boron-diffused p^+ emitter of comparable surface doping concentration (2×10^{18} cm^{-3}) [74].

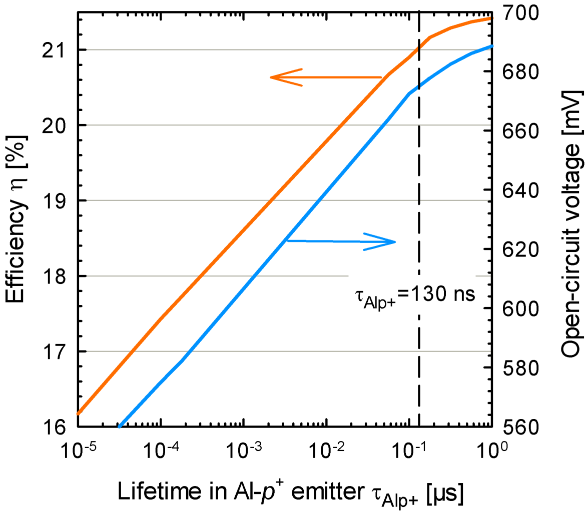

Figure 2.21.: *Simulated efficiency η and open-circuit voltage V_{oc} as a function of the lifetime τ_{Alp^+} in the Al-p^+ emitter for the ALU$^+$ solar cell shown in Figure 2.20 [PC1D simulation parameters: cell thickness 200 µm, series resistance R_s = 0.5 Ωcm^2, 3 Ωcm n-type silicon base, base lifetime τ_b = 3 ms, 3 µm thick Al-p^+ rear emitter, rear surface recombination velocity S_{rear} = 800 cm/s, 100 Ω/sq n^+ front surface field, S_{front} = 1000 cm/s].*

Figure 2.21 shows the simulated efficiency η and open-circuit voltage V_{oc} as a function of the SRH lifetime τ_{Alp^+} in the Al-p^+ emitter for the ALU$^+$ cell shown in Figure 2.20. Using the lifetime of $\tau_{\mathrm{Al}p^+}$ = 130 ns obtained from the above *IQE* analysis an efficiency η of 21% and a V_{oc} of 670 mV are feasible using a screen-printed Al-p^+ rear emitter.

2.3. Thermally activated defects in screen-printed Al-p^+ regions

In the previous Section it was shown that Al-O complexes which form at elevated temperatures (>900°C) during the cooling of the Cz-Si ingot are the most probable reason for the extremely low carrier lifetime in Al-doped Cz-Si. Extrapolation of Equation 2.1 to a doping concentration of $N_{\mathrm{dop}} = 2\times10^{18}$ cm^{-3} typically measured in Al-p^+ regions in Si solar cells, leads to an extremely low lifetime of $\tau_n = 1\times 10^{-4}$ μs (see Figure 2.14). This is in contradiction to the extracted upper limit of the carrier lifetime of $\tau_n = 0.13$ μs within such highly Al-doped p^+-regions fabricated by means of screen-printing and short firing as it has been found in Section 2.2. Thus, the lifetime is obviously much higher in screen-printed Al-p^+ regions than in Al-doped Cz-Si material. In this Section we try to find the reason for this huge difference in carrier lifetimes.

We investigate the impact of high-temperature treatment on the formation of recombination-active Al-O complexes and thus on the carrier lifetime in screen-printed Al-p^+ regions by means of saturation current density measurements (J_0). Using the measured J_0 values and SENTAURUS [75] numerical device simulations the activation energy E_{a} of the relating defect is determined. First, a detailed description of the experimental procedure is given followed by the results of the J_0 measurements and the determination of the activation energy E_{a}.

2.3.1. Experimental

Sample preparation

Figure 2.22 shows an overview of the used materials and thermal treatments applied to the samples in this experiment. One group of samples consists of Cz-Si material and a second group of FZ-Si material. Both groups are divided into two sets, where one set is thermally oxidized and the second set is annealed in a nitrogen atmosphere. The saturation current density is measured before and after the thermal treatment.

As base material single-crystalline shiny-etched (100)-oriented 300 μm thick quasi-intrinsic p-type float zone (FZ) silicon with a boron doping concentration of 6.6×10^{13} cm^{-3} (200 Ωcm) and an oxygen concentration $< 10^{15}$ cm^{-3} and very lowly doped (100)-oriented 200 μm thick n-type Czochralski-grown (Cz) silicon wafers with a phosphorus doping concentration of 1.8×10^{14} cm^{-3} (25 Ωcm) and an interstitial oxygen concentration of $(7.5\pm0.5)\times10^{17}$ cm^{-3} are used. In order to extract the saturation current density J_0 of the Al-p^+ region, the p^+ region is fabricated only on one side of the wafer, while the other surface of the sample is well passivated by PECVD-SiN$_x$. The processing sequence is as follows: (i) After RCA cleaning a 100 nm thick SiN$_x$ layer is deposited on one side with a refractive index of $n = 2.05$. (ii) Subsequently, a non-fritted Al paste is screen-printed on the opposite surface of the wafer with an amount of 8 mg/cm^2. (iii) To vaporize the organic solvents in the Al paste, the screen-printed samples are

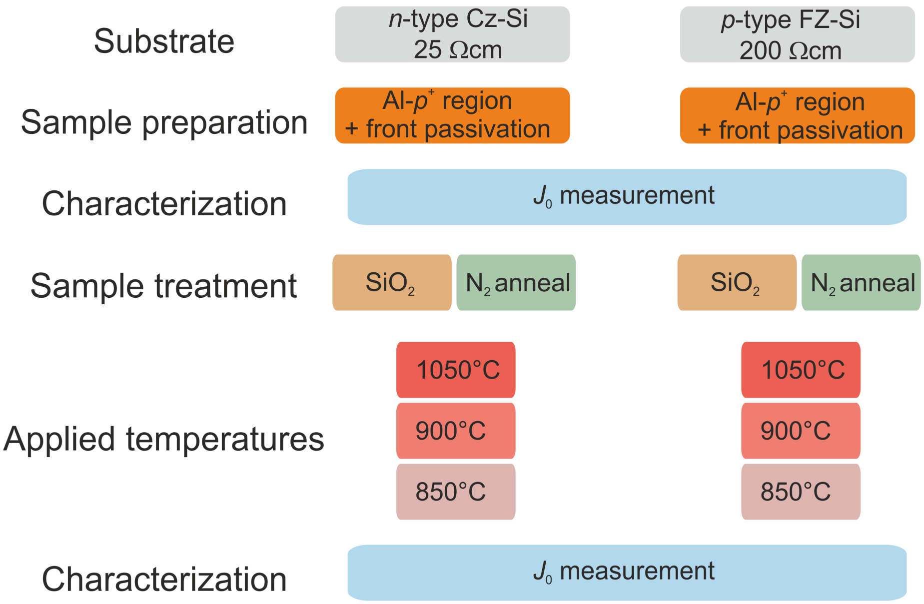

Figure 2.22.: *Illustration of the experimental procedure for the analysis of the lifetime degradation in the Al-p^+ bulk during thermal treatment.*

dried in a belt dryer at 150°C for 10 min. (iv) Finally, the Al-doped p-type region is formed in a *Radiant Technologies Corporation LA-310* infrared conveyor belt furnace at a measured temperature of 780°C for 13 seconds.

For thermal oxidation of the Al-p^+ region the residual Al paste and the Al-Si eutectic are removed from the surface in a boiling 37 % solution of hydrochloric acid. There is a pronounced peak in the doping profile of screen-printed Al-p^+ regions near the surface. As described in Section 2.1 this peak is caused by Al-rich surface structures that remain after the removal of both the residual Al paste and the eutectic composition. This apparent concentration peak in the doping profile is etched back by 3 μm in a 50% KOH solution at 70°C. Then, after the PECVD-SiN$_x$ has been removed from the front side by an HF dip (20%, 5 min) the samples receive an RCA cleaning and are thermally oxidized in a quartz tube furnace using a dry oxidation in O_2 at 1050°C for 180 min and a wet oxidation in O_2 and H_2 at 900°C for 120 min and at 850°C for 60 minutes. A *Centrotherm CENTRONIC Dotiersystem 2000HT 180-4* quartz tube furnace was used for the oxidations. Subsequently, the SiO_2 is removed only from the non-screen-printed front surface of the sample. Finally, the front surface is passivated by a 70 nm thick PECVD-SiN$_x$ with a refractive index of $n = 2.4$. The samples are now well passivated by a PECVD-SiN$_x$ layer at the front side and have a thermally oxidized Al-p^+ region at the rear side.

One set of Cz-Si and one set of FZ-Si samples featuring the screen printed Al-p^+ regions is oxidized at 1050°C (180 min), 900°C (120 min), and 850°C (200 min). Additionally, a set of Cz-Si as well as FZ-Si samples underwent only an annealing step at 1050°C (180 min), 900°C (120 min), and 850°C (200 min) in nitrogen atmosphere instead of an oxidation (see Figure 2.22), which has also been performed in a *Centrotherm CENTRONIC Dotiersystem 2000HT 180-4* quartz tube furnace.

Saturation current density measurements

The saturation current densities J_0 are obtained from transient photoconductance decay (PCD) measurements using a *Sinton Instruments WCT-100* lifetime tester [76]. Figure 2.23 shows a schematic of the measurement setup which has been used in this work for the PCD measurements. With this method the photoconductance of a silicon wafer is measured with a calibrated radio-frequency (rf) bridge circuit. An rf coil which is part of a resonant circuit operating at a fixed frequency of 10.7 MHz induces eddy currents in the test sample. These eddy currents in turn induce an additional voltage in the coil. This additional voltage is a function of the sample conductance. Once the measurement unit is calibrated by determining the output voltage of the rf circuit as a function of the dark conductance of wafers with different known base doping concentrations, the system can be used to analyze the absolute photoconductance of a wafer. By illuminating the sample with a short light pulse of generation rate $G(t)$ its photoconductance will rise in accordance to the generated excess charge carries Δn. The carrier lifetime is then determined from the decaying photoconductance signal monitored by the oscilloscope as a function of time after termination of the optical generation. The effective carrier lifetime τ_{eff} is now determined from the mono exponential decay of Δn. A detailed explanation of the measurement method including the corresponding calculations of Δn and τ_{eff} is given elsewhere [77–81].

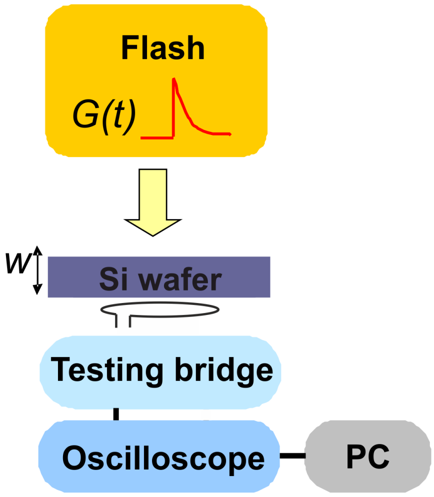

Figure 2.23.: *Schematic of the measurement setup used for the photoconductance decay carrier lifetime measurments.*

The saturation current density J_0 is extracted from the measured injection-dependent lifetime data by plotting the reciprocal effective lifetime $1/\tau_{\text{eff}}$ versus the excess carrier concentration Δn using an equation as derived by Kane & Swanson for an asymmetric sample structure [82]:

$$\frac{1}{\tau_{\text{eff}}} = \frac{1}{\tau_{\text{bulk}}} + \frac{S_{\text{SiN}}}{W} + \frac{J_0 \Delta n}{q n_i^2 W}, \tag{2.2}$$

where W is the wafer thickness and $n_i = 1 \times 10^{10}$ cm^{-3} is the intrinsic carrier concentration of silicon at 300 K, τ_{eff} is the effective carrier lifetime and τ_{bulk} the bulk carrier lifetime. S_{SiN} is the surface recombination velocity of the SiN_x passivated illuminated front side of the sample and q is the elementary charge. It is assumed that the excess carrier concentration Δn is uniform throughout the base, which is not strictly valid for large surface recombination velocities. Due to the given asymmetry between the front and the rear side of the sample the emitter saturation current density tends to be underestimated up to 10% in the worst-case scenario [82]. Due to the low base doping concentration of 6.6×10^{13} cm^{-3} of the used FZ-Si material, all lifetime measurements are performed under high-injection conditions. J_0 is extracted in a Δn range of (1-8) $\times$ 10^{15} cm^{-3}. As Auger recombination is not significant at these relatively low injection levels, the measured lifetime data is not Auger-corrected in our particular case. The saturation current density has been measured before and after the thermal treatment of the samples as shown in Figure 2.22.

2.3.2. Results

To quantify the degradation caused during oxidation, the J_0 value of the Al-p^+ region of the Cz-Si samples is measured after passivation by thermally grown SiO_2 at 1050°C, 900°C, and 850°C, respectively.

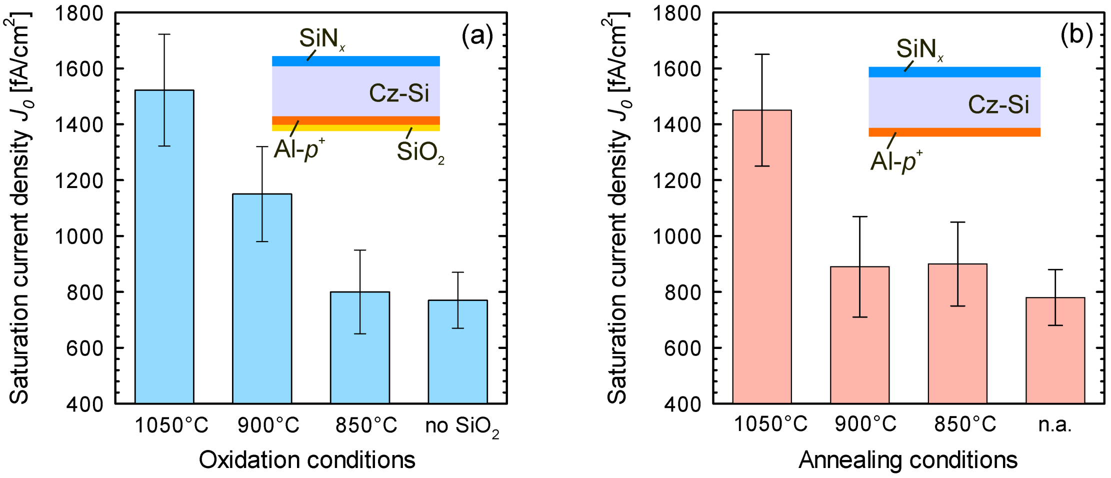

Figure 2.24.: *Measured saturation current densities J_0 as a function of oxidation temperature measured on Al-p^+ emitters fabricated on Cz-Si material. (b) Measured J_0 as a function of annealing temperature without addition of oxygen.*

The measured saturation current densities of the Cz-Si samples annealed in O_2 ambient and of the Cz-Si samples annealed in N_2 ambient are shown in Figures 2.24 (a) and (b). A J_0 value of (1522 ± 300) fA/cm^2 is obtained after oxidation at 1050°C, a J_0 of (1150 ± 220) fA/cm^2 after the 900°C oxidation and a J_0 of (800 ± 140) fA/cm^2 after 850°C oxidation, indicating a pronounced lifetime degradation in the Al-p^+ region at temperatures $\geq$ 900°C. For comparison, the J_0 value of a fired and etched-back (non-oxidized) sample is also included in Figure 2.24 showing a J_0 value of (780 ± 150) fA/cm^2.

Figure 2.24 (b) shows the J_0 values measured from the second set of the Cz-Si samples. However, these samples were not oxidized, they were exposed to the same thermal profile (1050°C, 900°C, and 850°C) in a nitrogen atmosphere. Again, a significant lifetime degradation of the Al-p^+ region is observed at 1050°C, where J_0 = (1450 ± 280) fA/cm^2 is measured. At temperatures lower than 900°C the J_0 is in the range of a fired and etched-back sample (non annealed), indicating no lifetime degradation of the Al-p^+ region. Thus, for Cz-Si material there is no influence of the ambient on the lifetime degradation. To elucidate the role of the oxygen in the Cz material, some of the above experiments were repeated on FZ samples. The measured J_0 values are compiled in Figure 2.25. They are all in the range of an untreated Al-p^+ region with J_0 = (780 ± 150) fA/cm^2 and decrease slightly towards lower oxidation temperatures. At 850°C a J_0 of (580 ± 116) fA/cm^2 is obtained. This reduction in J_0 is probably due to a passivation of the Al-p^+ surface by the thermally grown silicon dioxide.

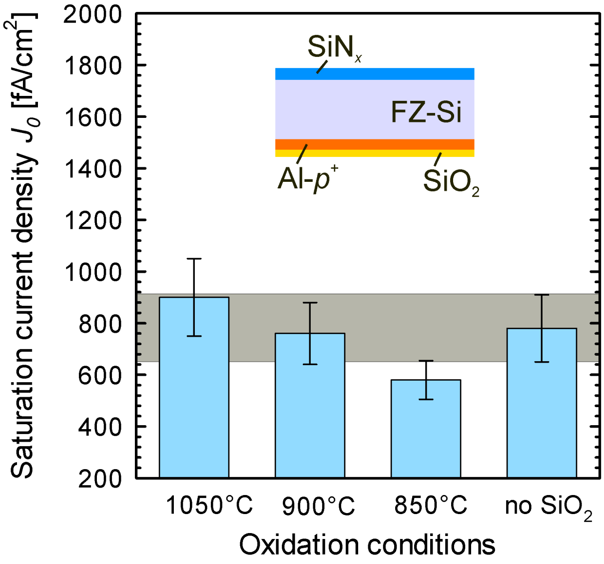

Figure 2.25.: *Measured saturation current densities J_0 as a function of oxidation temperature measured on Al-p^+ emitters fabricated on FZ-Si material.*

2.3.3. Activation energy of the aluminum-oxygen defect formation

In the following, the experimental findings are interpreted by means of numerical device simulations. A basic model published in Ref. [83, 84] is used with the following addition: To describe the lifetime degradation, Equation 2.1 presented in Section 2.2 is multiplied with a factor f to describe, which fraction of the Al-O concentration is formed during thermal treatment relative to the case of Al-doped Cz-Si wafers. Thereby, it is assumed that a maximum amount of Al-O complexes is formed during the Cz process, where $f = 1$. In contrast, the screen-printed Al-p^+ regions are characterized by $f < 1$ because of their limited thermal budget. In the simulation of the above J_0 measurements, f is the only free parameter and can be extracted from a comparison between the simulated and experimental J_0. The striking simulation result is that all of the above measured J_0 values are dominated by recombination losses in the bulk and not at the surface. With the simulated factor f and the applied duration of thermal treatment t_{th} the generation rate R_{gen} of the Al-O complex is determined to be:

$$R_{\text{gen}} = \frac{ln(1-f)}{t_{\text{th}}}. \tag{2.3}$$

Figure 2.26 shows an Arrhenius plot of the generation rate R_{gen} as a function of the inverse temperature $1/T$.

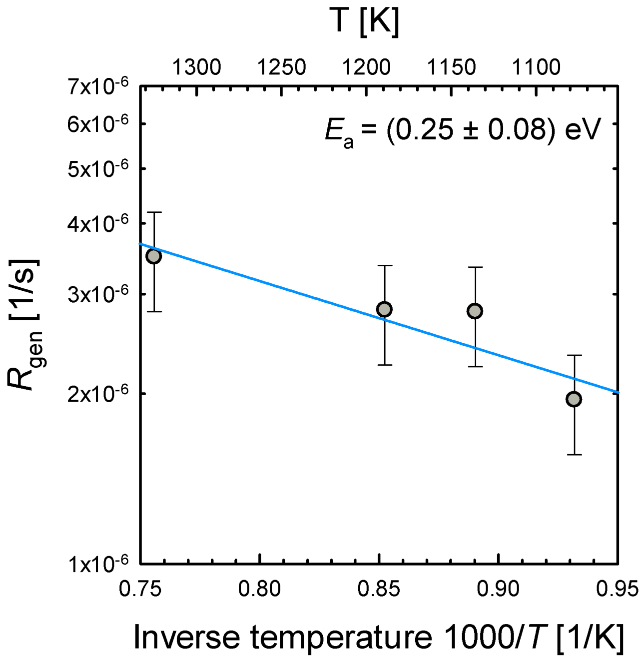

Figure 2.26.: *Al-O defect generation rate R_{gen} as a function of the inverse temperature in an Arrhenius plot. The calculated activation energy E_a of the Al-O complex formation is determined to be E_a = (0.25 ± 0.08) eV.*

The fact that the data can be well fitted by an Arrhenius law

$$R_{\mathrm{gen}} = \nu_0 exp\left(-\frac{E_{\mathrm{a}}}{k_{\mathrm{B}}T}\right), \tag{2.4}$$

where ν_0 is the pre-exponential factor, k_{B} is the Bolzman´s factor, T is the temperature, and E_{a} is the activation energy, indicates that the formation of Al-O complexes in screen-printed Al-doped p^+ regions during a high-temperature treatment is a thermally activated process. To extract the activation energy of the process, a least-square fit of Eq. (2.4) to the measured data is carried out. This results in an activation energy E_{a} = (0.25 ± 0.08) eV and a pre-exponential factor of $\nu_0 = 3.3 \times 10^{-5}\mathrm{s}^{-1}$.

2.3.4. Discussion

From the analysis of our experimental results it is concluded that two prerequisites are necessary for a degradation of the lifetime in Al-doped p^+ regions. First, the formation of defects is thermally activated and occurs in detrimental amounts at temperatures above ∼900°C. Second, oxygen has to be present for the defect formation. Both, the extremely low carrier lifetimes in Al-doped Cz-Si wafers [70] as well as the relatively high carrier lifetime in screen-printed Al-p^+ regions can be consistently explained by the formation of recombination-active Al-O complexes. The level of lifetime degradation is then given by the thermal budget and thus by the overall amount of the recombination-active Al-O complexes reaching its maximum during the cooling of the crystal after the high-temperature Czochralski-crystal growth process.

A probable reason for the observed lifetime degradation in screen-printed Al-p^+ regions after a high-temperature treatment is hence the formation of recombination-active Al-O complexes within the Al-p^+ region. Note that a short (∼13 s) firing at temperatures ≤900°C does not cause a significant Al-O complex formation due to the lower temperatures and very short duration of the process. Thus, a nearly defect-free Al-p^+ region explains the very high measured carrier lifetime of τ_n = 130 ns which is close to the Auger-limited carrier lifetime $\tau_{n.Aug}$ = 650 ns at a doping concentration $N_{\mathrm{a}} = 3\times10^{18}$ cm^{-3} [70]. As the oxygen concentration in FZ-Si wafers is below 10^{16} cm^{-3} and the diffusion of oxygen into the Si bulk during thermal oxidation is extremely weak [85], no significant degradation in the Al-p^+ lifetime is observed for the FZ-Si samples, even up to high temperatures of 1050°C.

One speculation explaining the unusually low measured activation energy of the Al-O formation of E_{a} = (0.25 ± 0.08) eV might be that fast-diffusing oxygen complexes such as O_2, O_3, etc., attach to the substitutional immobile Al. It has been shown by first-principles calculations that small-chained oxygen complexes show migration energies down to 0.3 eV [86].

2.4. Chapter summary

We have demonstrated that the doping profile of screen-printed Al doped p^+ regions show a pronounced apparent peak at the surface. The measured carrier concentration of $\sim 10^{19}$ cm^{-3} is about one order of magnitude above the solid solubility of Al in Si at the corresponding temperature during alloying ($\sim 10^{18}$ cm^{-3}). This apparent concentration peak has already been presented in the literature e.g. by Lölgen in 1993 [62] and Huster in 2006 [64] and it had been attributed to aluminum-rich structures on the surface, a working hypothesis, which however has never been experimentally confirmed. In this Chapter, a detailed microscopic investigation and elemental analysis of surface structures and line-networks was presented for the first time. As a key result the Al-p^+ region is epitaxially grown and of very high quality without any crystallographic defects in the bulk of the Al-p^+ region. Aluminum inclusions were found $\sim$50 nm beneath the silicon surface of islands, which remain on the surface after removal of the residual Al paste and the Al-Si eutectic in boiling HCl. Furthermore, by using HRTEM, STEM and EDX analysis, Al nano-precipitates of $\leq$7 nm diameter were localized within the bulk of the islands on the Al-p^+ surface. Additionally, Al inclusions of about 30 nm diameter covered by a thin silicon layer were found within the self-assembled network of line-like nanostructures on top of the Al-p^+ surface. It was shown that these Al inclusions are the cause of the concentration peak.

The experimental results of this work suggest that the Al-O complex limiting the lifetime in Al-doped Cz-Si forms at very high temperatures (>900°C) during the cooling of the Cz ingot. Using *IQE* measurements and numeric device simulations the charge carrier lifetime in Al-p^+ regions was extracted for the first time to be 130 ns, which is about 3 orders of magnitude lower than lifetimes measured in Cz-grown Al-doped silicon. Simulations showed that the SRH lifetimes of 130 ns in Al-p^+ regions enable open-circuit voltages of 670 mV and efficiencies of 21% on *n*-type silicon wafers. This result suggests that the Al-O complex limiting the lifetime in Al-doped Cz-Si forms at very high temperatures (>900°C), whereas the conditions during firing of an aluminum paste (a few seconds at a peak temperature < 900°C) do not lead to the formation of the Al-O complex. These results prove that the realistic potential of screen-printed Al-p^+ emitters for the application to high-efficiency *n*-type cells is much higher than traditionally assumed [54].

We have also shown that a temperature treatment at elevated temperatures (900-1050°C), as it is typically used to oxidize the Si surface, can also significantly degrade the lifetime in an Al-p^+ region when fabricated on Cz-Si. This lifetime degradation is directly coupled to the presence of oxygen in the silicon and thus is attributed to the Al-O complex which also limits the carrier lifetime in Al-doped Cz-Si. The activation energy of the Al-O formation was determined to be $E_a = (0.25 \pm 0.08)$ eV.

3. Surface passivation of screen-printed Al-p^+ emitters

The Chapter deals with the surface passivation of screen-printed Al-p^+ regions for the application as emitter in n-type silicon solar cells. The passivation quality of several passivation methods applied to the Al-p^+ emitter surface is investigated by means of emitter saturation current density ($J_{0\mathrm{e}}$) measurements. This approach combines the screen-printed Al-p^+ emitter with an effective surface passivation and thus reduction in emitter surface recombination velocity, which makes the easy-to-fabricate screen-printed Al-p^+ emitter to a realistic alternative to the technologically demanding high-temperature boron diffusion. The Chapter starts in Section 3.1 with a brief introduction into the passivated screen-printed Al-p^+ emitter approach. Section 3.2.1 introduces the processing sequence and gives experimental details of the emitter surface preparation. In Section 3.2.2, the deposition methods and the deposition parameters of the applied passivation layers are presented. The passivation quality is given in terms of $J_{0\mathrm{e}}$ values in Section 3.3, followed by a comparison with literature values in Section 3.4.

3.1. The Al-p^+ emitter passivation approach

Typically, the rear side of a *conventional* n-type silicon solar cell with a screen-printed Al-p^+ emitter is fully metalized due to the residual Al-paste (see Section 1.2.3). This full-area metalization causes a very high emitter surface recombination velocity in the range of 10^6 cm/s which drastically limits the solar cell conversion efficiency. To overcome this limiting factor and to reduce the emitter surface recombination velocity, we apply a surface-passivation to the screen-printed Al-p^+ emitter. However, in order to passivate the emitter it needs to be very clean and in particular free from any metal impurities. In the previous Chapter it was shown that even after the Al-paste is completely removed from the surface, the emitter surface is still covered by aluminum-rich surface islands. These surface islands are not beneficial for the surface passivation. Therefore, we first remove the remaining Al paste from the emitter surface and subsequently etch the emitter back by a few μm. This procedure provides a clean and metal-free emitter surface and allows to deposit a passivation layer to the surface.

3.2. Experimental

3.2.1. Sample preparation

Single-crystalline shiny-etched (100)-oriented 300 μm thick p-type FZ-Si wafers of 200 Ωcm resistivity are used in all passivation experiments. Asymmetric test structures are fabricated for the $J_{0\text{e}}$ measurements, where the p^+-emitter is prepared on one side of the wafer and the other surface of the sample is passivated by SiN_x. After RCA cleaning a 100 nm thick SiN_x layer is deposited by means of remote PECVD. Subsequently, Ferro 5540 (paste A) and DuPont PV322 (paste B) non-fritted aluminum pastes are screen-printed onto the opposite surface with an amount of 8 mg/cm^2. After drying the screen-printed samples at 150°C for 5 min to vaporize the organic solvents in the Al paste, the Al-p^+ region is formed in an infrared conveyor belt furnace as described in Section 1.2.3. All Al-p^+ regions for the passivation experiments were formed in a *Radiant Technologies Corporation (RTC) LT-310* conveyor belt furnace. Additionally, the high-temperature firing step improves the passivation quality of the SiN_x film, achieving surface recombination velocities of $S_{SiN} \leq 10$ cm/s after the short high temperature firing step [87]. In order to passivate the p^+ surface, the residue of the aluminum paste and the aluminum-silicon eutectic are removed from the Al-p^+ region in a boiling 37% solution of hydrochloric acid. Finally, the screen-printed Al-p^+ emitter is passivated by a passivation layer as described in the following Section. Figure 3.1 depicts a schematic of the asymmetric sample structure used for the $J_{0\text{e}}$ measurements.

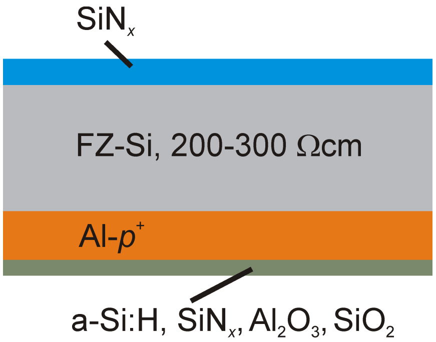

Figure 3.1.: *Sketch of the sample structure which is used for the $J_{0\text{e}}$ measurements. The illuminated front side of the sample is well passivated by PECVD-SiN$_x$ and the Al-p^+-emitter at the rear is passivated by various dielectric layers.*

3.2.2. Deposition techniques

Amorphous hydrogenated silicon (a-Si:H)

Amorphous hydrogenated silicon (a-Si:H) deposited by means of PECVD is well known as a very effective passivation layer for the passivation of highly boron-doped p^+ emitter surfaces [74]. We use an *Oxford Plasma Technology Plasmalab μP* parallel-plate PECVD reactor for the a-Si deposition as depicted in Figure 3.2.

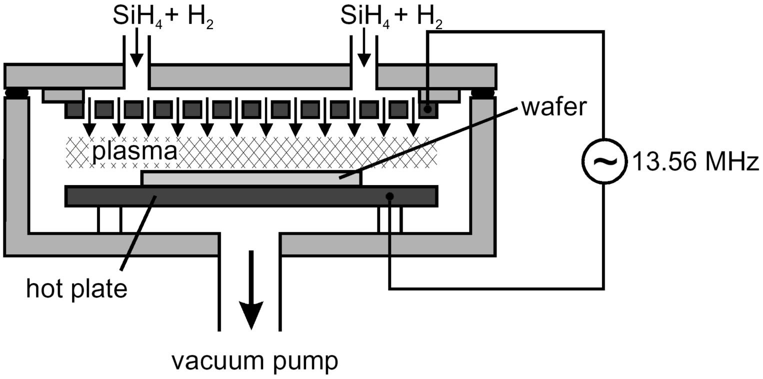

Figure 3.2.: *Schematic of the parallel-plate PECVD reactor used for the a-Si depositions. The SiH_4 gas is excited by an electric field between the upper- and lower electrode. The samples are placed on the heated lower electrode and thus they are in direct contact with the plasma. Figure is taken from Ref. [88].*

In this type of reactor, the samples are placed on the temperature-controlled lower electrode, whereas the process gases silane (SiH_4) and hydrogen (H_2) are injected through the perforated upper electrode. Between the lower and upper electrode the gas is excited by an ac electric field with a frequency of 13.56 MHz. Due to the high-frequency excitation of the ions no noticeable surface damage of the samples is caused, which had been shown to be an important advantage over the low frequency plasma excitation [89].

TABLE 3.1.
SUBSTRATE TEMPERATURE θ_{SUB}, PLASMA POWER P_{PLASMA}, PRESSURE p_{PLASMA}, SIH_4 GAS FLOW $Q_{\mathrm{SIH_4}}$ AND H_2 GAS FLOW $Q_{\mathrm{H_2}}$ USED FOR THE DEPOSITION OF THE A-SI:H FILMS.

	θ_{sub} [°C]	P_{plasma} [W]	p_{plasma} [mTorr]	$Q_{\mathrm{SiH_4}}$ [sccm]	$Q_{\mathrm{H_2}}$ [sccm]
a-Si:H	235	90	450	9	200

At the deposition parameters used in this work (see Table 3.1) the deposition rate is $r_{\text{a-Si:H}} = (10 \pm 2)$ nm/min. The deposited a-Si:H film thickness is characterized by ellipsometry and the ultra-high resolution scanning electron microscopy. J_{0e} measurements are performed directly after deposition and after annealing for 10 min at 350°C. The anneal is interrupted minute by minute for the lifetime measurements. All samples received an RCA cleaning prior to the a-Si:H deposition. Immediately before the deposition a 1 min 1% HF dip is applied to the samples in order to remove the native oxide from the c-Si surface.

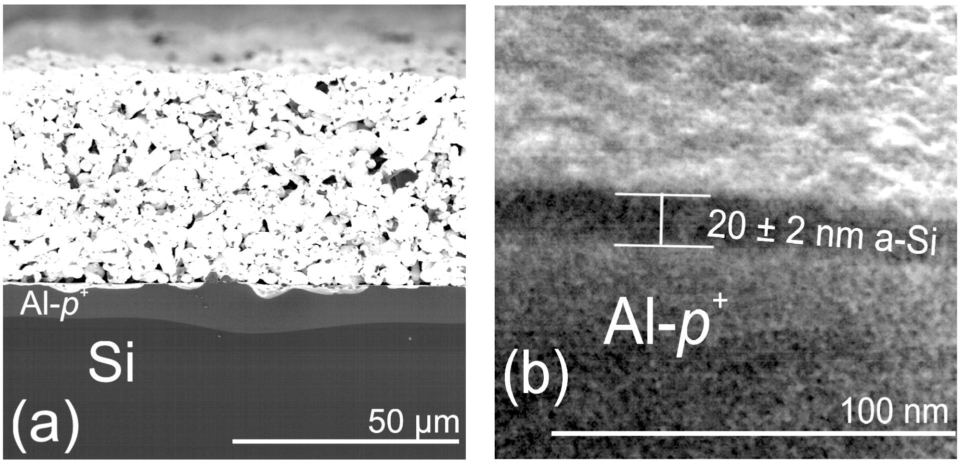

Figure 3.3.: *(a). SEM micrograph of a cross-section of a screen-printed Al-p^+ emitter. The Al-p^+ region is clearly visible as bright contrast below the residual Al paste. The emitter thickness is (8 ± 1) µm. (b) SEM micrograph of a cross section of the Al-p^+ region after etching off the Al and the Al–Si eutectic as well as 3 µm of the Si. The surface is passivated with a (20 ± 2) nm thick a-Si layer.*

Figure 3.3(a) shows a cross-sectional SEM image of a screen-printed Al-p^+ sample obtained from an ultrahigh resolution *Hitachi S-4800* field emission SEM. The Al-doped p^+ region appears brighter than the high-resistivity bulk of the silicon wafer due to the potential contrast [65]. From this image the Al-p^+ depth is determined to be (8 ± 1) μm. Figure 3.3(b) shows an SEM micrograph of the deposited a-Si layer on top of the Al-p^+ region. The a-Si:H layer thickness is determined from this micrograph to be (20 ± 2) nm.

Silicon nitride (SiN$_x$)

After RCA cleaning a PECVD-SiN$_x$ passivation layer is deposited on the Al-p^+ surface at a temperature of 400°C using a commercially available *Oxford Plasma Technology, Plasmalab 80+* remote-downstream PECVD reactor, as depicted in Figure 3.4. In this type of reactor the samples are placed on a temperature-controlled hot plate and the NH_3 plasma is generated outside of the reactor. Thus, the bombardment of the sample surface by accelerated ions during the deposition is nearly completely eliminated. For a detailed overview of the deposition principle, please refer to Ref. [90].

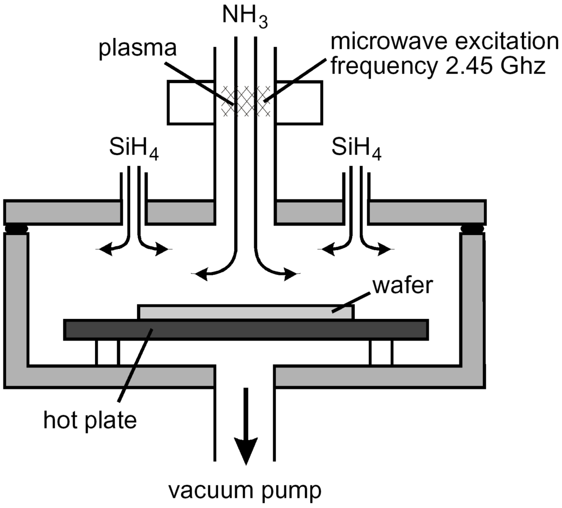

Figure 3.4.: *Schematic representation of the remote PECVD reactor used for the SiN_x deposition. The plasma is generated in the microwave generator outside the deposition chamber. Figure is taken from Ref. [88].*

SiN_x layers with a refractive index of $n = 2.05$ and $n = 2.4$ at a thickness of 70 nm are used in this work. The SiN_x layers are deposited at 400°C. The adjusted deposition parameters for the SiN_x films are given in Table 3.2. J_{0e} are measured before and after a high-temperature firing step at a set temperature of 900°C for $\sim$ 13 s.

TABLE 3.2.
SUBSTRATE TEMPERATURE θ_{SUB}, PLASMA POWER P_{PLASMA}, PRESSURE p_{PLASMA}, SiH_4 GAS FLOW Q_{SiH_4}, NH_3 GAS FLOW Q_{NH_3} AND N_2 GAS FLOW Q_{N_2} USED FOR THE DEPOSITION OF THE SiN_x FILMS.

	θ_{sub} [°C]	P_{plasma} [W]	p_{plasma} [mTorr]	Q_{SiH_4} [sccm]	Q_{NH_3} [sccm]	Q_{N_2} [sccm]
$n = 2.05$	400	150	150	16	200	100
$n = 2.40$	400	150	150	12	200	100

Aluminum oxide (Al_2O_3)

The aluminum oxide is deposited on the Al-p^+ surface by means of atomic layer deposition (ALD). Today ALD is mainly applied in the microelectronics industry where it is used for the deposition of ultra-thin high-quality dielectric layers. It becomes more and more important in photovoltaics as it provides a very effective surface passivation on highly-doped p^+-type silicon [91]. The Al_2O_3 deposition is based on the reaction of two gases, trimethylaluminium [(TMA), $Al(CH_3)_3$] and oxygen O_2. The oxygen is applied either by water steam (thermal ALD) or by an oxygen plasma (plasma-enhanced ALD). In this work, a plasma is used to provide the oxygen radicals for the reaction at the sample surface. The deposition of Al_2O_3 films by plasma-enhanced ALD is ruled by the formation of OH surface groups in combustion-like reactions between the $(CH)_3$ surface groups and the O_2 plasma species. Thus the following 2 half-reactions describe the formation of Al_2O_3 films at a Si surface during deposition [92]:

$$\mathrm{AlOH}^* + \mathrm{Al(CH_3)_3(g)} \rightarrow \mathrm{AlOAl(CH_3)_2}^* + \mathrm{CH_4(g)} \tag{3.1}$$

$$\mathrm{Al(CH_3)}^* + 4\mathrm{O(g)} \rightarrow \mathrm{AlOH}^* + \mathrm{CO_2(g)} + \mathrm{H_2O(g)} \tag{3.2}$$

where the asterisks designate the surface species. Figure 3.5 shows a schematic of the *Oxford Insturments FlexAL*™ remote-plasma ALD reactor which is used in this work.

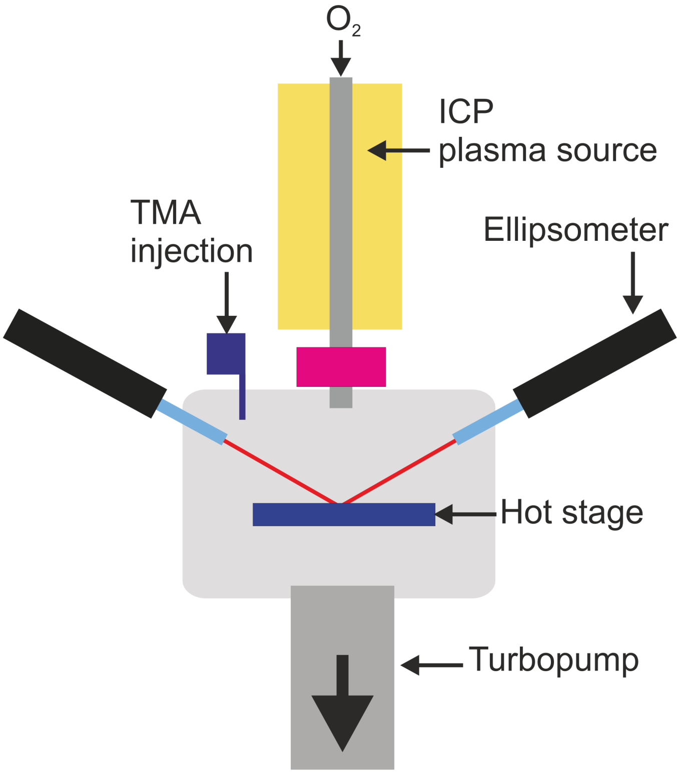

Figure 3.5.: *Schematic of the Oxford Instruments FlexAL™ ALD reactor for the deposition of Al_2O_3.*

Al_2O_3 films are deposited by alternating $Al(CH_3)_3$ dosing and O_2 plasma exposure at a substrate temperature of 200°C. 255 cycles of 4 s resulted in 30nm thick Al_2O_3 films. After deposition, the samples receive a 30 min annealing at 425°C in N_2 atmosphere. The film thickness is controlled by in-situ ellipsometry, as shown in Figure 3.5. The parameters used for the Al_2O_3 deposition are summarized in Table 3.3. Additionally, an Al_2O_3/SiN_x passivation stack is prepared

TABLE 3.3.
SUBSTRATE TEMPERATURE θ_{SUB}, PLASMA POWER P_{PLASMA}, PRESSURE p_{PLASMA}, O_2 GAS FLOW Q_{O_2} USED FOR THE DEPOSITION OF THE AL_2O_3 FILMS.

	θ_{sub} [°C]	P_{plasma} [W]	p_{plasma} [mTorr]	Q_{O_2} [sccm]
Al_2O_3	200	400	15	60

using a 70 nm thick PECVD-SiN$_x$ capping layer with a refractive index of n = 2.1 deposited at 400°C on top of the 30 nm thick Al_2O_3 layer. The J_{0e} values are measured before and after high-temperature firing at a set temperature of 900°C for 13s using the *RTC LT-310* conveyor belt furnace.

Figure 3.6 shows a tilted cross-sectional SEM image of an Al-p^+ region passivated by an Al_2O_3/SiN$_x$ stack where the Al_2O_3 layer appears as bright contrast in-between the Al-p^+ region beneath and the PECVD-SiN$_x$ capping layer on top of it.

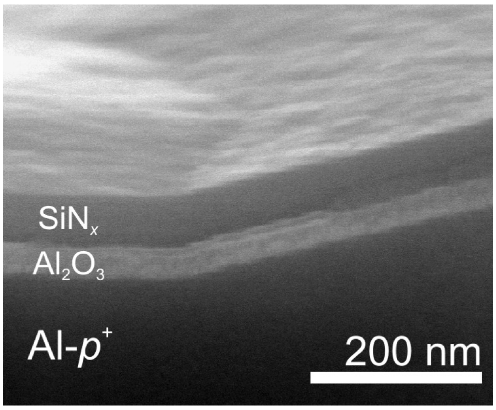

Figure 3.6.: *Tilted cross-sectional SEM image of an Al-p^+ region passivated by an Al_2O_3/SiN$_x$ stack.*

Thermally grown silicon dioxide (SiO_2)

The thermal oxidation of Si is a solid-state chemical reaction which is based on the diffusion of oxygen into the silicon surface. This reaction already takes place at room temperature. However, its reaction rate is extremely low at this temperatures and thus it is not relevant for technical applications. The oxidation of Si to silicon dioxide (SiO_2) can be subdivided into two different processes: (i) dry oxidation and (ii) wet oxidation. Each oxidation process is split up into three steps: (1) The transport of the gas to the surface of the substrate (oxygen gas or water), (2) the diffusion of the gas through the already existing SiO_2 layer, and (3) the oxidation reaction at the SiO_2/Si interface. During the SiO_2 growth the oxygen is incorporated into the silicon, thus the thermal oxidation is not a process where a dielectric layer is deposited onto the surface but the silicon is transformed into SiO_2. As the Si is consumed during the growth procedure, the SiO_2 extends from ∼46% below to ∼54% above the original Si surface (see Figure 3.7).

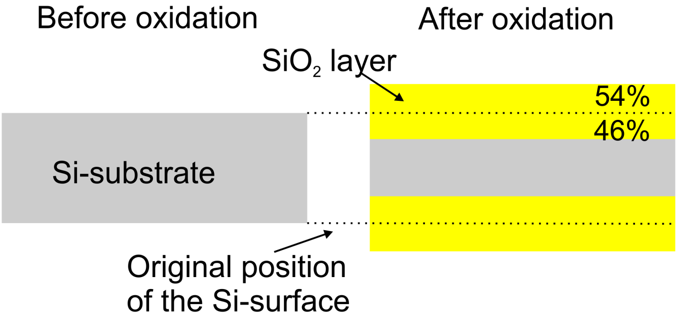

Figure 3.7.: *Schematic of the SiO_2 layer extention due to the Si consumption during thermal oxidation of a Si substrate.*

The dry oxidation of Si is typically performed at temperatures between 800°C and 1200°C in an oxygen atmosphere. The resulting film thickness depends on the applied temperature and on the oxidation time and is described by the following reaction:

$$\mathrm{Si} + \mathrm{O_2(g)} \rightarrow \mathrm{SiO_2}. \tag{3.3}$$

The wet oxidation process uses water as oxidizing agent. During the process a supporting gas such as oxygen or an oxygen-nitrogen mixture is pumped through the so-called *bubbler*. The bubbler is filled with deionized water at a temperature of 90°C. As the gas flows through the water it captures water molecules and transports them into the quartz tube and to the Si surface where they react at temperatures of 800°C-1100°C according to the following reaction:

$$\mathrm{SiO} + 2\mathrm{H_2O(g)} \rightarrow \mathrm{SiO_2} + 2\mathrm{H_2(g)}. \tag{3.4}$$

Figure 3.8 shows a schematic of a quartz tube as it is used in this work for the dry and the wet oxidation. The growth of an SiO_2 layer at a given temperature and time on a Si substrate is described by the Deal-Grove-model [93].Thermal oxidation is the state-of-the-art process for the surface passivation of crystalline silicon. It is used in microelectronics and in the laboratory-scale fabrication of high-efficiency silicon solar cells. It requires high process temperatures, resulting in a high energy consumption, and in the risk of impurity diffusion into the crystalline silicon bulk.

Nevertheless, thermal oxidation has proven to be an excellently passivating dielectric on lowly doped silicon surfaces as well as on highly n^+ phosphorus- and p^+ boron-doped samples. However, degradation of oxide-passivated p^+ emitters after long term storage has been reported. Common degradation mechanisms reported in solar literature are humidity, thermal treatment, and atomic hydrogen [94–97]. It was also found that boron-diffused oxide-passivated silicon

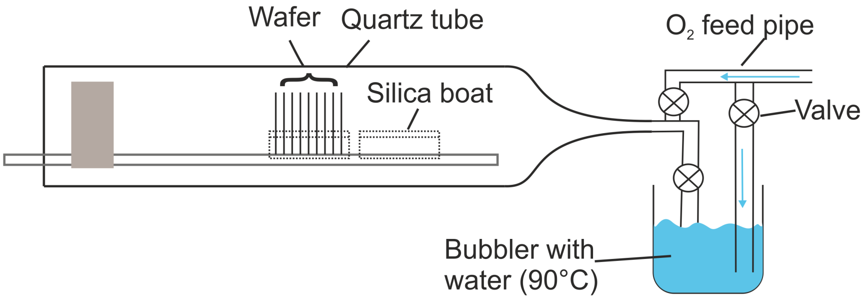

Figure 3.8.: *Schematic representation of a quartz tube as it is used for thermal dry and wet oxidations.*

severely degrades at room temperature, where Thomson et. al. reported a 45 fold increase in saturation current density after storage for 120 days [98].

In this work, wet thermal oxides grown at temperatures of 850°C, 900°C and 1050°C as well as dry oxides grown at 1050°C are applied.

3.3. Results

3.3.1. ECV measurements

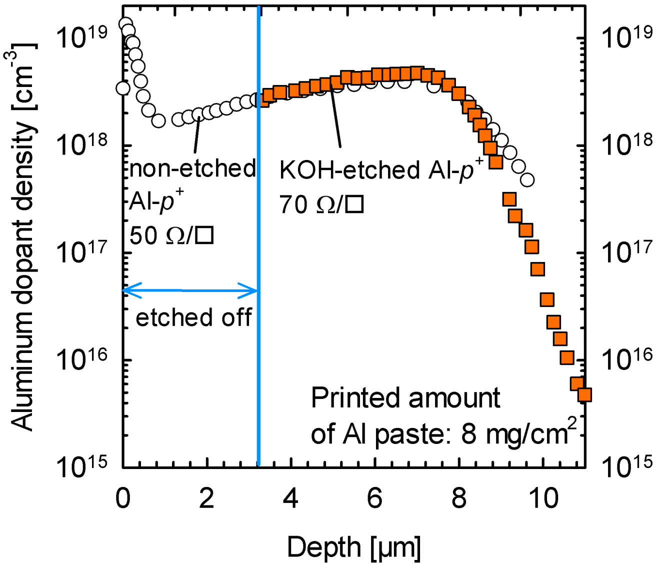

Figure 3.9.: *ECV doping profiles of a screen-printed Al-p^+ emitter before (open circles) and after (orange squares) etching in KOH. During the etching ∼3 µm of the silicon is removed.*

Figure 3.9 shows the ECV-measured doping profile of an Al-p^+ region used for the passivation experiments in this work. As analyzed in Section 2.1, the doping profile of the Al-p^+ region shows a apparent peak close to the surface that originates from residual aluminum-rich structures on the surface which are not effectively removed during the HCl etching. This apparent peak can be removed in a KOH solution at 70°C. In our experiments, 3 μm of the (8 $\pm$ 1) μm thick Al-p^+ region are etched off, which is demonstrated in Fig. 3.9 by ECV measurements taken before and after KOH etching. The emitter thickness after KOH etching is obtained from SEM micrographs at different sample positions to be (5 $\pm$ 1) μm, indicating that the Al-p^+ emitter is completely closed after etching. The sheet resistance is determined from four-point-probe measurements to be 50 $\Omega/\Box$ for the 8 μm deep emitter and 70 $\Omega/\Box$ for the 5 μm deep Al-p^+ emitter.

3.3.2. a-Si:H passivation

The emitter saturation current density J_{0e} is extracted from the measured injection-dependent effective lifetime data by plotting the reciprocal effective lifetime $1/\tau_{\text{eff}}$ versus the excess carrier concentration Δn. Figure 3.10 shows the measured inverse effective lifetime $1/\tau_{\text{eff}}$ as a function of the injection density Δn for the same sample in three different states. The steepest slope is obtained directly after the Al paste (paste A) and the Al–Si eutectic have been etched off and 3 μm of the p^+ region have been removed. Using a linear fit of Eq. 2.2 to the measured data results

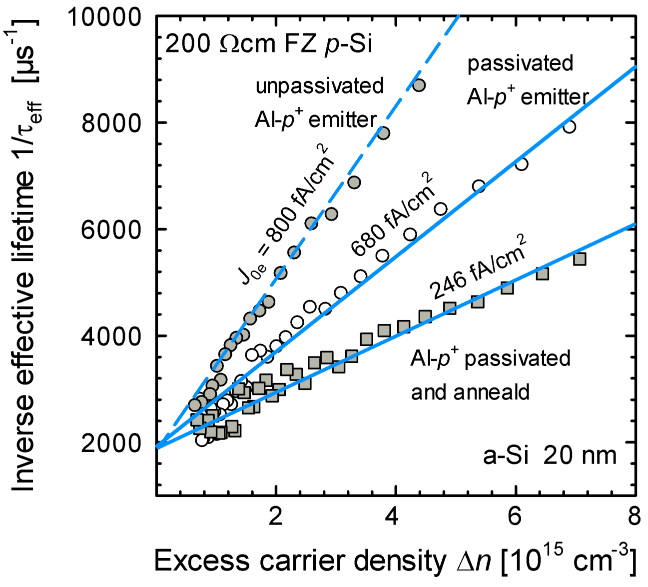

Figure 3.10.: *Measured inverse effective lifetime $1/\tau_{eff}$ as a function of the excess carrier density Δn of a 200 Ωcm FZ p-Si wafer. The Al-p^+ region covers only one side of the wafer; the other surface is well passivated by SiN_x.*

in an emitter saturation current density of J_{0e} = (800 ± 200) fA/cm^2.

Note that before KOH etching a J_{0e} of (680 ± 170) fA/cm^2 is measured. This lower J_{0e} value results from the deeper Al-p^+ emitter which has a lower sheet resistance and, thus, a higher degree of field effect passivation, effectively reducing the surface recombination rate. After the deposition of 20 nm of a-Si on the KOH-etched emitter surface a significant reduction in the slope can be observed, resulting in a J_{0e} value of (490 ± 120) fA/cm^2. Finally, the lowest slope is measured for the sample after an additional 300°C annealing for 10 min, resulting in a J_{0e} value of only (246 ± 60) fA/cm^2. The experimental results in Figure 3.10 prove that screen-printed Al-p^+ emitters can be very effectively passivated with low-temperature deposited amorphous silicon films.

From the measured J_{0e} values the implied open-circuit voltage $V_{\mathrm{oc.impl}}$ is calculated using the expression

$$V_{\mathrm{oc.impl}} = \frac{kT}{q} \ln\left(\frac{J_{\mathrm{SC}}}{J_{0e}} + 1\right), \tag{3.5}$$

where kT/q = 25.86 mV at 300 K and a realistic short-circuit current density J_{sc} of 38.6 mA/cm^2 is assumed. The latter J_{sc} value has recently been realized on n-type Si solar cells with a screen-printed Al-p^+ emitter [56]. Using the J_{0e} of (680 ± 170) fA/cm^2, a $V_{\mathrm{oc.impl}}$ of (640 ± 6) mV is calculated for the non-passivated Al-p^+ surface. This is quite high compared to experimentally realized n-type Si solar cells with Al-p^+ emitter showing maximum V_{oc} values of 627 mV [56]. This may be due to the Al paste and the Al–Si eutectic that remained on the p^+ emitter surface in these cells, increasing the surface recombination velocity on the Al-p^+ surface, whereas the emitter surface in this work is free from metallic residuals which may result in lower J_{0e} values. However, the most probable reason for the lower open-circuit voltage is a high surface recombination at the front of the solar cell due to a low passivation level of the highly-doped phosphorus-diffused front surface field (FSF) and due to recombination losses at the metalized areas.

Figure 3.11 shows the effect of low-temperature annealing on the emitter saturation current density of a-Si passivated screen-printed Al-p^+ emitters. The annealing is interrupted minute by minute for the lifetime measurements. Both pastes in this study behave similarly. Before annealing we measure J_{0e} values of (576 ± 144) fA/cm^2 for paste A and of (490 ± 120) fA/cm^2 for paste B. After only 1 min of annealing at 300°C a pronounced decrease in J_{0e} to (371 ± 92) fA/cm^2 for paste A and (328 ± 82) fA/cm^2 for paste B is observed. Annealing up to 10 min gives a measured J_{0e} of only (258 ± 64) fA/cm^2 for paste A and (246 ± 60) fA/cm^2 for paste B. These are the lowest J_{0e} values achieved so far for screen-printed Al-p^+ emitters. Note that a similar annealing effect as shown in Figure 3.11 has recently been reported for a-Si-passivated boron-doped p^+ emitters [99, 100].

The minority-carrier surface recombination velocity S_{n0} is extracted using PC1D simulations. In these simulations, it is assumed that the bulk of the Al-p^+ region is Auger-limited. An S_{n0}

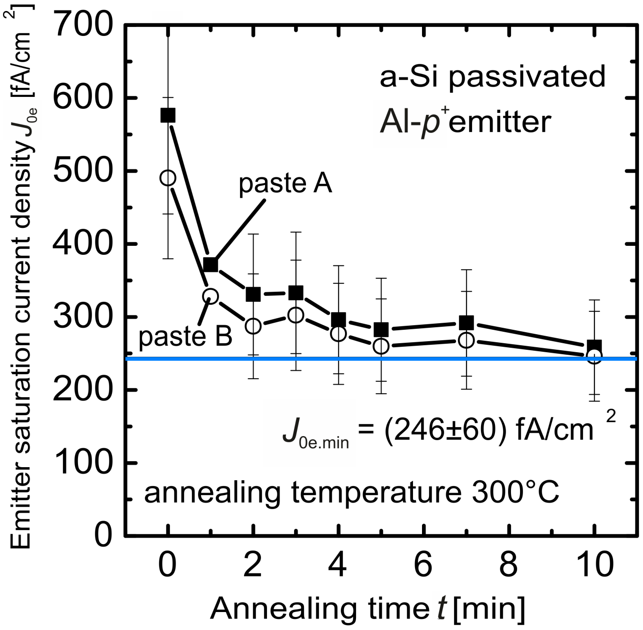

Figure 3.11.: *Impact of annealing time at 300°C on the emitter saturation current density J_{0e} of an a-Si passivated Al-p^+ emitter. An annealing period of 10 min at 300 °C gives a minimum saturation current density of $J_{0e.min}$ = (246 ± 60) fA/cm^2.*

value >5 × 10^4 cm/s is determined for the unpassivated surface. For the a-Si passivated and annealed Al-p^+ emitter with the measured J_{0e} of (246 ± 60 fA/cm^2) a surface recombination velocity S_{n0} between 7000 and 13000 cm/s is extracted. A minimum S_{n0} value of 800 cm/s has recently been published for a-Si-passivated boron-doped p^+ emitters at a comparable sheet resistance [74]. However, regarding the much lower complexity of forming a screen-printed Al-p^+ emitter, the S_{n0} values achieved in this study are still remarkably low. The lowest measured J_{0e} values correspond to implied open circuit voltages of $V_{oc.impl}$ = (667 ± 6) mV for paste A and $V_{oc.impl}$ = (665 ± 6) mV for paste B, clearly demonstrating the high-efficiency potential of a-Si passivated screen-printed Al-p^+ emitters.

Out experimental results show for the first time that screen-printed Al-p^+ emitters can be very effectively passivated by low-temperature PECVD-deposited amorphous silicon films. The observed excellent passivation properties are attributed to the high degree of interface passivation with atomic hydrogen. From in-situ spectroscopic ellipsometry and infrared spectroscopy it is known that a 30 Å thick a-Si layer with very high hydrogen content (~17 at.%) forms at the c-Si surface during deposition [101]. A part of this hydrogen effectively saturates dangling bonds at the a-Si/c-Si interface, reducing interface recombination. During annealing some of the hydrogen is released from the a-Si layer and diffuses towards the interface, where it passivates additional dangling bonds.

3.3.3. SiN$_x$ passivation

Figure 3.12 (a) shows the measured inverse effective lifetime $1/\tau_{\mathrm{eff}}$ as a function of the injection density Δn for a SiN$_x$ passivation layer with a refractive index of $n = 2.05$. After the Al-p^+ emitter surface is passivated no significant passivation effect can be observed and $J_{0\mathrm{e}}$ of (616 ± 150) fA/cm^2 is measured. Firing at 900°C improves the passivation quality of the SiN$_x$ layer resulting in a $J_{0\mathrm{e}}$ of (307 ± 76) fA/cm^2. A similar behavior is observed on samples passivated with an SiN$_x$ layer of $n = 2.4$, where a saturation current density of (764 ± 190) fA/cm^2 is measured for the unpassivated emitter surface and a nearly unchanged $J_{0\mathrm{e}}$ of (707 ± 177) fA/cm^2 for the passivated emitter surface [see Figure 3.12 (b)]. Firing at 900°C improves the passivation quality down to a measured $J_{0\mathrm{e}}$ of (339 ± 85) fA/cm^2. It is known that as deposited PECVD-SiN$_x$ gives by far the worst passivation quality on boron-doped p^+ emitters due to its high built-in positive charge density Q_{f} of 2×10^{12} charges/cm^2 [102]. An improvement of the passivation quality after firing is observed in this work, which is also consistent with literature data for boron-doped p^+ emitters [103]. Two possible mechanisms are discussed in the literature to be responsible for the improved passivation of PECVD-SiN$_x$ layers after post-temperature treatment: (1) hydrogenation of dangling bonds at the interface and (2) a decrease in the fixed positive charge density in the SiN$_x$ film during annealing [88, 104]. We assume that the hydrogenation of the dangling bonds is the major passivation mechanism on aluminum-doped p^+ emitters.

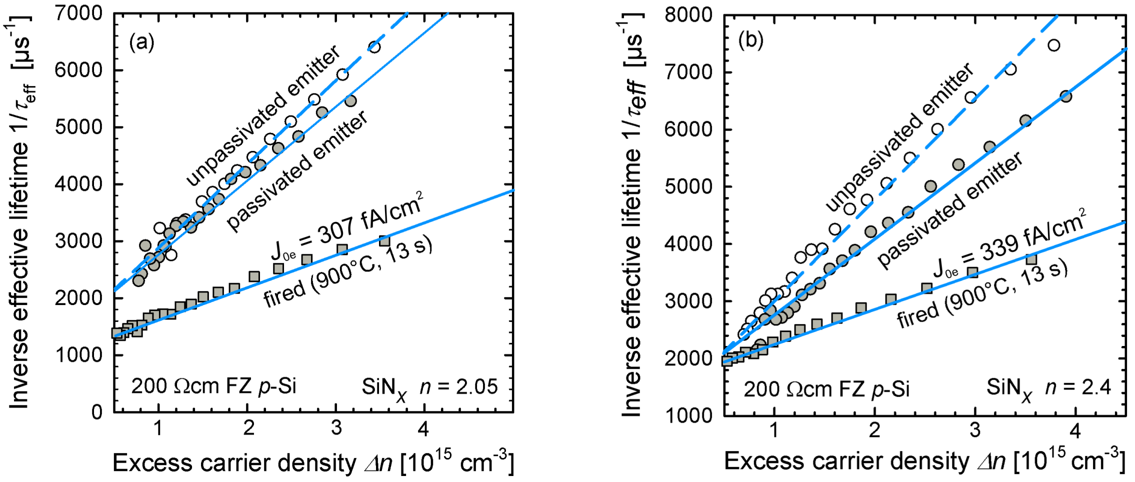

Figure 3.12.: *Measured inverse effective lifetime $1/\tau_{eff}$ as a function of the excess carrier density Δn of a 200 Ωcm FZ p-Si wafer. The Al-p^+ region covers only one side of the wafer and is passivated by SiN$_x$, (a) with a refractive index of n = 2.05 and (b) with a refractive index of n = 2.40. The other surface is well passivated by SiN$_x$.*

3.3.4. Al_2O_3 and Al_2O_3/SiN_x passivation

Figure 3.13 (a) shows the inverse effective lifetime $1/\tau_{\mathrm{eff}}$ as a function of the injection density Δn measured for an Al_2O_3-passivated sample. A 30 nm thick single layer of amorphous Al_2O_3 deposited on top of an Al-p^+ emitter surface reduces the saturation current density $J_{0\mathrm{e}}$ from (843 ± 210) fA/cm^2 down to only (206 ± 51) fA/cm^2. Firing at 900°C has almost no effect on the passivation quality of the deposited Al_2O_3 layer. The $J_{0\mathrm{e}}$ increases slightly to (265 ± 66) fA/cm^2, which is still at a very low $J_{0\mathrm{e}}$ level. Figure 3.13 (b) shows the $1/\tau_{\mathrm{eff}}$ vs. Δn plot measured for a sample passivated by Al_2O_3 plus a 70 nm thick SiN_x capping layer with a refractive index of n = 2.1, which reduces the $J_{0\mathrm{e}}$ to a record-low value of only (160 ± 40) fA/cm^2, proving the excellent passivation quality of Al_2O_3/SiN_x stacks. Moreover, the passivation stack provides a still remarkably low $J_{0\mathrm{e}}$ of (228 ± 57) fA/cm^2 after firing at a peak temperature of 900°C, which enables an industrial application of the Al_2O_3/SiN_x stack. Literature data shows that Al_2O_3 layers have a negative fixed charge density of up to $Q_{\mathrm{f}} = -1.3\times10^{13}$ elementary charges/cm^2 [102]. The fixed negative charge density within the Al_2O_3 layer induces an accumulation layer at the p-type silicon surface. As a consequence, the Al_2O_3 provides a very effective field-effect passivation.

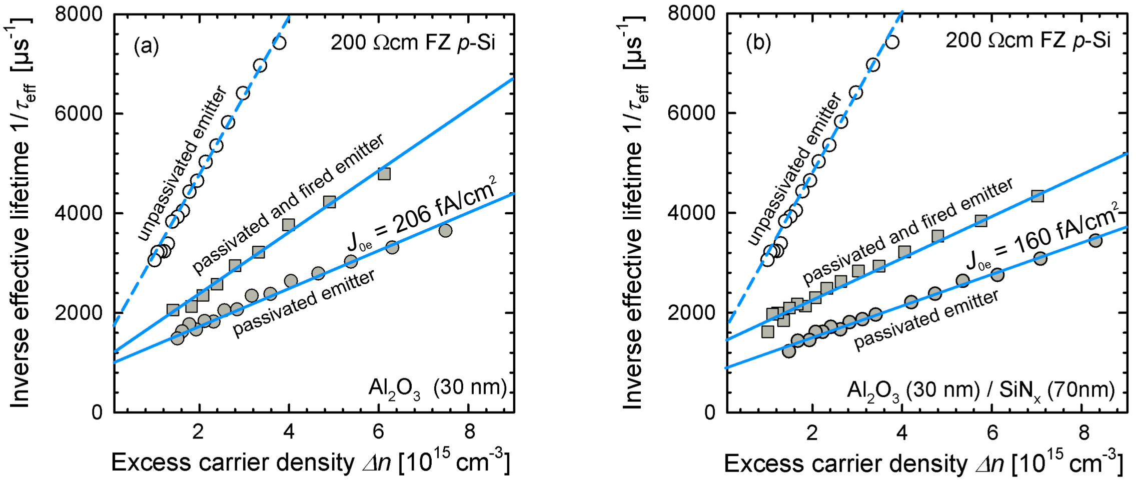

Figure 3.13.: *(a) Measured inverse effective lifetime* $1/\tau_{\mathit{eff}}$ *as a function of the excess carrier density* Δn *of a 200 Ωcm FZ p-Si wafer. The Al-*p^+ *region covers only one side of the wafer and is passivated by a 30 nm thick ALD-*Al_2O_3 *layer, the other surface is well passivated by* SiN_x*. (b) Measured inverse effective lifetime* $1/\tau_{\mathit{eff}}$ *as a function of the excess carrier density* Δn *of a 200 Ωcm FZ p-Si wafer. The Al-*p^+ *region covers only one side of the wafer and is passivated by an* Al_2O_3/SiN_x *stack, the other surface is well passivated by* SiN_x *only.*

3.3.5. SiO_2 passivation

As shown in Section 2.3 oxidation temperatures $\geq$900°C result in a reduced carrier lifetime in the Al-p^+ bulk and thus in J_{0e} values larger than J_{0e} values measured on unpassivated Al-p^+ regions. A probable explanation for this depassivation effect is the formation of recombination-active Al-O complexes at the elevated oxidation temperatures, while the low-temperature passivation methods applied to the Al-p^+ surface show no lifetime degradation. As a consequence, we develop a passivation method for the Al-p^+ emitter surface consisting of a low-temperature thermal oxidation at 850°C. During oxidation a 20 nm thick SiO_2 layer is formed which is covered by a 70 nm thick PECVD-SiN_x layer. Figure 3.14 shows the measured inverse effective lifetime $1/\tau_{eff}$ as a function of the injection density Δn of a sample featuring such an SiO_2/SiN_x stck. For comparison the J_{0e} measured for an unpassivated sample as well as for a sample oxidized at 1050°C is included. The SiO_2/SiN_x stack shows a remarkably low J_{0e} of 200 fA/cm^2 which is as good as the Al_2O_3. After firing the SiO_2/SiN_x stack still shows a very good J_{0e} of 280 fA/cm^2 proving its stability under firing conditions.

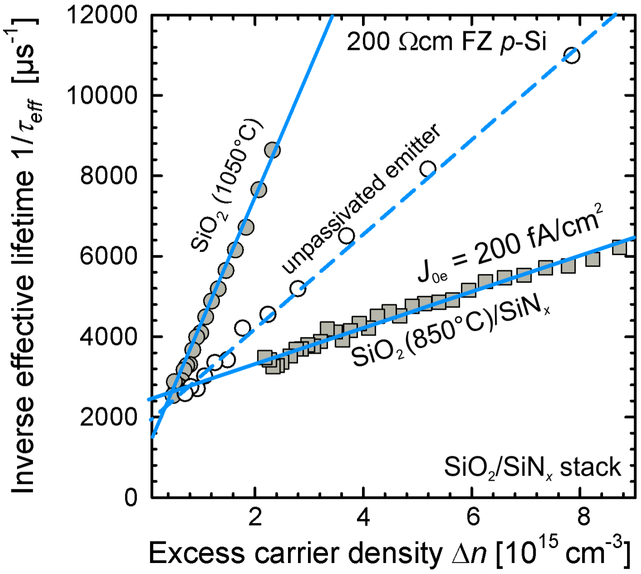

Figure 3.14.: *Measured inverse effective lifetime $1/\tau_{eff}$ as a function of the excess carrier density Δn for an Al-p^+ emitter oxidized at 1050°C and for an Al-p^+ emitter with our optimized passivation scheme featuring a thermal oxidation of the emitter surface at 850°C and a SiN_x coating (70nm, n = 2.4) on top of the SiO_2. A clear depassivation effect can be observed for the thermal oxidation at 1050°C, whereas the low-temperature oxidation (850°C) provides a J_{0e} of 200 fA/cm^2.*

3.4. Comparison with literature data

In this Section we compare the saturation current densities measured on unpassivated and passivated Al-p^+ regions in this work with data published in the literature. Bitnar [105] has determined an average J_{0e} of 650 fA/cm^2 using a combined evaluation of V_{oc}-J_{sc} transients and *IQE* measurements on Cz-Si solar cells. He measured only slightly higher values of 720 fA/cm^2 on mc-Si. Higher J_{0e} values were reported by Bowden et al. [106] who used QSSPC measurements and measured J_{0e} values between 980 and 1260 fA/cm^2 using the slope method. These values are slightly higher than the values measured on unpassivated samples in this work. This is probably due to measurement errors.

Saturation current densities of 380 fA/cm^2 were reported by Narasimha et al. [107], who analyzed the spectrally resolved *IQE* of a FZ-Si solar cell with a 6 μm thick BSF obtained from a fritted paste.

J_{0e} of 330-430 fA/cm^2 were reported by Loelgen [62], who used transient PCD measurements on symmetric test structures.

Tool et al. [108] on the other hand have reported much higher J_{0e} values. They published a J_{0e} of 3.3 pA/cm^2 by fitting the *IQE* of mc-Si solar cells with varying thickness using PC1D and 2.1 pA/cm^2 using the QSSPC-slope method. They also reported a value of 0.4 μm for the diffusion length in the BSF, which is much lower than the values presented in this work.

More recently, other groups presented J_{0e} values from passivated Al-p^+ regions. Rauer et al. [109] determined a J_{0e} of 128 fA/cm^2 for a-Si-passivated and of 89 fA/cm^2 for Al_2O_3-passivated Al-p^+ regions. These values are lower than the data presented in this work for passivated Al-p^+ regions. This is mainly due to the fact that the thickness of the Al-p^+ regions was 3 μm, whereas in this work it was 5 - 8 μm. Thicker Al-p^+ regions suffer from higher overall bulk recombination and thus show increased J_{0e} values.

The J_{0e} values presented by other authors seem at least partly not to be consistent with the data reported in this work. However, it has to be mentioned that the J_{0e} of an Al-p^+ region crucially depends on the conditions under which the Al-p^+ region has been processed and characterized. The influencing parameters are:

- the composition of the paste (fritted paste or not-fritted, presence of contaminants)
- the firing conditions (firing temperature and formation of defects, see Section 2.3)
- the thickness of the Al-p^+ region (thin Al-p^+ regions show lower J_{0e} values due to the reduced overall recombination)
- the homogeneity of the Al-p^+ region (thickness variations of 1-3 μm are possible)
- the sample structure (solar cell or symmetric and asymmetric test device, mc-Si, FZ-Si, Cz-Si)

- the measurement method (*IQE*, lifetime measurements on test structures, symmetric vs. asymmetric test structures)

All these factors have a pronounced impact on the recombination properties of the Al-p^+ region or on the measurement result and thus the J_{0e} values presented in this Section are valid for the particular conditions applied in our experiments.

3.5. Chapter summary

In this Chapter the passivation quality of several passivation methods for the screen-printed Al-p^+ emitter were investigated by means of saturation current density measurements. Figure 3.15 shows a summary of saturation current densities measured on samples with several passivation layers and passivation stacks. We have shown for the first time that the passivation of Al-p^+ emit-

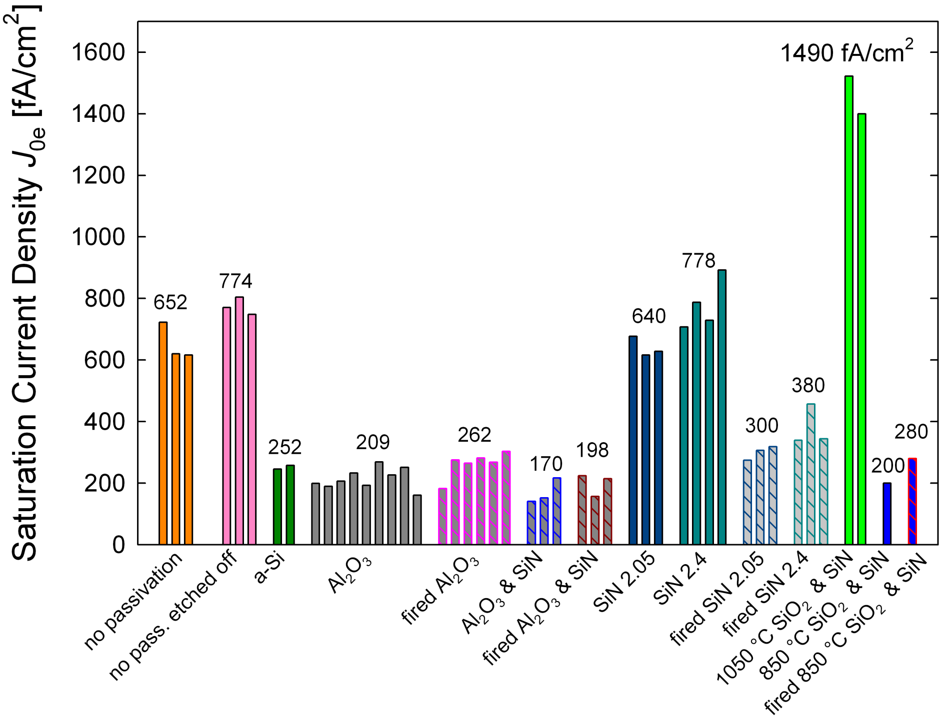

Figure 3.15.: *Summarized saturation current densities J_{0e} of all applied passivation schemes to our Al-p^+ emitters including a-Si, SiN_x, Al_2O_3, Al_2O_3/SiN_x stacks, SiO_2, and SiO_2/SiN_x stacks as well as the firing stability of these passivation methods. Each bar corresponds to a single sample. The J_{0e} values given above the bars represent average J_{0e} values of identically processed samples*

ters can be realized with a-Si, SiN_x, Al_2O_3, Al_2O_3/SiN_x stacks, and thermally grown SiO_2/SiN_x stacks.

Emitter saturation current densities of only 206 fA/cm^2 for Al_2O_3-passivated Al-p^+ emitters and an extremely low J_{0e} of 160 fA/cm^2 for the Al_2O_3/SiN_x stack have been achieved. Moreover, both passivation schemes showed very good stability under firing conditions with $J_{0e} = 265$ fA/cm^2 for Al_2O_3-passivated emitters and 228 fA/cm^2 for Al_2O_3/SiN_x-passivated emitters, respectively, enabling the application to high-efficiency industrial solar cells. PECVD-SiN_x shows also a good passivation quality after firing with a J_{0e} of 339 fA/cm^2 for the SiN_x layer with a refractive index n of 2.4 and a J_{0e} of 309 fA/cm^2 for the SiN_x layer with a refractive index n of 2.05, enabling the industrial application as well. A pronounced depassivation effect was observed for samples passivated by means of thermal SiO_2 at an oxidation temperature of 1050°C due to the formation of recombination active Al-O complexes. At oxidation temperatures of 850°C no depassivation effect was observed. The combination of a low-temperature (850°C) thermal SiO_2 with a PECVD-SiN_x capping layer shows an excellent passivation quality, where a saturation current density of $J_{0e} = 200$ fA/cm^2 was measured, which is as low as the J_{0e} of the Al_2O_3-passivated emitter and which is also stable under firing at 900°C. Our experimental results demonstrate that the industrially feasible and technologically simple screen-printed Al-p^+ emitter is well suitable for future generations of industrial high-efficiency silicon solar cells.

4. Application to solar cells

In Section 1.1 it has been shown that n-type Cz-silicon has a much higher carrier lifetime as well as a much better lifetime stability under illumination than boron-doped p-type Cz-silicon [6]. The combination of these benefits with a cost-saving and simple industrially feasible manufacturing process for the emitter, such as screen printing, makes n-type Cz-grown crystalline silicon a very promising material for future industrial solar cells. In Chapter 2 and 3 it was shown that the lifetime in screen-printed Al-p^+ regions is in the order of 130 ns and hence allows to achieve high open-circuit voltages up to 670 mV and efficiencies up to 21%. It was also demonstrated in this work for the first time that the highly aluminum-doped p^+ surface fabricated by means of screen printing can be effectively passivated by thin layers of amorphous silicon, aluminum oxide and also thermally grown silicon dioxide. This Chapter deals with the application of the screen-printed Al-p^+ emitter (i) to solar cells with evaporated contacts (Section 4.1), (ii) to back-junction back-contact solar cells (Section 4.2), and (iii) industrial-type solar cells with screen-printed contacts (Section 4.3).

4.1. *n*-type solar cells with Al-p^+ rear emitter

The purpose of this Section is to demonstrate the applicability of the surface-passivated and screen-printed Al-p^+ emitter to an n^+np^+ solar cell with evaporated contacts. In Section 4.1.1, the fabricated solar cell structures are introduced generally. Then, in Section 4.1.2, the processing sequence is explained in detail. Finally, in Section 4.1.3 the current-voltage characteristics, electroluminescence images, and quantum efficiency measurements of the fabricated cells are presented. We name the n^+np^+ solar cells with passivated Al-p^+ rear emitter *ALU*$^+$ *solar cells.*

4.1.1. Solar cell structures

Figure 4.1 shows two possible realizations of an ALU$^+$ solar cell featuring an n-type Si base, a surface-passivated screen-printed Al-p^+ rear emitter and evaporated front and rear contacts. The surface passivation is applied to the rear side of the cell with (i) a locally evaporated contact grid onto the a-Si passivation layer [Fig. 4.1 (a)] and (ii) a full-area metallization onto an a-Si/SiO$_x$ stack with local point contact openings [Fig. 4.1 (b)]. The second type of cell shown in Fig. 4.1 (b) was also realized with an Al_2O_3 passivation layer as well as an Al_2O_3/SiN$_x$ stack.

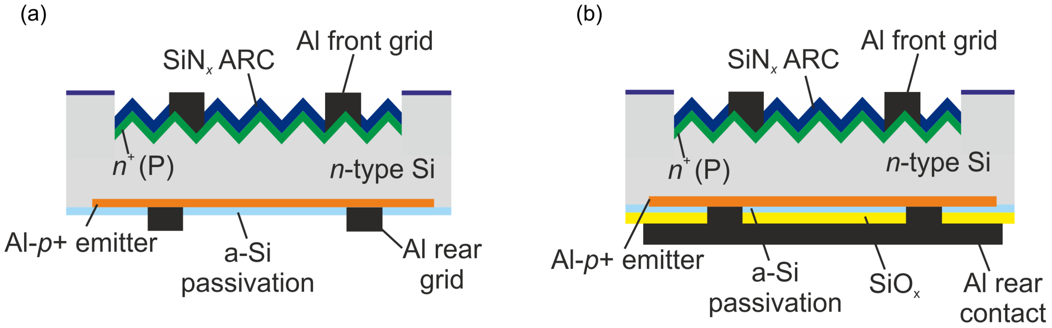

Figure 4.1.: *Two realizations of an n-type Si solar cell featuring a screen-printed Al-*p^+ *emitter passivated with a thin a-Si layer. (a) Evaporated Al-grid on the a-Si passivated rear emitter, (b) full-area metalized a-Si passivated emitter with local point contacts realised by laser ablation and subsequent Al evaporation.*

4.1.2. Processing sequences

a-Si-passivated solar cells

Figure 4.3 shows the processing sequence of the ALU$^+$ solar cells. As base material we use (100)-oriented phosphorus-doped Czochralski-grown silicon wafers with a thickness of $\sim$190 μm and a resistivity of $\sim$3 Ωcm. First, we grow a 220 nm thick thermal oxide on both wafer surfaces (120 min wet oxidation at 900°C plus 30 min dry oxidation at 900°C). Second, 2×2 cm^2 diffusion windows are opened on the front by means of photolithography and subsequently random pyramids are formed within the opened windows using a 5% solution of KOH plus $\sim$100ml of isopropanol at 90°C for 60 min. Afterwards, phosphorus is diffused into the diffusion windows at the front, resulting in an n^+ region, which is subsequently oxidized at 850°C (120 min wet oxidation plus 30 min dry oxidation).

Doping profiles of the applied front surface field (FSF) diffusions as measured by the ECV technique are depicted in Figure 4.2. Two different FSF diffusions have been applied to the cells, resulting in sheet resistance of 50 $\Omega/\square$ and 112 $\Omega/\square$, respectively. For the 50 $\Omega/\square$ n^+ diffusion $POCl_3$ gas has been applied to the wafers for 20 min at 880°C followed by a drive-in phase in nitrogen for 20 min at 880°C. For the 112 $\Omega/\square$ n^+ diffusion $POCl_3$ gas has been applied to the wafers for 20 min at 852°C followed by a drive-in phase in nitrogen of 20 min at 852°C. After the wet oxidation at 850°C sheet resistances of 125 $\Omega/\square$ and 238 $\Omega/\square$ are obtained. During this oxidation the phosphorus concentration peak (kink) is mostly oxidized and simultaneously, according to the applied temperature of 850°C, the phosphorus in the Si (tail) diffuses into the Si (drive-in). This process results in an n^+ FSF with easy-to-passivate low surface doping concentrations of 6×10^{19} and 2×10^{19} cm^{-3}, respectively [87, 110–112]. A *Centrotherm CENTRONIC Dotiersystem 2000HT 180-4* quartz tube furnace has been used for the thermal oxidation and diffusion processes.

Subsequently, the remaining oxide is removed from the wafer surface by means of an HF dip

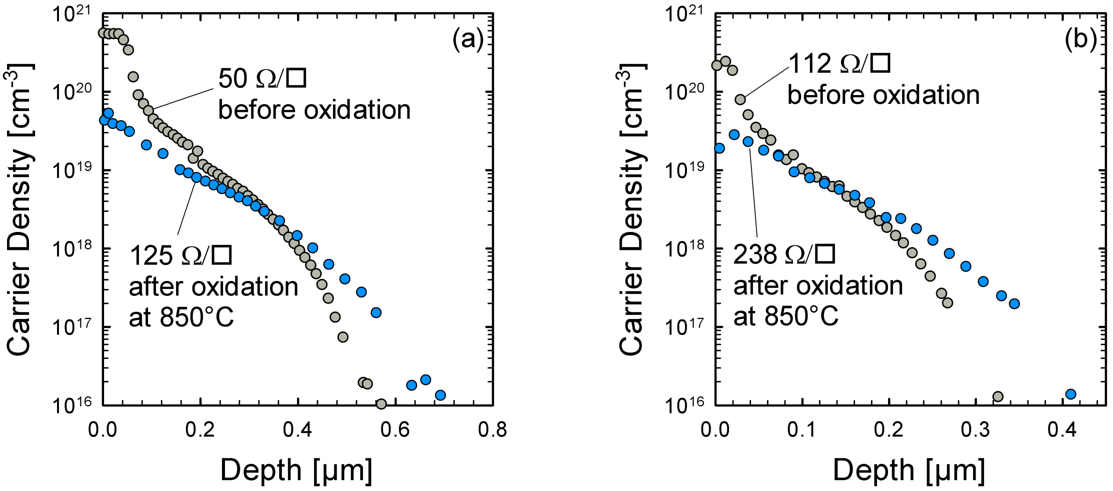

Figure 4.2.: *Doping profiles of the front surface field (FSF) phosphorus diffusion before and after a wet oxidation step at 850°C, measured by ECV profiling. (a) 50* $\Omega/\square$ *P-diffusion with an as-diffused surface dopant concentration of* 5×10^{20} *and of* 6×10^{19} cm^{-3} *after the oxidation step. (b) 112* $\Omega/\square$ *P-diffusion with an as-diffused surface dopant concentration of* 2×10^{20} *and of* 2×10^{19} cm^{-3} *after the oxidation step.*

(5% HF, 10 min) and the textured front side is covered by a 200 nm SiN$_x$ layer deposited by remote-PECVD at 400°C with a refractive index of n = 2.05 using an *Oxford Plasma Technology Plasmalab 80+* PECVD reactor to protect the front surface from etching during the subsequent back-etching procedure of the rear emitter.

After screen-printing and firing of the Al-p^+ rear emitter, the residual Al paste and the Al-Si eutectic are removed in a boiling 37% solution of HCl and the Al-p^+ emitter is etched back by 2-3 μm in a 50% KOH solution at 70°C. The protective SiN$_x$ coating is removed from the front side and the wafer received an RCA cleaning before the emitter surface is passivated by a 20 nm thick a-Si layer deposited by means of PECVD at 225°C using an *Oxford Plasma Technology Plasmalab µP* PECVD reactor. For the cell type shown in Fig. 4.1 (a) an Al rear contact grid is evaporated through a shadow mask with metallization fractions of ∼4% (finger spacing 2 mm) and of ∼6% (finger spacing 1 mm), respectively. For the cell type shown in Fig. 4.1 (b) a 200 nm thick PECVD-SiO$_x$ layer was deposited on top of the a-Si layer (*Oxford Plasma Technology Plasmalab µP*). After local contact opening using photolithograpy, a full-area Al layer is evaporated onto the rear side. The metallisation fraction of the rear emitter contact is 4%. For both cell types, an Al front contact grid is evaporated through a shadow mask with a metallization fraction of ∼3% and a finger distance of 1 mm. A Blazers BAK 500 vacuum coating system has been used for the contact evaporation. As last process step a SiN$_x$ layer is deposited onto the front of the solar cells. The SiN$_x$ consists of two layers: (i) a 15 nm thick well passivating SiN$_x$ layer with a refractive index of n = 2.4 at 692 nm and (ii) a 60 nm thick SiN$_x$

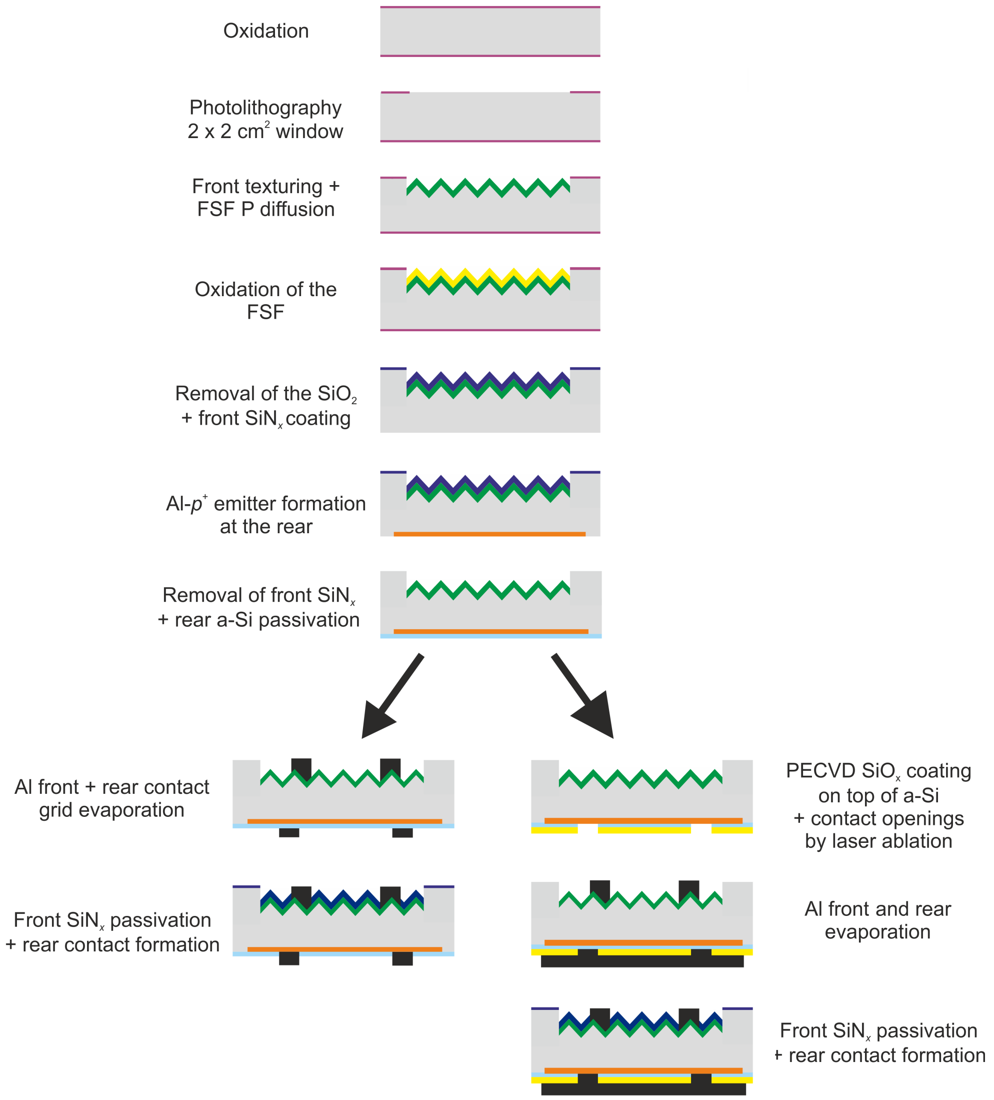

Figure 4.3.: *Schematic of the processing sequence of the two types of ALU$^+$ solar cells with evaporated contacts fabricated in this work.*

antireflection coating with a refractive index of $n = 2.05$. During the SiN_x deposition performed at 400°C, the a-Si underneath the Al contacts dissolves and the Al formes an ohmic contact to the Al-p^+ emitter [113].

Al_2O_3/SiN_x-passivated solar cells

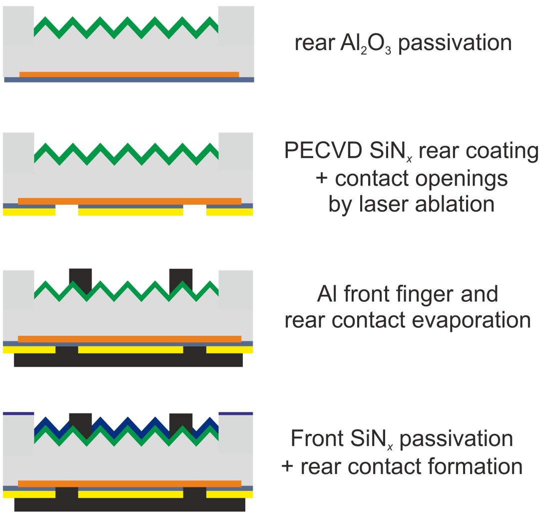

Figure 4.4.: *Schematic of the processing steps different from that shown in Fig. 4.3 for the fabrication of the solar cells with an Al-p^+ rear emitter passivated with an Al_2O_3/SiN_x stack.*

Additionally, in accordance with the results presented in Section 3.3.4, where the Al_2O_3/SiN_x stack has proven to provide the lowest saturation current density values on screen-printed Al-p^+ emitter surfaces, a second set of solar cells featuring an Al_2O_3/SiN_x passivation stack at the rear emitter surface has been prepared. The solar cell structure is similar to the solar cell shown in Fig. 4.1 (b). Figure 4.4 shows the processing steps which are different compared to the processing sequence shown in Fig. 4.3. The main difference is the ALD-Al_2O_3 passivation of the Al-p^+ rear emitter instead of PECVD-a-Si. We deposit a 20 nm thick ALD-Al_2O_3 layer at 225°C on the Al-p^+ emitter surface using an *Oxford Instruments FlexAL*™ ALD reactor. Secondly, a 100 nm PECVD-SiN_x capping layer with a refractive index of $n = 2.05$ instead of a PECVD-SiO_x capping layer is implemented. The SiN_x deposition has been performed at 400°C which simultaneously acts as activation of the Al_2O_3 layer (see Chapter 3).

4.1.3. Solar cell results

a-Si-passivated rear emitter

The one-sun performance of the best n-type solar cells featuring the a-Si passivated Al-p^+ emitter is shown in Table 4.1. Cells P01 and P25 have evaporated Al-grid on the rear and front and an n^+ FSF of 125 $\Omega/\square$ and 238 $\Omega/\square$, respectively [Figure 4.1 (a)]. Cell P15 corresponds to the full-area rear Al metalization and point-contact openings at the rear and an n^+ FSF of 238 $\Omega/\square$ [Figure 4.1 (b)].

TABLE 4.1.
SOLAR CELL PARAMETERS MEASURED UNDER STANDARD TESTING CONDITIONS (AM1.5G, 100 MW/CM^2, 25°C). THE APERTURE CELL AREA IS 4 CM^2.

Cell type	V_{oc} [mV]	J_{sc} [mA/cm^2]	*FF* [%]	η [%]
P01 (a-Si + evaporated Al contact grid)	649	39.1	77.5	19.7*
P25 (optimized a-Si + evaporated Al contact grid)	636	39.5	79.5	20.0*
P15 (a-Si/SiO$_x$ + full-area metalization)	639	39.9	77.2	19.7*
P21 (non-passivated rear)	629	38.9	77.9	19.1

* independently confirmed at ISE Callab

The fabricated solar cells show open-circuit voltages V_{oc} up to 649 mV for P01, demonstrating the excellent Al-p^+ emitter quality and its effective surface passivation by amorphous silicon. The highest V_{oc} achieved for n-type silicon solar cells with full-area metalized Al-p^+ emitter before this work was started was V_{oc} = 627 mV [56]. For comparison, a solar cell with full-area metalized Al-p^+ emitter is also included in Table 4.1. This cell has been fabricated during this work and it shows solar cell parameters which are consistent with cell results published by others [56, 114]. In this work, n-type silicon solar cells with a-Si passivated Al-p^+ emitter have been introduced as a high-potential cell type. More recently, other groups have demonstrated a V_{oc} of 645 mV for n-type Si solar cells with an a-Si-passivated Al-p^+ emitter using 10 Ωcm n-type float-zone silicon material [114]. The corresponding cell efficiency was 19.5%. Cuevas et al. have estimated an ultimate V_{oc} limit of 641 mV for full-area screen-printed Al-p^+ emitters [54]. The surface-passivated Al-p^+ emitter developed in this work clearly outperforms this estimated V_{oc} limit.

The very high short-circuit current densities of the cells in the range J_{sc} = 39.1 - 39.9 mA/cm^2 confirm a very effective minority-carrier diffusion to the rear junction. For the best cell (cell P25 in Table 4.1) an energy conversion efficiency of 20.0% has been obtained, which was indepen-

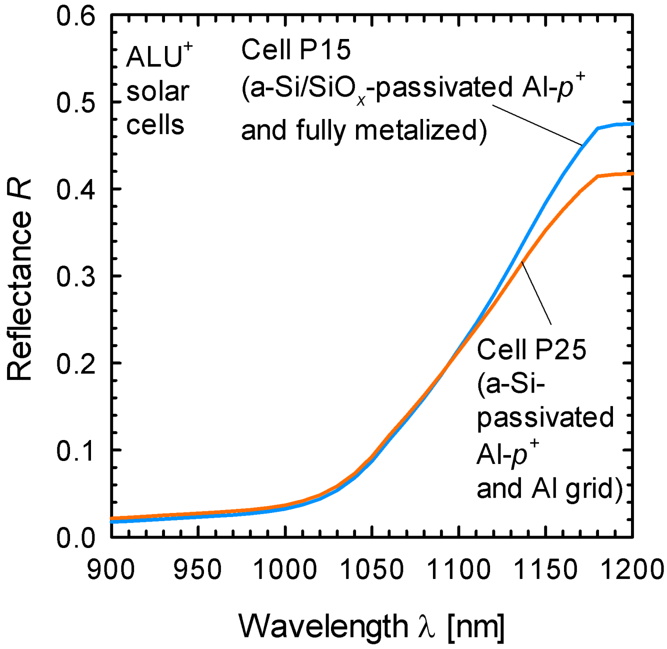

Figure 4.5.: *Comparison of the spectral reflectance R(λ) in the infrared wavelength range of cell P25 from Table 4.1 and Cell P15 from Table 4.1.*

dently confirmed at Fraunhofer ISE CalLab, Freiburg, Germany. This is the highest efficiency attained so far for n-type Cz silicon solar cells featuring an a-Si-passivated screen-printed Al-p^+ emitter. The solar cell with a-Si/SiO$_x$ passivation, local contact openings and a full-area metallization of the emitter surface reaches an independently confirmed cell efficiency of 19.7% (cell P15 in Table 4.1) and a high short-circuit current density of J_{sc} = 39.9 mA/cm^2, which is due to the increased internal rear reflection. Figure 4.5 shows the spectral reflectance of cell P15 and P25 of Table 4.1. Solar cell P15 with a-Si/SiO$_x$ passivation and a full-area metalized rear shows an increased reflectance in the wavelength range between 1100 and 1200nm. Figure 4.6 shows the internal quantum efficiency (*IQE*) calculated from the external quantum efficiency measured at 1/3 suns bias light intensity and the measured reflectance data of a standard n-type solar cell with a fully metalized unpassivated Al-p^+ rear emitter in comparison to the *IQE* of an ALU$^+$ solar cell featuring an a-Si passivated Al-p^+ emitter with a contact grid at the rear and an optimized FSF. High *IQE* values above 0.95 are achieved at wavelengths λ between 500 and 900 nm for both solar cells. The ALU$^+$ cell shows an increased *IQE* at $\lambda > 950$ nm due to the a-Si-passivated Al-p^+ emitter surface. Also a significantly higher *IQE* is obtained for the ALU$^+$ cell at < 500 nm, which can be explained by a reduced surface recombination at the front due to the 238 $\Omega/\square$ n^+ FSF enabling an easy-to-passivate low surface doping concentration of 3×10^{19} cm^{-3} [87, 110–112].

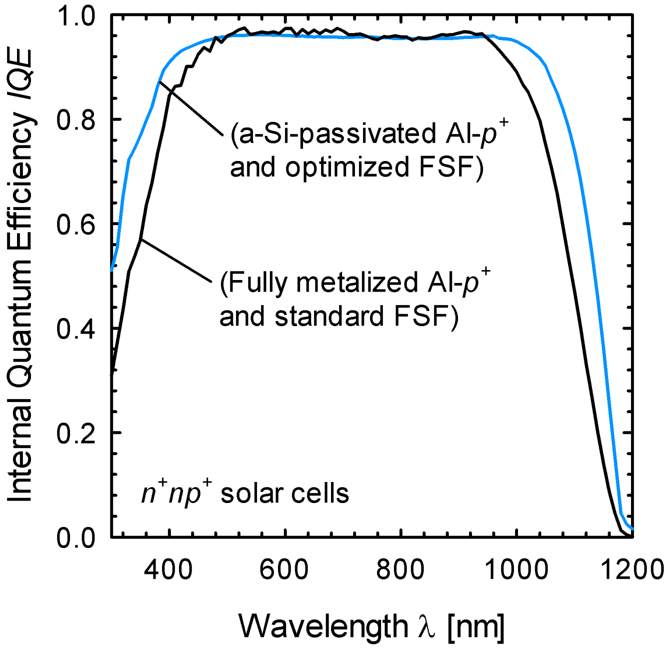

Figure 4.6.: *Comparison of the internal quantum efficiency of a standard n-type solar cell with a fully metalized unpassivated screen-printed rear Al-*p^+ *emitter and a solar cell with an a-Si-passivated screen-printed Al-*p^+ *rear emitter and an optimized FSF at the front.*

Figure 4.7 (a) shows an electroluminescence (EL) image [115,116] of an ALU$^+$ solar cell with a non-optimized metallization grid on the a-Si passivated Al-p^+ emitter with a finger spacing of 2 mm (corresponding to cell P01 from Table 4.1).

The large area fraction of the well-passivated emitter results in a high V_{oc} of 649 mV, whereas the EL signal drops significantly in between the fingers due to an increased series resistance. This results in a reduced fill factor *FF* of 77%. In comparison, Fig. 4.7 (b) shows an EL image of a solar cell with an optimized metalization grid on the Al-p^+ emitter with a reduced finger spacing of 1 mm (corresponding to cell P25 from Table 4.1).

A homogeneous EL signal over the entire cell area can be observed. Due to the higher metallization fraction, and thus increased recombination, a reduced V_{oc} of 640 mV is obtained. The optimized contact-grid geometry results, however, in an increased fill-factor *FF* of 79.5% and a record-high efficiency for this cell type of 20.0%.

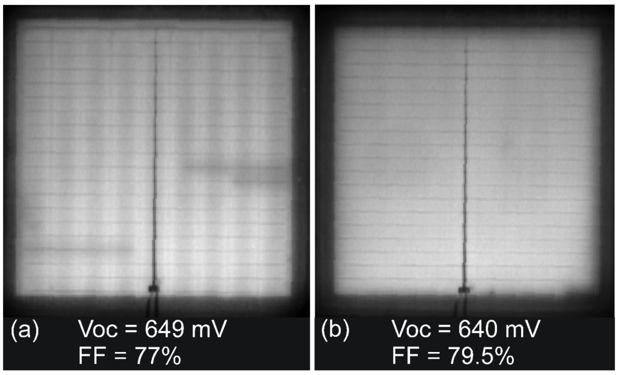

Figure 4.7.: *(a) Electroluminescence (EL) image at an applied voltage V_{appl} of 646 mV of an ALU$^+$ solar cell with a non-optimized Al metal grid at the rear (finger distance 2 mm) showing a decreased EL signal between the metalization fingers due to an increased series resistance. (b) EL image at an applied voltage V_{appl} of 644 mV of an ALU$^+$ solar cell with an optimized Al metal grid at the rear (1 mm finger distance) showing a homogeneous EL signal.*

Al_2O_3/SiN_x passivated rear emitter

The one-sun performance of the best n-type solar cell featuring an Al_2O_3/SiN_x passivated Al-p^+ rear emitter is shown in Table 4.2.

The solar cell features local contact openings and a full-area Al metalization of the Al_2O_3/SiN_x-passivated Al-p^+ emitter. The cell efficiency is 19.8%, which is slightly below that of the a-Si-passivated ALU$^+$ cell P25 of Table 4.1, which is mainly due to non-optimized contact openings at the rear resulting in a reduced fill factor of 76.4%. However, the high open-circuit voltage V_{oc} of 649 mV indicates an effective passivation of the p^+-emitter by the Al_2O_3/SiN_x stack, which is consistent with the J_{0e} measurements of Chapter 3. The high short-circuit current density of J_{sc} 39.9 mA/cm^2 is due to the increased reflection at the rear of the Al_2O_3/SiN_x-passivated cell.

TABLE 4.2.
SOLAR CELL PARAMETERS OF THE BEST AL_2O_3/SIN_x PASSIVATED CELL MEASURED UNDER STANDARD TESTING CONDITIONS (AM1.5G, 100 MW/CM^2, 25°C). THE APERTURE CELL AREA IS 4 CM^2.

Cell type	V_{oc} [mV]	J_{sc} [mA/cm^2]	FF [%]	η [%]
P15 (Al_2O_3/SiN_x)	649	39.9	76.4	19.8

4.2. Back-junction back-contact *n*-type solar cells with Al-p^+ emitter

Back-junction back-contact (BJBC) solar cells are one of the most promising high-efficiency solar cell concepts, showing conversion efficiencies above 22% in laboratory and production [1]. Due to the higher lifetimes of *n*-type compared to *p*-type Czochralski-grown (Cz) silicon, BJBC solar cells are usually fabricated on *n*-type Cz-Si [6] and consequently a p^+-emitter is needed for the formation of the *pn*-junction. Typically, a high-temperature boron diffusion is performed for the p^+-emitter formation. This boron-diffusion, however, is still a key issue in solar cell technology, as it is technologically demanding and tends to induce crystallographic defects in the bulk, degrading its recombination lifetime [29, 30]. In recent years, alternatives to the high-temperature boron diffusion have been developed, which might enable a simplified p^+-emitter formation [54, 56].

This Section presents a BJBC solar cell featuring the screen-printed and surface-passivated Al-doped p^+ emitter developed in this work. In Section 4.2.1, the solar cell structure is introduced, while in Section 4.2.2 the processing sequence is explained in detail. In Section 4.2.3, the current-voltage characteristics of the fabricated cells are presented and discussed. Using two dimensional device simulations, a realistic efficiency limit of the presented BJBC cell structure is determined, and finally, using numerical simulations, a loss analysis of the fabricated cells is carried out.

4.2.1. Solar cell structure

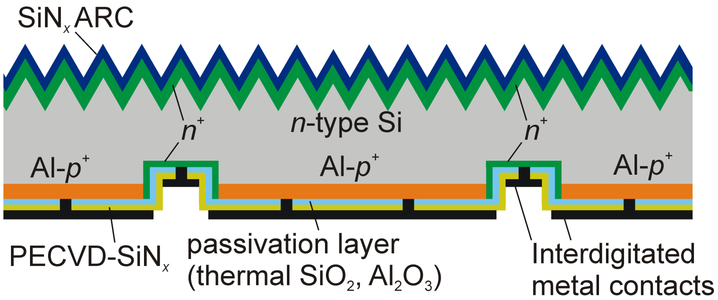

Figure 4.8.: *Schematic of our back-junction back-contact n-type Si solar cell featuring a screen-printed and surface-passivated Al-p^+ rear emitter.*

Figure 4.8 shows a schematic of our novel *n*-type BJBC solar cell. This cell type is chracterized by local Al-p^+ emitter and local n^+ base regions at the rear of the cell. The front side of the cell features a weak phosphorus-diffused n^+ FSF and a random pyramid texture.

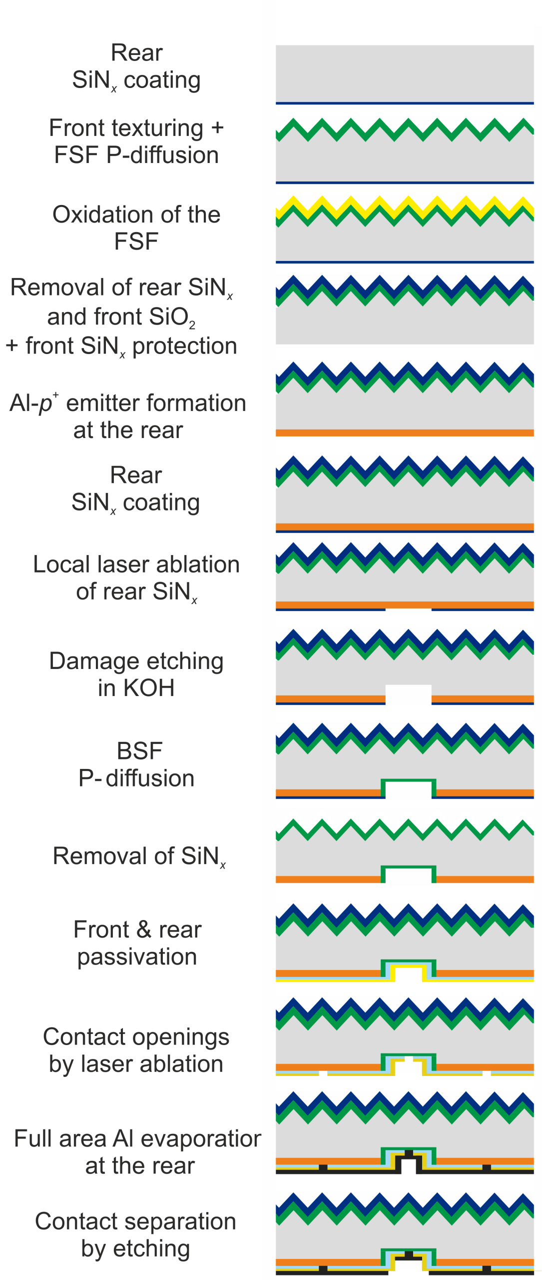

Figure 4.9.: *Processing sequence of the n-type BJBC silicon solar cell featuring a screen-printed Al-*p^+ *rear emitter.*

4.2.2. Processing sequence

The processing sequence of the BJBC solar cell is depicted in Figure 4.9. As base material 150 μm thick (100)-oriented phosphorus-doped Czochralski-grown (Cz) silicon wafers with a resistivity of $\sim$1.8 Ωcm are used. After cleaning and damage etching in a 50% KOH solution at 90°C for 10 min, where about 15 μm of the Si is etched, a 150 nm thick PECVD-SiN$_x$ protection layer with a refractive index $n = 2.05$ is deposited on the rear of the wafer. Then, the front surface is textured with random pyramids in a 5% solution of KOH plus $\sim$100 ml of isopropanol at 90°C for 60 min. Afterwards, a 100 $\Omega/\Box$ POCl$_3$ diffusion is performed at the front at 850°C (20 min at 850°C in POCl$_3$ gas plus 15 min drive-in in nitrogen) using a *LPT Sirius 9000* quartz tube furnace. Subsequently, the n^+ diffused region undergoes a wet oxidation at 850°C (120 min wet oxidation plus 30 min dry oxidation) also by using the *LPT Sirius 9000* quartz tube furnace. During this oxidation the phosphorus concentration peak is mostly oxidized, resulting in an n^+ front surface field (FSF) with an easy-to-passivate surface doping concentration of 7×10^{19} cm^{-3} and a sheet resistance of $\sim$250 $\Omega/\Box$. The remaining oxide at the front and the SiN$_x$ at the rear are removed from the wafer by means of a short HF dip (5% HF, 10 min). The textured front side is then covered by a 200 nm SiN$_x$ layer (n = 2.05 deposited at 400°C) to protect the front surface during the back-etching procedure of the rear emitter.

After screen-printing and firing of the Al-p^+ rear emitter, the residual Al paste and the Al-Si eutectic are removed in a boiling 37% solution of HCl and the Al-p^+ emitter is etched back by 2-3 μm in a 50% KOH solution at 70°C. For the laser structuring of the base region we deposit a 150 nm SiN$_x$ layer (n = 2.05) on the Al-p^+ emitter surface. The base region is defined by ablation of the SiN$_x$ from the emitter surface using a *LUMERA LASER Super Rapid* picosecond laser [117]. Pulse lengths of 9 ps and a pulse energy of 8.3 μJ at a wavelength of 532 nm are applied for the ablation. Then, the samples undergo a KOH etching (50% KOH at 90°C for 10 min), where about 20 μm of the silicon is etched back and the heavier doped 58 $\Omega/\Box$ n^+ back surface field (BSF) is diffused into the base region (40 min at 850°C in POCl$_3$ gas plus two drive-in phases: (i) 15 min at 850°C in nitrogen and, (ii) for additional 15 min at 875°C in nitrogen). After the BSF P-diffusion we remove the protective SiN$_x$ from the front and rear by means of a dip in a 5% solution of HF for 10 min. Prior to surface passivation, the cells receive an extra RCA cleaning.

Two types of BJBC solar cells have been fabricated. For type 1, both surfaces are passivated by a 10 nm thick thermal SiO$_2$ grown at 800°C for 75 min using the *LPT Sirius 9000* quartz tube furnace, which is capped by a 70 nm thick PECVD-SiN$_x$ layer with a refractive index of n = 1.9 at the front and by a 150 nm PECVD-SiN$_x$ (n = 1.9) layer at the rear. Type 2 has a 10 nm thick PECVD-SiN$_x$ (n = 2.4) passivation layer at the front, capped by a 70 nm thick PECVD-SiN$_x$ (n = 1.9) layer acting as antireflection coating. The rear is passivated by a 20 nm thick layer of ALD-Al$_2$O$_3$ deposited at 225°C with a 150 nm thick PECVD-SiN$_x$ (n = 1.9) layer on top deposited at 400°C. After front- and rear-side passivation we open the contact points at the rear by laser ablation of the dielectric using the *LUMERA LASER Super Rapid* picosecond laser. For the ablation of the dielectric we use a pulse energy of 5 μJ. Contact points of $\sim$20 μm in diameter at a distance of 30 μm to each other were opened. We then evaporate 15 μm of Al on the rear side of the cell and on top of the Al layer we deposit $\sim$500 nm of SiO_2. The Al evaporation and the SiO_2 deposition was performed in an *Blazers BAK EVO* batch vacuum coating system. Contact separation is realized by chemical etching of the Al as described elsewhere [118]. The width of the Al-p^+ region is 2500 μm and of the n^+ region 300 μm. As a consequence, the emitter covarage of the rear amounts to 85%.

4.2.3. Solar cell results

Table 4.3 shows the one-sun performance of the best type 1 and type 2 BJBC solar cells. The measurements were carried out using a shadow mask with an aperture area of 3.97 cm^2. On this designated cell area conversion efficiencies of 18.9% for type 1 and 19.0% for type 2 solar cells were measured under standard testing conditions (AM1.5G spectrum, 100 mW/cm^2, 25°C).

TABLE 4.3.
SOLAR CELL PARAMETERS MEASURED UNDER STANDARD TESTING CONDITIONS (AM1.5G, 100 MW/CM^2, 25°C). THE APERTURE CELL AREA IS 3.97 CM^2.

Cell type	V_{oc} [mV]	J_{sc} [mA/cm^2]	FF [%]	η [%]
1 (SiO_2 front and rear)	637	37.5	79.0	18.9
2 (SiN_x front and Al_2O_3 rear)	636	37.9	78.7	19.0

These results prove that the screen-printed Al-p^+ emitter is suitable for the application in advanced BJBC solar cells and that it is a realistic alternative to the boron-diffused p^+ emitter. Nevertheless, the measured conversion efficiencies are still below that of BJBC solar cells with boron-diffused emitters [19,20]. In order to determine a realistic efficiency potential of the introduced solar cell structure and to analyze the limitations in conversion efficiency of the fabricated solar cells, we performed two-dimensional numerical simulations using the conductive boundary (CoBo) model, which has recently been introduced by Brendel [119]. The CoBo model characterizes diffused layers by their sheet resistances and diode saturation current densities.

Figure 4.10 shows a unit cell of the simulated device together with all input parameters including the geometry parameters, the saturation current density contributions of the front J_{0FSF}, the emitter J_{0e}, the BSF J_{0BSF}, the metalized regions $J_{0e.contact}$, $J_{0BSF.contact}$ and the bulk lifetime τ_{bulk}. Also included are the base resistivity, contact resistances $R_{e.contact}$, $R_{BSF.conatct}$ and the photogeneration rate G. The geometry parameters (cell thickness and pitch) of the simulated cell are identical to that of the fabricated cells. As the CoBo model does not treat optics the following approximated generation rate G for device modeling is used [120]:

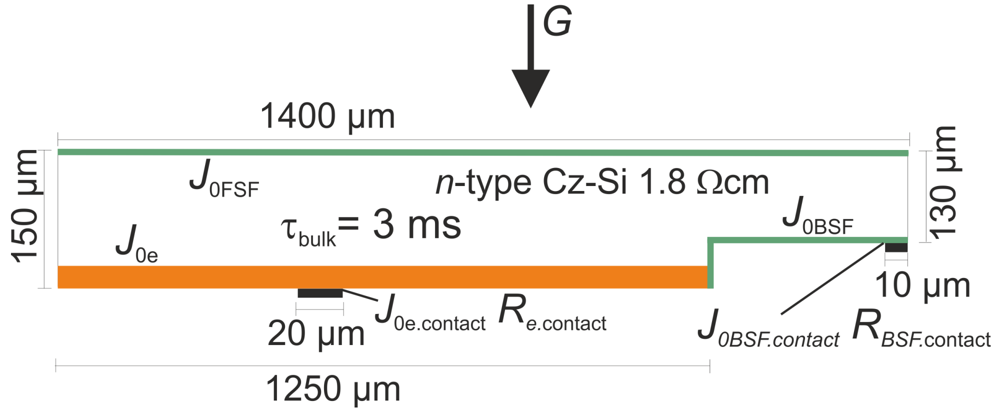

Figure 4.10.: *2D representation of a unit cell of the simulated BJBC solar cell showing the geometrical and electrical input parameters of the simulation.*

$$G(y) = \beta\left(449.4e^{\frac{-(w-y)}{0.5\mu m}} + 332.4e^{\frac{-(w-y)}{4\mu m}} 19.23e^{\frac{-(w-y)}{25\mu m}} + 1.173\right). \tag{4.1}$$

The factor β is a scaling factor which scales the generation rate G to a value of 95% of the Lambertian limit (i.e., fully diffusely reflecting surfaces) [119] at a given cell thickness w. For simplicity w is assumed to be constant. To determine a realistic conversion efficiency limit, the simulations have been carried out using measured saturation current density and sheet resistance data from literature [110, 112, 121]. The saturation current densities used for the simulations are summarized in Table 4.4. J_0 data which could not be found in the literature were determined in this work using lifetime measurements (see Chapter 3). As passivation layers the same passivation schemes which have been applied experimentally to the cells are considered: (1) a thermally grown SiO_2 at the rear and front plus SiN_x capping layer and (2) a PECVD-SiN_x at the front and an ALD-Al_2O_3 at the rear.

Table 4.5 shows simulated parameters of the illuminated current-voltage curves for the two considered passivation schemes. The thermally grown SiO_2 passivation [scheme (1)] shows the highest conversion efficiency of 21.6%. Free energy loss analysis [119] shows that this is mainly due to the fact that both the n^+-doped as well as the p^+-doped surfaces can be effectively passivated by the oxide and thus the power loss is minimized in both regions. The ALD-Al_2O_3 passivation of the rear combined with a SiN_x passivation of the front [scheme (2)] shows a conversion efficiency potential of 21.3%. The Al_2O_3 has the best passivation quality on the Al-p^+ emitter and thus shows a higher V_{oc} compared to scheme (1), however, the main losses are due to the poorer passivation at the front by the SiN_x compared to the SiO_2/SiN_x stack coming along with a lower J_{sc}. The V_{oc} of all simulated cells is ultimately limited by recombination losses in the Al-p^+ emitter.

The experimental V_{oc} and J_{sc} data shown in Table 4.3 are significantly below the simulated data in Table 4.5. Additional simulations have shown that only a simultaneous deterioration of the

TABLE 4.4.
MEASURED SATURATION CURRENT DENSITIES J_0 USED FOR THE SIMULATION OF THE CONVERSION EFFICIENCY LIMIT OF OUR BJBC CELL.

(1) Thermal SiO_2 (front and rear)	Passivation layer	J_0 [fA/cm^2]	Ref.
J_{0FSF} (250 $\Omega/\square$)	SiO_2/SiN_x	30	[110]
J_{0BSF} (50 $\Omega/\square$)	SiO_2/SiN_x	50	[110]
J_{0e} (Al-p^+ 75 $\Omega/\square$)	SiO_2/SiN_x	180	this work
(2) SiN_x (front) and Al_2O_3 (rear)			
J_{0FSF} (250 $\Omega/\square$)	SiN_x	50	[110]
J_{0BSF} (50 $\Omega/\square$)	Al_2O_3/SiN_x	200	this work
J_{0e} (Al-p^+ 75 $\Omega/\square$)	Al_2O_3/SiN_x	160	this work
Metalized regions			
$J_{0BSF.contact}$ (50 $\Omega/\square$)	-	500	[121]
$J_{0e.contact}$ (75 $\Omega/\square$)	-	1000	[112]

front and rear recombination can account for the V_{oc} and J_{sc} reduction. An excellent agreement of the experimental I-V curves and the simulated one is achieved for J_{0FSF} = 100 fA/cm^2 and J_{0e} = 750 fA/cm^2. We attribute this reduced J_{0e} to degradation of the lifetime in the bulk of the Al-p^+ emitter during P-diffusion (see Chapter 2).

TABLE 4.5.
SIMULATED PARAMETERS OF THE BJBC CELLS UNDER STANDARD TESTING CONDITIONS (AM1.5G, 100 MW/CM^2, 25°C) .

Cell type	V_{oc} [mV]	J_{sc} [mA/cm^2]	FF [%]	η [%]
1 (SiO_2/SiN_x front and rear)	671	40.3	80.1	21.6
2 (SiN_x front and Al_2O_3/SiN_x rear)	668	39.7	80.3	21.3

4.3. Industrial-type *n*-type solar cells with screen-printed Al-p^+ emitter

This Section deals with *n*-type industrial-type solar cells including a screen-printed Al-p^+ rear emitter, a fully screen-printed front and rear metalization and a selective front surface field. In Section 4.3.1, the solar cell structure is introduced and the processing sequence is explained. In Section 4.3.2, the solar cell results are presented and discussed. We analyze the current-voltage (*I*-*V*) characteristics, the dark *I*-*V* curves and the J_{sc}-V_{oc} curves. In addition, camera-based EL measurements are performed.

4.3.1. Solar cell structure and processing sequence

Figure 4.11 shows a schematic of an industrial-type *n*-type solar cell featuring a screen-printed Al-p^+ rear emitter and a local deep diffusion (LDD) beneath the screen-printed Ag front contact grid plus a weak diffusion with a low surface doping concentration between the contact fingers. The LDD beneath the Ag contact grid serves as an effective front surface field (FSF) to the minority charge carriers and thus reduces the recombination at the silicon/metal interface.

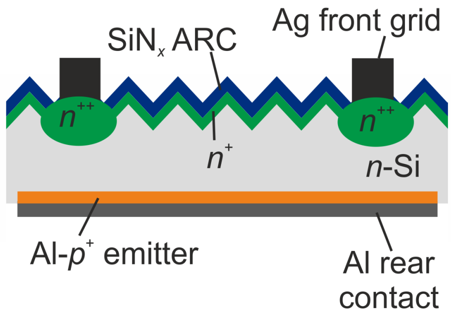

Figure 4.11.: *Schematic of the industrial-type solar cell featuring a screen-printed Ag front grid and a fully metalized Al rear side.*

In addition, the LDD provides an excellent ohmic contact of the screen-printed Ag fingers to the FSF. The weak diffusion between the non-metalized area at the front on the other hand, shows less recombination in the bulk and at the surface of the FSF [87, 110]. The processing sequence of the solar cell is shown in Figure 4.12 and will be described in the following.

As base material 12.5 × 12.5 cm^2 pseudo-square (100)-oriented phosphorus-doped Czochralski-grown silicon wafers with an initial thickness of ∼180 μm and a resistivity of ∼5 Ωcm are used. After depositing a 150 nm thick SiN$_x$ layer (n = 1.9, deposited at 500°C) onto the rear surface, random pyramids are formed at the front using a 5% solution of KOH plus ∼100 ml of isopropanol at 90°C for 60 min.

Afterwards, a phosphorus diffusion is performed, resulting in an n^+ region with a sheet resistance of R_{sh} = 80 Ω/□. The SiN$_x$ at the rear and the phosphorus silicate glass (PSG) at the front

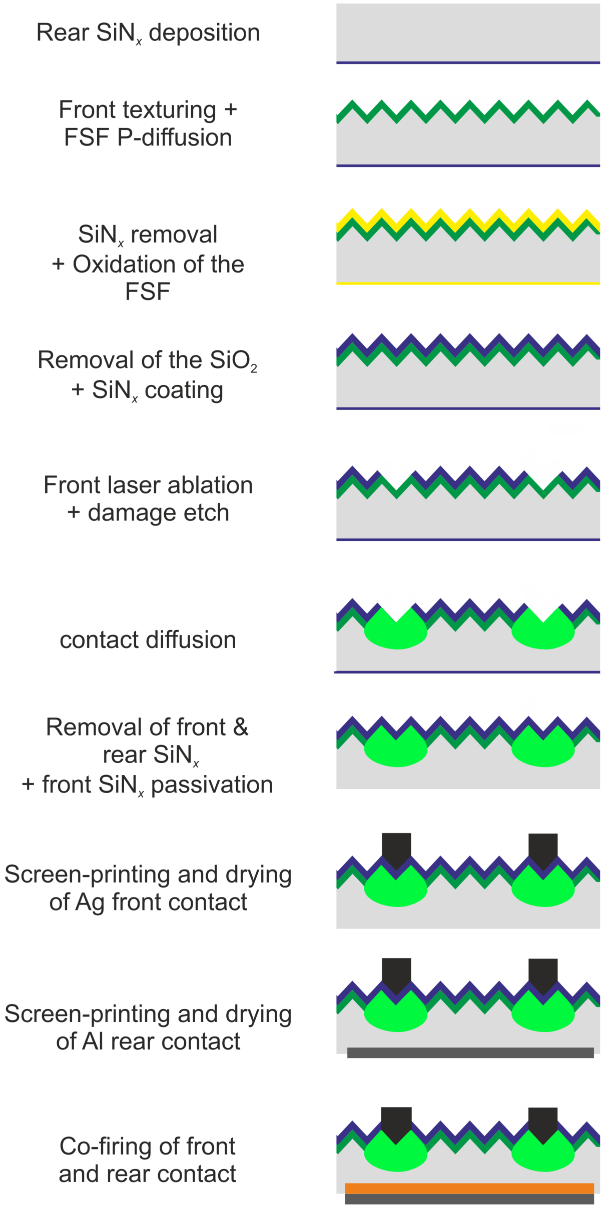

Figure 4.12.: *Processing sequence of the industrial-type solar cell featuring a screen-printed Ag front grid and a fully metalized Al rear side.*

are removed from the wafer by applying a dip in 1% HF solution for 30s. As already described in Section 4.1.2, a wet oxidation at 850°C (120 min wet plus 30 min dry oxidation) is applied to the initial diffusion of this solar cell, which results in a sheet resistance R_{sh} = 140 $\Omega/\Box$ and a surface doping concentration as low as (2-4)$\times 10^{19}$ cm^{-3}. The diffusion and the oxidation processes were performed in an *LPT Sirius 9000* quartz tube furnace.

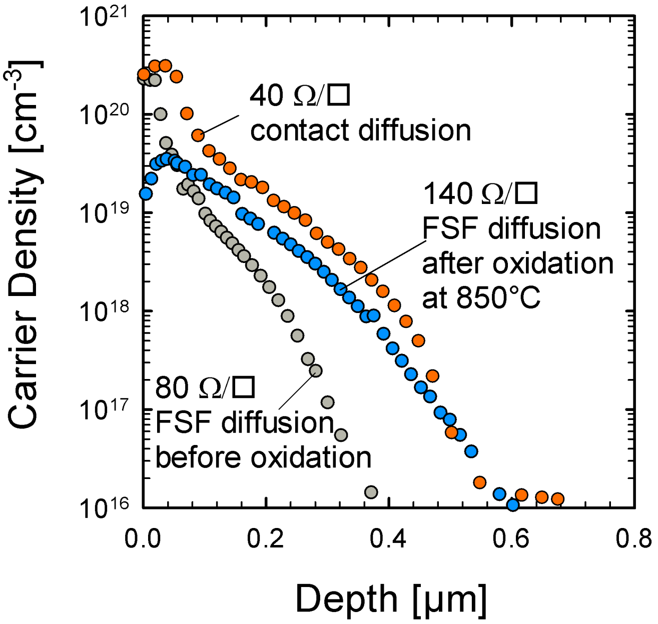

Figure 4.13.: *Doping profiles of the front surface field (FSF) phosphorus diffusion before and after a wet oxidation at 850°C as well as of the local deep contact diffusion, measured by ECV profiling.*

In order to protect the wafer surfaces during laser processing and contact diffusion the oxide is removed from the surface by dipping the Wafers in 5% HF for 10 min and subsequently the front and rear side of the wafer are coated by a 150 nm SiN$_x$ layer (n = 2.05). As a next step, using a *Coherent AviaX* nanosecond laser, the SiN$_x$ is removed from the textured front side at the positions of the LDD. The laser has a wavelength of 355 nm and a pulse length of 20 ns. We have applied a pulse energy of $\sim$ 25 μJ to remove the SiN$_x$ layer from the textured surface. Damage etching for 2-3 min in a 50% KOH solution at 90°C removes 3-6 μm of the silicon at the laser-ablated areas. This is necessary as the laser induces crystallographic defects which act as recombination centers for the generated charge carriers. A phosphorus diffusion with a resulting sheet resistance of R_{sh} = 40 Ω/□ is performed into the ablated and damage-etched areas. Figure 4.13 shows the doping profiles of the applied phosphorus diffusions at the front measured with the electrochemical capacitance voltage (ECV) method. Subsequent to the contact diffusion, the protective SiN$_x$ layer is removed from the surfaces by a dip in 40% HF for 10 min and the wafers receive an RCA cleaning before the front side of the wafer is passivated by a 70 nm thick SiN$_x$ layer with a refractive index of n = 2.05 deposited at 400°C. All SiN$_x$ coatings of this solar cell were performed in an industrial *Roth & Rau SiNA* PECVD reactor.

As the surface shows a different reflection in the laser-ablated regions compared to the textured neighbouring regions the ablated and damage-etched grid structure itself is used as alignment mark during screen-printing of the Ag front grid. Figure 4.14 shows an optical micrograph of a laser-ablated and damage-etched region with a screen-printed finger inside the contact region. The SiN_x-passivated cell area appears in blue, whereas the laser-ablated and deeply diffused region appears in green color. The bright contrast within the LDD region represents the screen-printed Ag finger.

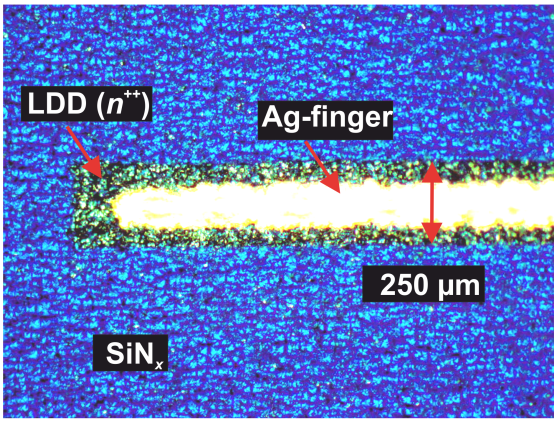

Figure 4.14.: *Optical micrograph of a Ag finger screen-printed onto an LDD region.*

A glass-fritted Ag paste (DuPont PV149) is screen-printed onto the front of the cell and is dried at 150°C for 4 min in a *Centrotherm DO-HTO-5.200-210* belt dryer. Afterwards, an Al paste (Ferro 53-121) is screen-printed onto the rear of the solar cell and is dried at 150°C for 10 min. Finally, the solar cells are co-fired using a *Centrotherm DO-FF-8.600-300* infrared conveyor belt furnace with 8 firing zones. All screen-printing pastes used for the fabrication are commercially available pastes. Pre-firing temperatures of 520°C / 540°C / 560°C / 580°C were applied in the first 4 zones in order to burn the organic solvents in the pastes (see Section 1.2.3). The contact co-firing has been performed at a peak-firing set temperature of 840°C / 840°C in the last 2 firing zones. During the firing step the Ag paste contacts the LDD region through the SiN_x layer at the front of the solar cell (for details see Ref. [122]) and the Al-p^+ emitter is formed as described in Section 1.2.3.

4.3.2. Solar cell results

The one sun performance of our best all-screen-printed industrial-type solar cell featuring an Al-p^+ rear emitter and a selective FSF at the front measured under standard testing conditions (AM1.5G spectrum, 100 mW/cm^2, 25°C) is shown in Table 4.6. The Table shows two measurements of the same cell measured with and without a mask. The open-circuit voltage amounts to $V_{\text{oc}} = 625$ mV and the short circuit current density is $J_{\text{sc}} = 36.6$ mA/cm^2. The high fill factor of $FF = 78.8\%$ indicates low contact resistance of the screen-printed Ag fingers to the LDD and also a homogeneously fired Al-p^+ emitter at the rear without any indication of shunting. These solar cell parameters result in a stable and independently confirmed energy conversion effciency of η = 18.0%, which was the highest efficiency of this cell type at the time of the publication [123].

TABLE 4.6.
SOLAR CELL PARAMETERS OF THE SAME CELL MEASURED WITH AND WITHOUT MASK (STANDARD TESTING CONDITIONS).

Cell area	V_{oc} [mV]	J_{sc} [mA/cm^2]	FF [%]	η [%]
100 cm^2 (mask)	625	36.6	78.8	18.0*
146.5 cm^2 (no mask)	633	35.8	76.8	17.4

* independently confirmed at ISE Callab

The current-voltage (I-V) characteristic of the solar cell is traditionally described as an ideal diode in parallel with a constant current source (see e.g. Refs. [78, 124, 125]). The parameters describing the ohmic losses and the leakage currents (R_{shunt}, R_{serial}) and the recombination losses of emitter, base and space charge region of the pn-junction (J_{01}, J_{02}) have been extracted in accordance with the 2-diode model from least-square fits of measured current-voltage characteristics of an illuminated I-V, a dark J-V, and a J_{sc}-V_{oc} curve. Furthermore, the pseudo fill factor FF_0 is obtained using the J_{mpp} and V_{mpp} values from the J_{sc} - V_{oc} curve. The FF_0 corresponds to a fill factor without any influence of series resistances and thus it is a good indicator for fill factor losses caused by shunts. The fit parameters were extracted using the computer program SCAN (**S**olar **C**ell **AN**alysis) [126]. SCAN is developed at the ISFH for the combined analysis of different measurement techniques and allows for a quantitative global and local loss analysis of crystalline silicon solar cells. Figure 4.15 (a) shows the measured and fitted J_{sc} - V_{oc} curves, (b) the dark J-V characteristics, and (c) the illuminated J-V curves. As the ideality factor of the solar cell at the maximum power point (MPP) is $n_{MPP} \cong 1.1$, the measured curves can be better fitted by the two-diode model using one single parameter set. The extracted fit parameters of the 2-diode model are shown in Table 4.7.

For the analyzed solar cell a saturation current density J_{01} of 910 fA/cm^2 is determined which is slightly higher than the measured saturation current densities from non-passivated Al-p^+ emitter (800 ± 200) fA/cm^2 (see Section 3.3), and thus the higher J_{01} is attributed to enhanced recombination at the front side of the solar cell. J_{02} of the second diode is determined to be J_{02} = 5.6 nA/cm^2. The series resistance is R_{serial} = 0.71 Ωcm^2 proving a good ohmic contact of the screen-printed Ag grid to the n^{++} region. The high shunt resistance of R_{shunt} = 25 kΩcm^2 indicates a homogeneous Al-p^+ emitter without any interrupts which otherwise would cause shunting at the rear. This is additionally supported by the high pseudo fill factor FF_0 = 82.9%.

From these results it can be concluded that the conversion efficiency of this solar cell is mainly limited by J_{01} and R_{ser} and secondly by J_{02}. A likely explanation for an increased recombination

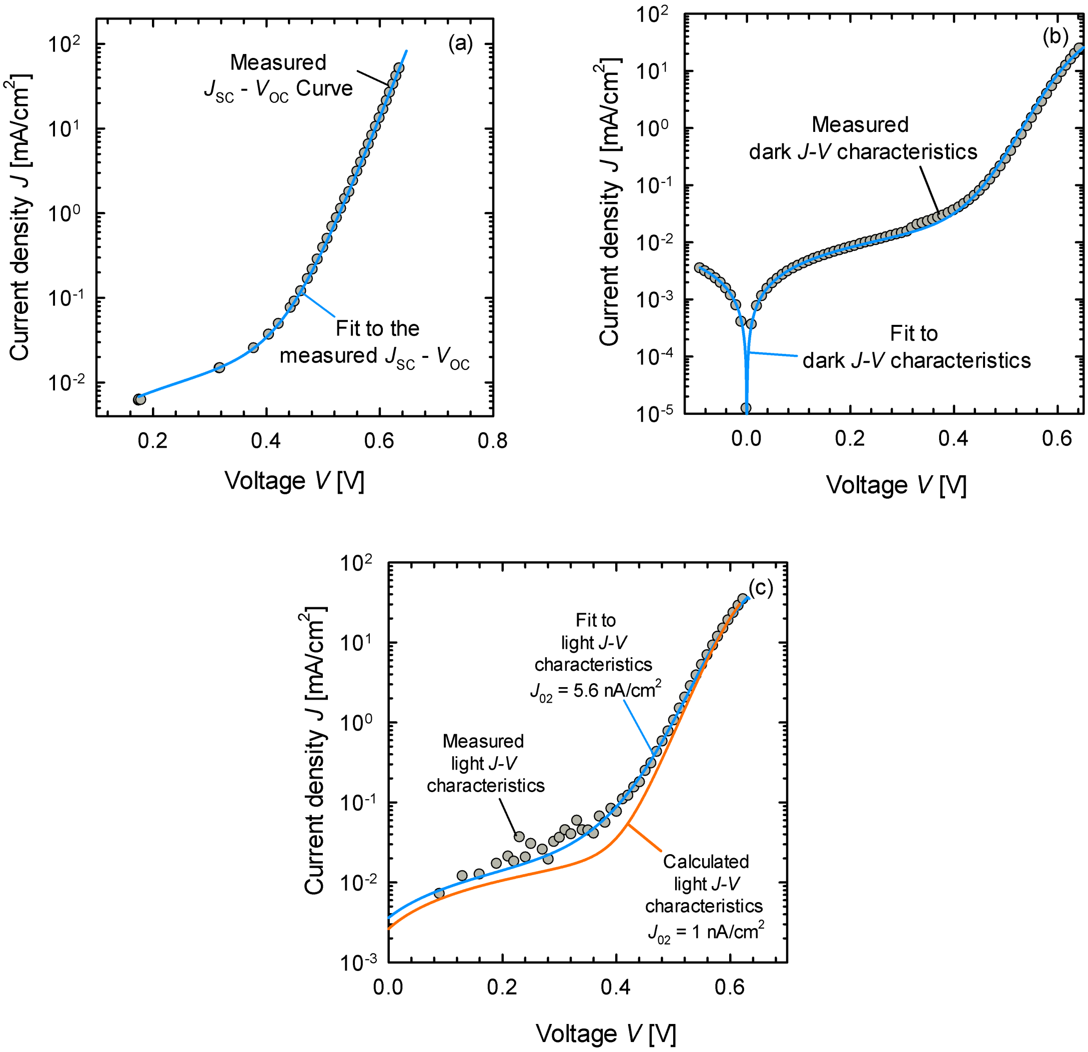

Figure 4.15.: *Measured and calculated current-voltage characteristics: (a) J_{sc} - V_{oc}, (b) dark J-V, and (c) illuminated J-V characteristic.*

TABLE 4.7.
FIT PARAMETERS OF THE MEASURED SOLAR CELL CHARACTERISTICS SHOWN IN FIGURE 4.15.

Cell area	J_{01} [fA/cm^2]	J_{02} [nA/cm^2]	R_{shunt} [kΩcm^2]	R_{serial} [Ωcm^2]	FF_0 [%]
100 cm^2 (mask)	910	5.6	25	0.71	82.9

at the front of the solar cell (increasing the J_{01} value) is an insufficient damage etching of the laser-ablated LDD regions at the front.

The relatively high pseudo fill factor FF_0 = 82.9% in comparison to the the measured fill factor of FF = 78.9% suggests that the main fill factor losses are due to series resistance losses. However, as the series resistance is determined to be only 0.71 Ωcm^2, a fill factor reduction solely due to a high series resistance can be excluded. Figure 4.7 (c) also includes a calculated I-V curve with a decreased J_{02} value of 1 nA/cm^2. The lower J_{02} value of the second diode would increase the FF about 0.5% absolute. From this result we conclude that the extracted J_{02} value of 5.6 nA/cm^2 is in a moderate range and has only a minor effect on the conversion efficiency of the solar cell. We also expect the bulk lifetime of the n-type Cz-Si to be independent of the injection level. As the passivated surfaces of this solar cell are highly doped, an injection dependency of the surface recombination velocity can also be excluded. Thus, we attribute the origin of the slightly increased J_{02} value to enhanced recombination within the space charge reagion of the emitter at the rear.

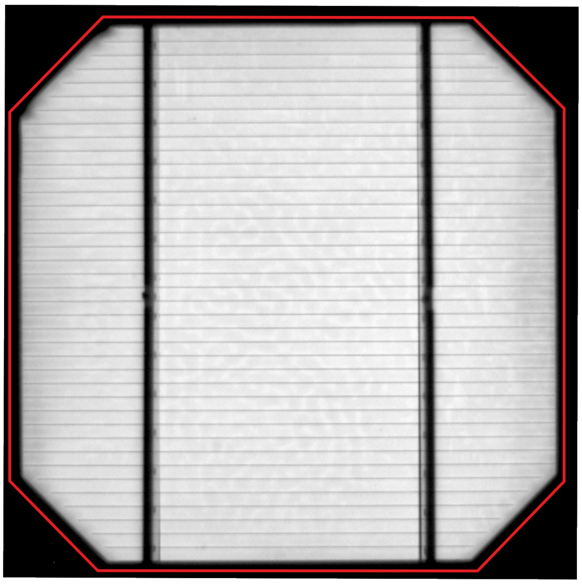

Figure 4.16.: *Electroluminescence image of the solar cell of Table 4.6 recorded at an applied voltage V_{appl} of 553 mV.*

As indicated in Table 4.6, the measured solar cell has a total cell area of 146.5 cm^2. However, it has also been measured at an aperture area of 100 cm^2. Figure 4.16 depicts an electroluminescence (EL) image of the solar cell measured at an applied voltage V_{appl} of 553 mV which equals the voltage at the maximum power point (V_{mpp}). This image clearly shows that the luminescent area does not equal the total cell area which is marked by a red frame. As the screen-printed region and thus the emitter at the rear does not cover the entire cell area, an edge of $\sim$1.5 mm width around the entire cell remains completely dark in the EL image, which corresponds to

$\sim$4% of the total cell area. This dark region can be attributed to extremely high charge carrier recombination reducing the V_{oc} and in particular the J_{sc} of the solar cell, which is consistent with the solar cell parameters shown in Table 4.6. This area cannot be completely avoided due to handling issues and deviating wafer dimensions. The non-active cell-area could be reduced by printing the Al paste closer to the wafer edge, requireing a new screen design, by an improved control of the wafer dimensions (reduced scattering in wafer dimensions), or by passivation of the edge area, e.g. by SiN_x or Al_2O_3

4.4. Industrial-type ALU$^+$ solar cells

This Section deals with an industrial-type n-type Si solar cell including a screen-printed and passivated Al-p^+ rear emitter and a screen-printed Ag front metalization. In Section 4.4.1, the solar cell structure is introduced and the processing sequence is explained. In Section 4.4.2, the solar cell results are presented and discussed.

4.4.1. Solar cell structure and processing sequence

Figure 4.17 shows a schematic of an industrial-type n-type Si solar cell featuring a screen-printed and passivated Al-p^+ rear emitter, screen-printed Ag front contact grid plus evaporated Al rear metalization. The rear emitter surface is passivated with an Al_2O_3/SiN_x stack.

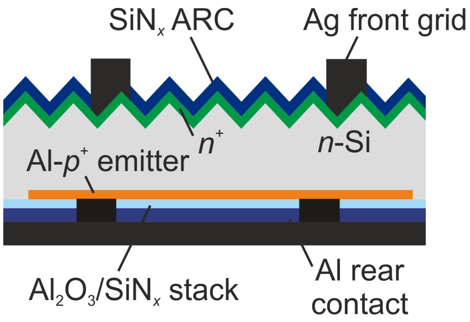

Figure 4.17.: *Schematic of the industrial-type ALU$^+$ solar cell featuring a screen-printed Ag front grid and a screen-printed and passivated Al-p$^+$ rear emitter.*

The processing sequence is depicted in Figure 4.18 and will be described in the following.

As base material 10 × 10 cm^2 (100)-oriented phosphorus-doped Czochralski-grown silicon wafers with an initial thickness of 180 μm and a resistivity of 1.8 Ωcm are used. After depositing a 150 nm thick protective SiN_x layer (n = 1.9, deposited at a set temperature of 500°C) onto the rear surface using plasma-enhanced chemical vapor deposition (PECVD) in an inline system (*SiNA, Roth & Rau*), random pyramids are formed at the front using a 5% solution of KOH plus ∼100 ml of isopropanol at 90°C for 60 min.

Afterwards, a phosphorus diffusion is performed at the front using an *LPT Sirius 9000* quartz tube furnace, resulting in an n^+ FSF with a sheet resistance of $R_{sh} = 58\ \Omega/\square$ (40 min at 850°C in $POCl_3$ gas plus two drive-in phases: (i) 15 min at 850°C in nitrogen and (ii) for additional 15 min at 875°C in nitrogen). The SiN_x at the rear and the phosphorus silicate glass (PSG) at the front are removed from the wafer by applying a dip in a 40% HF solution for 5 min. Subsequently, the wafers are coated by a 150 nm thick SiN_x layer with a refractive index of n = 1.90 at the front side using an inline-PECVD system (*SiNA, Roth & Rau*) to protect the surface during the later back-etching procedure of the rear emitter.

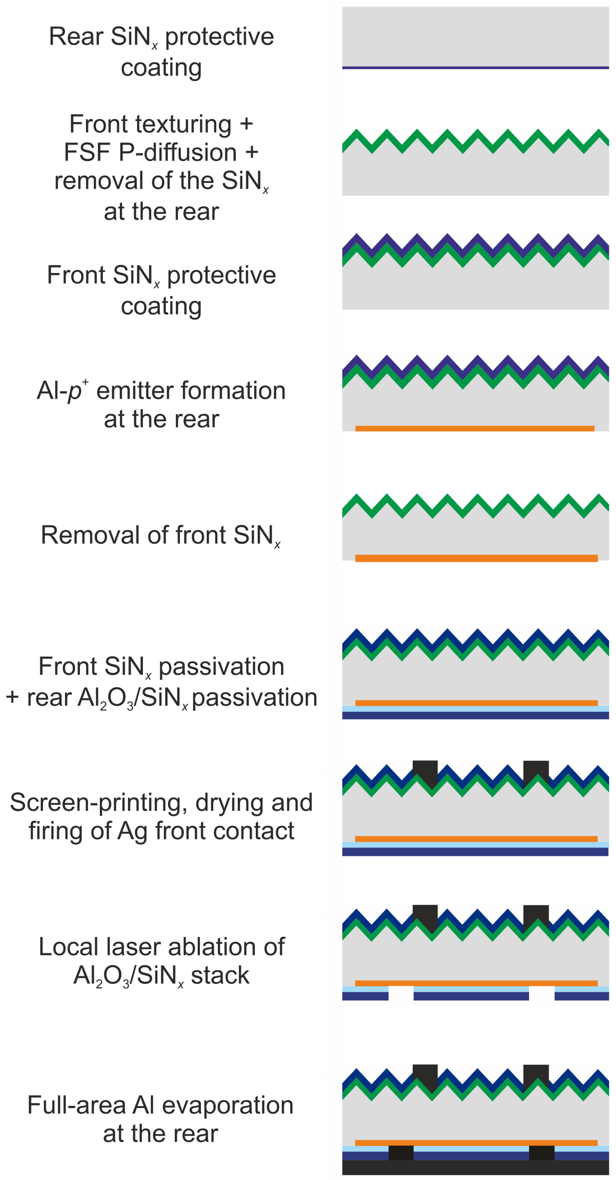

Figure 4.18.: *Processing sequence of the industrial-type ALU$^+$ solar cell.*

A non-fritted Al paste (Ferro 5540) is screen-printed onto the rear of the cell and is dried at 150°C for 10 min in a *Centrotherm DO-HTO-5.200-210* belt dryer. Subsequently, the solar cells are fired using a *Centrotherm DO-FF-8.600-300* infrared conveyor belt furnace. Pre-firing temperatures of 520°C / 540°C / 560°C / 580°C were applied in the first 4 zones of the furnace in order to burn the organic solvents in the paste (see Section 1.2.3). The Al-p^+ emitter firing was performed at a peak-firing set temperature of 800°C / 800°C in the last 2 firing zones at a belt speed of 2000 mm/min.

After screen-printing and firing of the Al-p^+ rear emitter, the residual Al paste and the Al-Si eutectic are removed in a boiling 37% solution of HCl and the Al-p^+ emitter is etched back by 2-3 μm in a 50% KOH solution at 70°C.

In the next step, the protective SiN_x layer is removed from the front side using a 40% HF solution for 5 min and the cells receive an extra RCA cleaning prior to the surface passivation. The rear is passivated by a 20 nm thick layer of plasma ALD-Al_2O_3 in an *Oxford Insturments FlexAL™* reactor deposited at 225°C with a 150 nm thick PECVD-SiN_x (n = 2.05) layer on top deposited at 400°C. The front is passivated by a 70 nm thick SiN_x layer with a refractive index of n = 2.05 deposited at 400°C. The SiN_x depositions performed in an industrial *Roth* & *Rau SiNA* PECVD reactor.

After front and rear-side passivation, a glass-fritted Ag paste (DuPont PV149) is screen-printed onto the front of the cell and is dried at 150°C for 4 min in a *Centrotherm DO-HTO-5.200-210* belt dryer. Then, the front contacts are fired using a *Centrotherm DO-FF-8.600-300* infrared conveyor belt furnace. Pre-firing temperatures of 520°C / 540°C / 560°C / 580°C were applied in the first 4 zones in order to burn the organic solvents in the pastes (see Section 1.2.3). The contact firing was performed at a peak-firing set temperature of 770°C / 770°C in the last 2 firing zones at a belt speed of 2000 mm/min.

Subsequently, we open the contact points at the rear by laser ablation of the dielectric stack using a *LUMERA LASER Super Rapid* picosecond laser. For the ablation of the dielectric a pulse energy of 5 μJ is applied. Point contacts of 20 μm in diameter with a pitch of $\sim$ 50 μm are opened. The point contact openings are arranged along lines at a distance of 1 mm to each other. Finally, we evaporate 2.5 μm of Al on the rear side of the cell using a-n *ATON 500* inline metalization system from *Applied Materials*.

4.4.2. Solar cell results

Table 4.8 shows the one-sun performance of our best solar cell with a screen-printed and passivated Al-p^+ rear emitter and a screen-printed Ag front grid measured under standard testing conditions (AM1.5G spectrum, 100 mW/cm^2, 25°C). The Table shows two measurements of the same cell measured with and without a mask.

TABLE 4.8.
PARAMETERS OF OUR BEST INDUSTRIAL-TYPE ALU$^+$ SOLAR CELL MEASURED WITH AND WITHOUT MASK. (STANDARD TESTING CONDITIONS).

Cell area	V_{oc} [mV]	J_{sc} [mA/cm^2]	FF [%]	η [%]
100 cm^2 (no mask)	643	33.7	77.0	16.2
86.8 cm^2 (mask)	640	36.0	76.6	17.6

The high open-circuit voltage of V_{oc} = 640 mV (643 mV without mask) indicates a very effective passivation of the p^{+}-emitter by the Al_2O_3/SiN_x stack. We measure a short circuit-current density of J_{sc} = 36.0 mA/cm^2 and a fill factor of only FF = 76.6%. These solar cell parameters result in a energy conversion effciency of η = 17.6%.

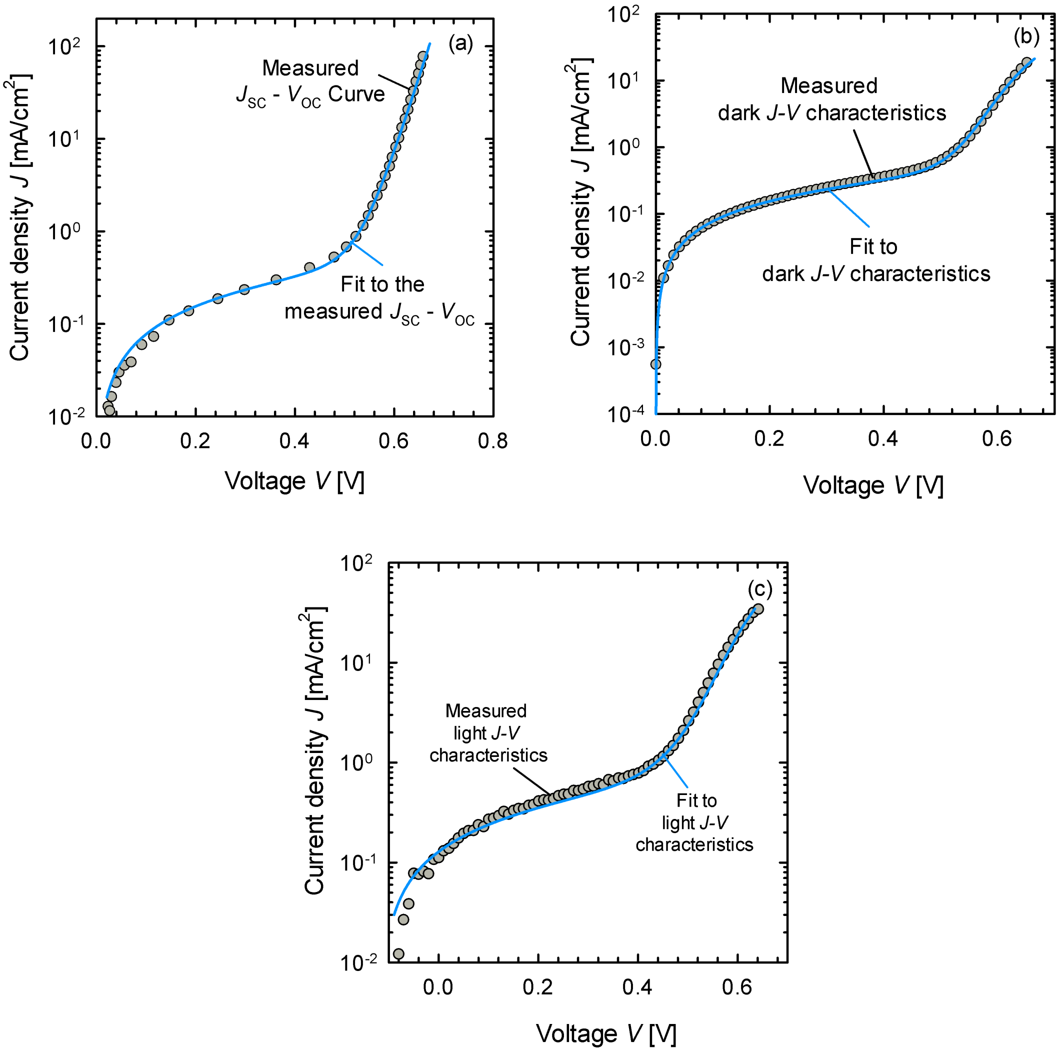

Figure 4.19.: *Measured and calculated current-voltage characteristics: (a)* J_{sc}-V_{oc}*, (b) dark J-V, and (c) illuminated J-V curves.*

The parameters of the 2-diode model [78, 124, 125] R_{shunt} (shunt resistance), R_{series} (series resistance) and the J_{01} (saturation current density of the first diode), J_{02} (saturation current density of the second diode) have been extracted from least-square fits of measured current-voltage characteristics of an illuminated J-V, a dark J-V, and a J_{sc}-V_{oc} curve. Furthermore, the pseudo fill factor FF_0 is obtained from the J_{sc} - V_{oc} curve. The fits were performed by using the ISFH-developed software SCAN (Solar Cell ANalysis) [126].

Figure 4.19 shows the measured and fitted (a) J_{sc}-V_{oc}, (b) dark J-V, and (c) illuminated J-V curves. The extracted fit parameters of the 2-diode model are shown in Table 4.9. For the analyzed solar cell a saturation current density J_{01} of 460 fA/cm^2 is determined which is consistent with the high measured V_{oc} of 643 mV, which corresponds to a $J_0 = f(J_{sc}, V_{oc}) = 540$ fA/cm^2 (Eq. 3.5). The current density of second diode is determined to be J_{02} = 5.9 nA/cm^2 which is in the range of the industrial-type solar cell with non-passivated Al-p^+ emitter at the rear introduced in Section 4.3. The high series resistance of R_{serial} = 1.70 Ωcm^2 has a negative impact on the fill factor. This is also supported by the high pseudo fill factor FF_0 = 82.9% and the relativeley high R_{shunt} value of 1.7 kΩcm^2. The high series resistance of the solar cell is attributed to a high contact resistance of the Ag grid to the FSF due to non-optimized firing conditions.

TABLE 4.9.
FIT PARAMETERS OF THE MEASURED SOLAR CELL CHARACTERISTICS SHOWN IN FIGURE 4.19.

Cell area	J_{01} [fA/cm^2]	J_{02} [nA/cm^2]	R_{shunt} [kΩcm^2]	R_{serial} [Ωcm^2]	FF_0 [%]
86.8 cm^2 (mask)	460	5.9	1.29	1.70	82.6

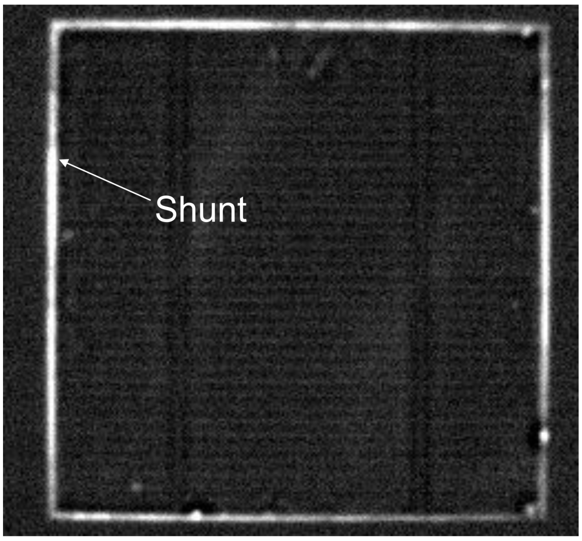

Figure 4.20.: *Illuminated Lock-in Thermography (ILIT) image of an industrial-type ALU$^+$ solar cell showing an increased signal at the edge of the solar cell.*

Figure 4.20 shows an illuminated lock-in thermography (ILIT) image [127, 128], where an increased camera signal along the edge of the solar cell can be observed. In Section 4.3, it was shown that an edge of ~1.5 mm around the entire cell remains completely dark in the EL image.

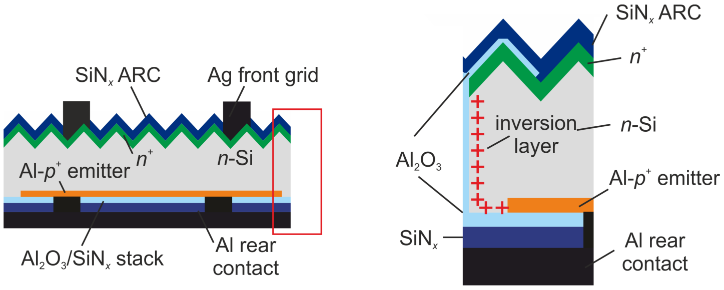

Figure 4.21.: *Schematic of a solar cell edge demonstrating the parasitic shunting of the industrial-type ALU$^+$ solar cell which leads to a decrease in J_{sc}.*

In that particular case, the unpassivated area of the solar cell led to enhanced recombination resulting a decreased EL signal.

In the industrial-type ALU$^+$ solar cell the screen-printed region and hance the emitter at the rear is also not covering the entire cell area, however, this area is passivated with an Al_2O_3/SiN_x stack, thus, enhanced recombination in this region is not expected. As atomic layer deposition was used for the Al_2O_3 layer, which is a highly conformal deposition technique, the Al_2O_3 deposits not only on the rear surface, but also on the edges and typically about 0.5 - 1.0 mm on the front side of the wafer. This is schematically illustrated in Figure 4.21. As the Al_2O_3 relies on the field effect passivation provided by the fixed negative charges in the film, which are in the range from $Q_f = -1.3 \times 10^{13}$ cm^{-2} to $Q_f = -4 \times 10^{12}$ cm^{-2} [129–131], one very likely explanation for the increased ILIT signal is parasitic shunting between the inversion layer underneath the passivation layer and the front contact, which leads to a parasitic current loss at these positions and so to a decreased J_{sc}. Thus, the most probable reason for the low J_{sc} value of only 33.7 mA/cm^2 when measured without the mask is parasitic shunting [132] along the edge of the entire solar cell.

The still moderate J_{sc} of 36 mA/cm^2 when measured with mask (excluding parasitic shunting at the edges) is attributed to shadowing due to the non-optimized Ag front grid. On this solar cell 7.8% (finger width of 125 μm) of the incoming sunlight are reflected by the front grid and thus it can not contribute to the total J_{sc}. An optimized front grid with a typical finger width of $\sim$ 90 μm would result in a shadowing of only 5.7% and thus in an increased short-circuit current density $J_{\mathrm{sc}} = 36.8$ mA/cm^2. Combining this increased J_{sc} with the measured V_{oc} and FF of Table 4.8 would result in an energy conversion eficiency of $\eta = 18.2$ % for our industrial-type ALU$^+$ solar cell.

4.5. Chapter summary

We have successfully demonstrated the implementation of screen-printed and surface-passivated Al-p^+ emitters into laboratory-type high-efficiency n-type Si solar cells and into a novel back-junction back-contact n-type solar cell. Furthermore, an all-screen-printed n-type industrial-type solar cell was fabricated and analyzed.

Laboratory-type solar cells fabricated on n-type Cz-Si featuring an a-Si as well as an Al_2O_3/SiN_x passivated Al-p^+ rear emitter showed record-high open-circuit voltage of 649 mV proving the high passivation quality of both passivation layers on Al-p^+ emitters. An independently confirmed conversion efficiency of 20.0% was demonstrated, which is a record efficiency for n-type silicon solar cells with an a-Si passivated Al-p^+ emitter.

Solar cells passivated with Al_2O_3/SiN_x stacks showed a slightly reduced conversion efficiency of 19.8% which was attributed to fill factor problems. However, the measured open-circuit voltage is as high as 649 mV, proving the excellent passivation quality of the Al_2O_3/SiN_x stack as it has already been predicted from saturation current density measurments in Chapter 3.

A conversion efficiency of 19.0% was experimentally realized on a novel back-junction back-contact n-type solar cell featuring an Al_2O_3 passivated Al-p^+ rear emitter. From two-dimensional numerical device simulations a realistic efficiency potential of 21.6% was calculated using industrially applicable surface passivation schemes.

An independently confirmed conversion efficiency of 18.0% was realized for an industrial-type n-type large area solar cell with a screen-printed Al-p^+ rear emitter and a selective front surface field and screen-printed contacts at the front and rear.

Finally, a large-area industrial-type ALU$^+$ solar cell with screen-printed and passivated Al-p^+ rear emitter and screen-printed Ag front contacts was realized showing open-circuit voltage of 643 mV proving the effective passivation of the rear emitter surface. With this solar cell a conversion efficiency of 17.6% has been achieved.

5. Summary

We have demonstrated that screen-printed Al-p^+ emitters are of a much higher electrical quality than has been expected in the literature and that they can serve as an alternative to e.g. high-temperature boron-diffused p^+ emitters. However, the use of screen-printed Al-p^+ emitters in high-efficiency solar cell structures demands for surface passivation and thus for increased process complexity compared to the simple screen-printing process as it is used for the BSF formation in industrial-type p-Si solar cells.

The morphology and the electrical properties of the screen-printed Al-p^+ emitter were investigated in this work. It was shown that the concentration peak in measured doping profiles of Al-p^+ regions originates from aluminum-rich Si surface structures which remain on the surface after the Al-paste has been etched off. Furthermore, it was demonstrated that the bulk of the surface structures and, more importantly, of the Al-p^+ emitter bulk is completely free from any crystallographic defects and thus epitaxially grown from the liquid phase. The carrier lifetime in the Al-p^+ bulk was determined for the first time to be 130 ns instead of the 100 ps which had been determined previously by extrapolating lifetime measurements on Al-doped Cz-Si wafers. From carrier lifetime measurements of samples with Al-p^+ regions it was concluded that an Al-O-related defect complex forms at elevated temperatures, degrading the lifetime of the Al-p^+ region. The activation energy for the formation of the Al-O complex was determined to be $E_a = (0.25 \pm 0.08)$ eV.

For the first time, a screen-printed Al-p^+ region was surface-passivated. An excellent surface passivation quality was achieved using ALD-Al_2O_3, Al_2O_3/SiN_x stacks and PECVD a-Si, where saturation current densities J_0 ranging from 160 - 248 fA/cm^2 were measured. As-deposited PECVD-SiN_x layers showed no passivation. However, firing at 900°C activated the SiN_x and saturation current densities of 307 fA/cm^2 were achieved. Thermally grown SiO_2 led to a lifetime degradation in the Al-p^+ emitter for growth temperatures above 900°C. Silicon dioxide grown at lower temperatures ($\leq$ 850°C) provided an excellent passivation quality, where a J_0 value of 200 fA/cm^2 was achieved using a SiO_2/SiN_x stack.

Finally, the screen-printed and passivated Al-p^+ emitter was successfully applied to a laboratory-type n^+np^+ solar cell. An independently confirmed record-high efficiency of 20.0 % was achieved for a front and rear-contacted solar cell, the ALU$^+$ cell, fabricated on n-type Cz-Si material (4 cm^2 cell size). The implementation of the screen-printed and passivated emitter to a back-junction back-contact cell structure using n-type Cz-Si material was realized. Using this novel approach an efficiency of 19.0% (4 cm^2) was experimentally realized. 2-dimensional numerical simulations revealed that this structure has a realistic efficiency potential of 21.6%. We have developed an all-screen-printed industrial-type *n*-type solar cell featuring a full-area metallized Al-p^+ rear emitter and a selective front surface field. This industrial-type solar cell achieved an independently confirmed conversion efficiency of 18.0% on a 100 cm^2 solar cell area. Finally, our ALU$^+$ cell concept was successfully transfered to a large-area industrial-type ALU$^+$ solar cell, where we achieved an efficiency of 17.6% on a cell area of 86.8 cm^2. Due to the high achieved open-circuit voltage of 643 mV for this cell type, we conclude that efficiencies up to 20% are acievable with the ALU$^+$ cell concept introduced in this work.

The results of this work suggest that the quality of a screen-printed Al-p^+ emitter and the efficiency potential of screen-printed solar cells on *n*-type silicon have been strongly underestimated in the past and that the screen-printed Al-p^+ emitter is a competitive alternative to the high-temperature boron diffusion.

A. Accurate extraction of doping profiles from ECV measuremnts

The common doping profile measurement methods are spreading resistance (SR), secondary ion mass spectroscopy (SIMS) and electrochemical capacitance-voltage (ECV). The SR method is simple and cheap but needs mechanical pretreatment of the sample and has restrictions in depth resolution [133, 134]. The SIMS method is in comparison to the other methods expensive and provides only the chemical doping concentration, which is e.g. in the case of a phosphorus diffusion not very helpful for the use in simulations of electrical properties of semiconductor devices. In contrast, the ECV method provides only the electrically active dopants and has a depth resolution in the sub-nm range, which makes it a very powerful measurement tool for the use in device simulations and for device optimization in the PV industry [135]. However, today the ECV method, which is well known in the field of microelectronics, is still quite uncommon in photovoltaics, due to its limited accuracy. In this Section, it is demonstrated that highly accurate results can be obtained from ECV measurements by applying relatively simple correction procedures.

A.1. Doping profile characterization by ECV measurements

The ECV technique is based on the determination of the space-charge-region (SCR) capacitance of a semiconductor-electrolyte contact, which basically is similar to the Schottky-contact (semiconductor-metal contact). Details to the models describing the semiconductor-electrolyte interface, such as the Helmholz model (the Helmholtz model considers that a layer of ions is located at the surface of the electrode and compensates its charge), Gouy-Chapman model (the Gouy-Chapman model assumes that ions are mobile due to thermal fluctuations and therefore ions form a diffuse structure called Gouy layer) and the Stern model (combination of both, Helmholtz model and Gouy-Chapman model.) can be found in the references [136–141].

The depth profiling is achieved by electrochemically etching the semiconductor between the capacitance measurements. Describing the electrolyte-semiconductor Schottky contact by the depletion approximation for a homogeneously doped semiconductor the following assumptions need to be taken into account:

- The SCR is free of any charges

- The edge of the SCR in the semiconductor is neutral
- The interface between SCR and the neutral zone is abrupt

Using this approximations and by describing the SCR as a parallel plate capacitor the measured capacitance C depends on the applied voltage V and thus $1/C^2$ is given as a function of the carrier concentration N by the so called Schottky-Mott equation:

$$\frac{1}{C^2} = \frac{-2}{e\varepsilon_0\varepsilon_\mathrm{R}A^2N}(V - V_\mathrm{th}). \tag{A.1}$$

Thus the carrier concentration N is inversely proportional to the slope of $1/C^2$(V):

$$N = \frac{-2}{e\varepsilon_0\varepsilon_\mathrm{R}A^2N\frac{\mathrm{d}(1/C^2)}{\mathrm{d}V}}. \tag{A.2}$$

where e is the elementary charge, ε_0 the vacuum dielectricity, ε_R the dielectric constant of the semiconductor material, V_th the flat-band potential, and A the electrolyte-semiconductor contact area. The flat-band potential V_th is equal to the external voltage that must be applied for a flat energy band in the semiconductor, which simply means the depletion width is zero. The depth profile is achieved by etching off the surface between the capacitance measurements. This is done electrochemically by anodic etching of the silicon in an 0.1 molal NH_4F-electrolyte-solution.

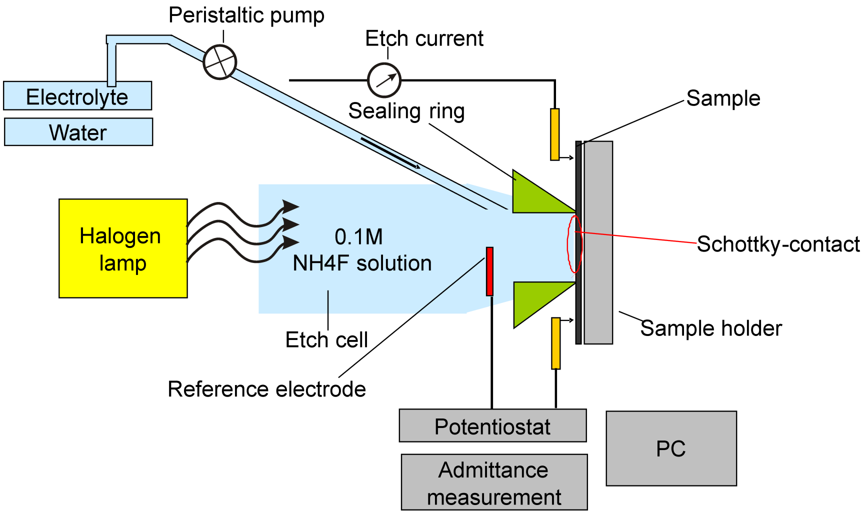

Figure A.1.: *Schematic of the WEP CVP21 ECV measurement equipment.*

A *WEP CVP21* ECV-profiler as depicted schematically in Figure A.1 has been used for the ECV-measurements. In order to create the Schottky contact the sample is contacted to the NH_4F-electrolyte-solution with aid of a sealing ring. This sealing ring has a defined area of $0.1\mathrm{cm}^2$ which has a large impact on the doping concentration N (see Eq.A.2) and thus the knowledge of the sealing ring area is of high importance. This will be the topic of the following Section.

A.2. Experimental details

In order to carry out ECV doping-profile measurements and to compare them to SIMS measurements and simulations diffused samples are prepared. For the investigation of hole concentration profiles boron-diffused (100) oriented *n*-type FZ-Si wafers are used. The resulting p^+ diffusions have sheet resistances of 54 $\Omega/\square$ and 91 $\Omega/\square$. For the investigation of electron concentration profiles $POCl_3$ diffused *p*-type (100)-oriented textured and flat FZ-Si wafers with resulting sheet resistances of 38 $\Omega/\square$ and 95 $\Omega/\square$ are used. A *Centrotherm Dotiersystheme 2000HT180-4* quartz tube furnace has been used for the P-diffusion processes. The sheet resistances were measured using a four-point probe. The electrically active doping profiles from the boron- and phosphorus-doped samples are subsequently measured by the ECV technique using the *WEP CVP21* profiler (see Section A.1) with a 0.1M solution of NH_4F. Good ohmic contact to the silicon was achieved using an Indium-Gallium alloy. For comparison, the dopant distributions of the boron-diffused samples are measured by means of Time-of-Flight Secondary Ion Mass Spectroscopy (TOF SIMS) using an *IONOF TOFSIMS IV* instrument in the depth profiling mode with Bi^+ analysis ions at 25 keV. Finally, we recalculate the measured doping profiles with exact area parameters obtained from optical microscopy images taken on the ECV-measured samples.

A.3. Exemplary results

In commercially available automated measurement equipment, the ECV doping concentration is usually calculated from the electrochemical measurement assuming a fixed etch area, which is defined by the sealing ring geometry of the measurement equipment. In previous publications, it has been discussed that the etch crater wall is one major source of error in ECV measurements, whereas the Si-electrolyte contact area has always been assumed to be fixed since it is defined by the sealing ring geometry [64].

Figure A.2 shows a comparison of ECV doping depth profiles of homogeneously doped low-resistivity *n*-type FZ-Si wafers measured with different measurement systems. It can be seen that the *WEP CVP21* profiler shows a constant carrier concentration to a depth of 20 μm. In comparison, the *Accent PN4300PC* shows a significant deviation of about 20% at this depth. A possible cause for this strong deviation is probaly a leakage of the sealing ring. The area contribution of the etch crater walls at an etch depth of 10 μm using a sealing ring of 3.7 mm in diameter is in the range of 1% and thus it is negligible especially for phosphorus and boron doping profile measurements. From optical microscopy analysis of the etch crater geometry directly after the ECV measurement with our equipment we found the Si-electrolyte contact area to be always larger by a factor of 1.16 - 1.18 than it is assumed for the calculation of the carrier concentration. This factor may be different with other commercially available ECV measurement equipment but is very like to be present. As a result of this Si-electrolyte contact area underestimation by

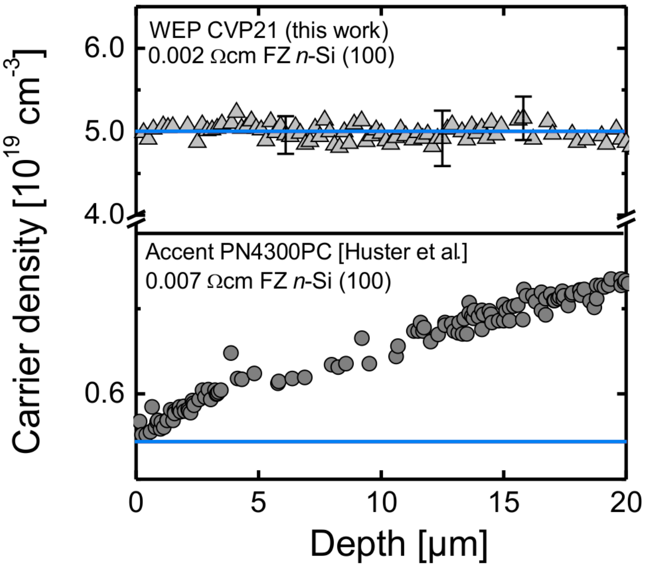

Figure A.2.: *Comparison of ECV measurements on low-resistivity Si wafers using different measurement systems.*

the measurement system the carrier concentration is always overestimated in accordance with the Schottky-Mott equation (Eq. A.2).

Boron diffusion

Figure A.3 shows doping profiles measured on boron-diffused samples. Their sheet resistances are 91 Ω/□ [Figure A.3 (a)] or 54 Ω/□ [Figure A.3 (b)] as measured by the 4-pp technique. Using Masetti´s carrier mobility model [142] the sheet resistance of the original ECV doping profile is calculated: it is about 30% below that of the values measured by the 4-pp method. The sheet resistance obtained from the SIMS profile agrees with the 4-pp result within less than 10%. After the ECV doping profile has been recalculated with the 18% larger externally determined Si-electrolyte contact area, the resulting sheet resistance of 97 Ω/□ for the sample in Figure A.3 (a) and 55 Ω/□ for the sample in Figure A.3 (b) respectively, is in the range of the 4-pp measurement within less than 10%. Moreover, the corrected carrier distribution fits very well to the SIMS measurement as shown in Fig. A.3 (a) and (b).

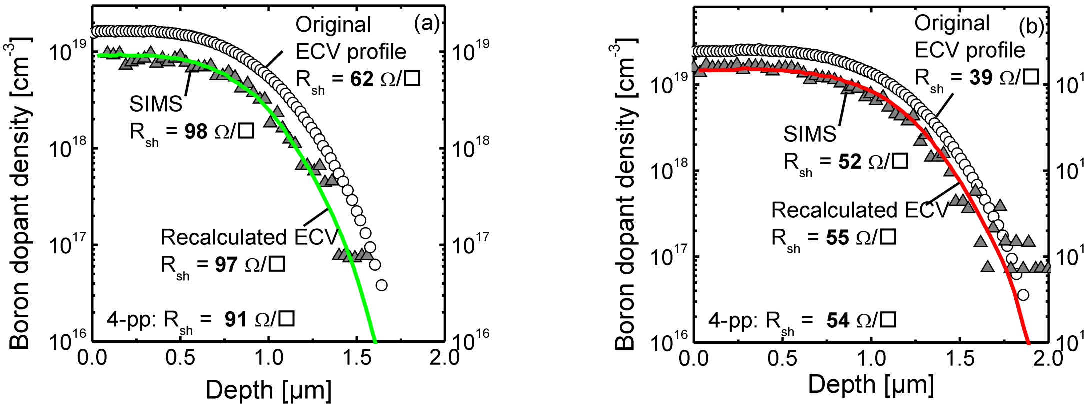

Figure A.3.: *Boron diffused samples with a sheet resistance of (a) 91 Ω/□ and (b) 54 Ω/□ as measured by the four-point probe method.*

A.3.1. Phosphorus diffusion

Figure A.4 shows doping profile measurements of phosphorus-diffused samples with sheet resistances of 96 Ω/□ [Figure A.4 (a)] and 40 Ω/□ [Figure A.4 (b)] obtained from 4-pp measurements.

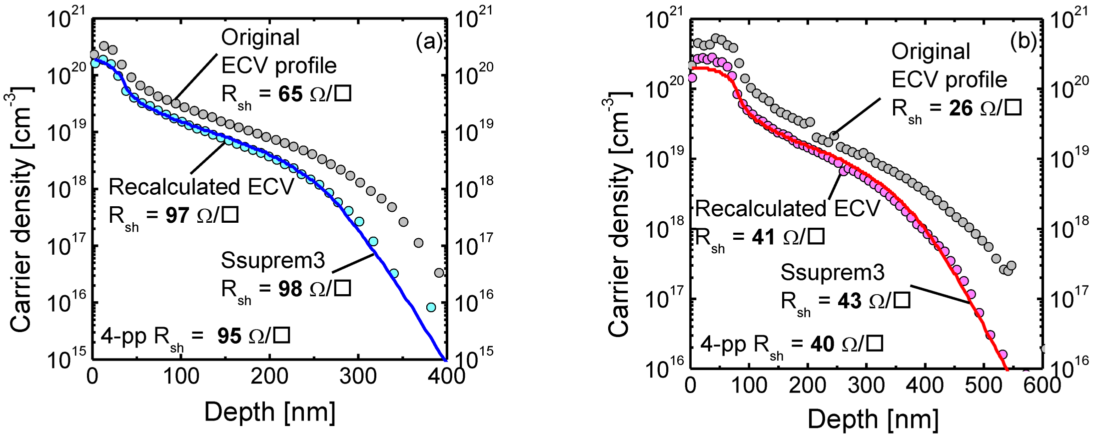

Figure A.4.: *Phosphorus-diffused samples with a sheet resistance of (a) 95 Ω/□ and (b) 40 Ω/□ as measured by the four-point probe method.*

The original ECV measurement again overestimates the 4-pp sheet resistance. The sheet resistance values from the ECV profile are again about 30% below that of the 4-pp measurement. This is not surprising since the same equipment has been used for the profile measurement, thus the Si-electrolyte contact area increased by the same amount (18%) resulting in an overestimated carrier concentration and, consequently, in a lower sheet resistance. Additionally, Ssuprem3 doping profile simulations are included in Fig. A.4, where the diffusion parameters of the measured samples have been used for the calculation. The simulations show an excellent agreement with the corrected ECV doping profiles, proving that the parameterization method works also well for the carrier distribution, not only for the sheet resistance.

A.3.2. Textured surface

However, the presented results have been obtained on flat samples. In order to apply this method to a non-flat sample, e.g., a random-pyramid-textured sample, the surface area enlargement due to the texture needs to be taken into account for the evaluation of the measured ECV profile. For a single-crystalline Si wafer textured with random pyramids, the average surface area enlargement is 73%. Figure A.5 shows ECV profiles of the same phosphorus diffusion on a textured sample and on a flat reference sample.

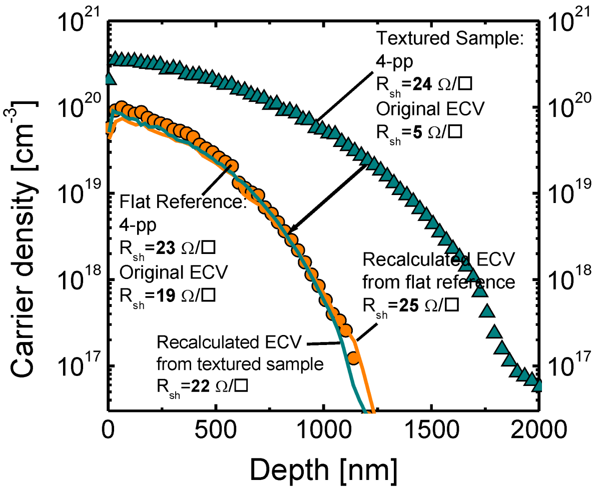

Figure A.5.: *ECV doping profiles of phosphorus-diffused regions measured on flat reference samples and on random-pyramid-textured samples. The sheet resistances of both profiles match within 10% after recalculation using the corresponding Si-electrolyte contact area.*

It is quite clear that the original doping profile of the textured sample is completely erroneous due to the enlarged Si-electrolyte contact area and can not be used for device optimization nor for device simulation. In this case, the difference in sheet resistance between the ECV value of 5 Ω/□ and the 4-pp value of 24 Ω/□ is huge, whereas, as expected, the sheet resistance obtained from the 4-pp measurement for the textured sample and for the flat reference sample is nearly the same. After the profile of the reference sample has been recalculated using the enlarged contact area originating from the sealing ring a sheet resistance of 22 Ω/□ was determined, which is close to the 4-pp value. In order to extract the true doping profile of the textured sample, the enlargement factor is 1.18 × 1.73 = 2.04. As a result the sheet resistance determined from the recalculated ECV doping profile is about 25 Ω/□ and thus is in the range of the 4-pp value of 23 Ω/□ within 10%.

A.3.3. Application

The surface recombination parameter of minority carriers, S_{n0} or S_{p0}, is a measure for the quality of the surface passivation within the SRH recombination theory. At dopant-diffused surfaces this parameter is experimentally inaccessible and thus is numerically calculated from the measured current-density J_{0e} of the diffused emitter. The procedure to extract S_{n0} is as follows. The J_{0e} values are obtained from QSSPC measurements [82]. Then, J_{0e} is calculated as a function of the surface recombination velocity S_{n0}. We use the device simulator SENTAURUS [75] and the physical models described in Refs. [74] and [83]. The surface recombination velocity parameter is the only free parameter in the model; other model parameters for Auger recombination, band gap narrowing, carrier mobilities etc. were independently determined and do not vary among experiments.

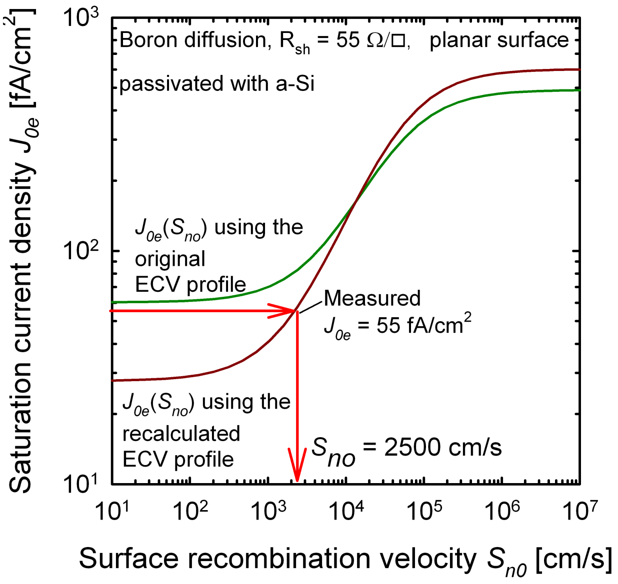

Figure A.6.: *Simulated saturation current density J_{0e} as a function of the surface recombination velocity parameter S_{n0} using the measured ECV profile before and after the correction procedure of a boron diffused region with a measured sheet resistance of R_{sh} = 55 Ω/□.*

Figure A.6 shows that the simulated S_{n0} or S_{p0} values depend sensitively on the dopant profile: without the etch-area correction, too high dopant densities are measured, leading to an overestimation of Auger losses in the model. The simulation where the original doping profile is used as input parameter shows a minimal J_{0e} of 60 fA/cm^2 at S_{n0} = 0 cm/s, which is higher than the measured J_{0e} of 55 fA/cm^2. Using the recalculated doping profile a realistic reproduction of the emitter saturation current density J_{0e} is achieved where the measured J_{0e} = 55 fA/cm^2 corresponds to S_{n0} = 2500 cm/s. An overestimated ECV doping profile generally leads to an overestimated J_{0e}.

A.4. Conclusions

A simple correction procedure for ECV doping profile measurements has been introduced. An excellent agreement between the sheet resistance measured with the 4-point-probe method and that determined from the corrected ECV doping profiles (accuracy better ±10%) was found. It has been shown that the accuracy of ECV measurements is mainly determined by the precise measurement of the area of the electrolyte-Si contact. The corrected ECV doping profiles of the boron-diffused samples have been verified with secondary ion mass spectroscopy (SIMS) and were also found to be in excellent agreement. In conclusion, it is highly recommended to measure the external etch area and crater depth and to recalculate the measured ECV doping profile using this data in order to obtain accurate doping profiles e.g. suitable for advanced device simulations.

References

[1] D. M. De Ceuster, P. Cousins, D. Rose, D. Vicente, P. Tipones, and W. Mulligan, Low cost, high volume production of >22% efficiency silicon solar cells, *Proceedings of the 22nd European Photovoltaics Specialists Conference, Milan, Italy*, p. 816 (2007).

[2] P. J. Cousins, D. D. Smith, H.-C. Luan, J. Manning, T. D. Dennis, A. Waldhauer, K. E. Wilson, G. Harley, and W. P. Mulligan, Generation 3: Improved performance at lower costs, *Proceedings of the 36th IEEE Photovoltaic Specialists Conference, Hawaii, USA* (2010).

[3] A. Terakawa, T. Asaumi, S. Kobayashi, Y. Tsunomura, T. Yagiura, Y. Yoshimine M. Taguchi, H. Sakata, E. Maruyama, and M. Tanaka, High effciency hit solar cells and the effects of open circuit voltage on temperature coeffcients, *Proceedings of the 15th International Photovoltaic Science and Engineering Conference Shanghai, China*, p. 661 (2005).

[4] J. Schmidt, A. G. Aberle, and R. Hezel, Investigation of carrier lifetime instabilities in Cz-grown silicon, *Proceedings of the 26th IEEE Photovoltaic Specialists Conference, Anaheim, USA*, p. 13 (1997).

[5] A. Cuevas, M. J. Kerr, C. Samundsett, F. Ferrazza, and G. Coletti, Millisecond minority carrier lifetimes in n-type multicrystalline silicon, *Appl. Phys. Lett.* **81**, 4952 (2002).

[6] J. Schmidt, K. Bothe, R. Bock, C. Schmiga, R. Krain, and R. Brendel, N-type silicon – the better material choice for industrial high-efficiency solar cells?, *Proceedings of the 22ed European Photovoltaic Solar Energy Conference, Milan, Italy*, p. 998 (2007).

[7] J. Schmidt and K. Bothe, Structure and transformation of the metastable boron- and oxygen-related defect center in crystalline silicon, *Phys. Rev. B* **69**, 024107 (2004).

[8] H. Fischer and W. Pschunder, Investigation of photon and thermal induced changes in silicon solar cells, *Proceedings of the 10th IEEE Photovoltaic Specialists Conference, Palo Alto, USA*, p. 404 (1973).

[9] J. Knobloch, S. W. Glunz, V. Henninger, W. Warta, W. Wettling, F. Schomann, W. Schmidt, A. Endrös, and K. A. Münzer, 21% efficient solar cells processed from

Czochralski-grown silicon, *Proceedings of the 13th European Photovoltaic Solar Energy Conference, Nice, France*, p. 9 (1995).

[10] K. Bothe, R. Sinton, and J. Schmidt, Fundamental boron-oxygen-related carrier lifetime limit in mono- and multicrystalline silicon, *Prog. Photovolt: Res. Appl.* **13**, 287 (2005).

[11] K. Bothe and J. Schmidt, Fast-forming boron-oxygen-related recombination center in crystalline silicon, *Appl. Phys. Lett.* **87**, 262108 (2005).

[12] S. Chandrasekhar, On the inhibition of convection by a magnetic field, *Philos. Mag.* **43(7)**, 501–532 (1952).

[13] A. F. Witt, C. J. Herman, and H. C. Gatos, Czochralski-type crystal growth in transverse magnetic fields, *J. Mat. Sci.* **5**, 822–824 (1970).

[14] T. Suzuki N. Isawa, Y. Okubo, and K. Hoshi, Cz silicon crystals grown in a transverse magnetic field, *H.R. Huff, editor, Semiconductor silicon 1981* 90–100 (1981).

[15] A. Herguth, G. Schubert, M. Kaes, and G. Hahn, Investigations on the long time behavior of the metastable boron–oxygen complex in crystalline silicon, *Prog. Photovolt: Res. Appl.* **16**, 135 (2008).

[16] B. Lim, K. Bothe, and J. Schmidt, Deactivation of the boron–oxygen recombination center in silicon by illumination at elevated temperature, *phys. stat. sol. (RRL)* **2, No. 3**, 93 (2008).

[17] F. A. Trumbore, Solid solubilities of impurity elements in germanium and silicon., *Bell Syst. Tech. J.* **39**, 205 (1960).

[18] S. Taira, Y. Yoshimine, T. Baba, M. Taguchi, and H. Kanno, Our approaches for achieving hit solar cells with more than 23% efficiency, *Proceedings of the 22ed European Photovoltaic Solar Energy Conference, Milan, Italy* (2007).

[19] J. Benick, B. Hoex, M. C. M. van de Sanden, W. M. M. Kessels, O. Schultz, and S. W. Glunz, High efficiency n-type Si solar cells on Al_2O_3-passivated boron emitters, *Appl. Phys. Lettl* **92**, 253504 (2008).

[20] V. Mertens, S. Bordihn, Y. Larionova, N.-P. Harder, and R. Brendel, The buried emitter solar cell concept: Interdigitated back-junction strucutre with virtually 100% emitter coverage of the cell area, *Proceedings of the 24th European Photovoltaic Solar Energy Conference, Hamburg, Germany*, p. 934 (2009).

[21] B. Lim, K. Bothe, and J. Schmidt, Impact of oxygen on the permanent deactivation of boron–oxygen-related recombination centers in crystalline silicon, *J. Appl. Phys.* **107**, 123707 (2010).

[22] S. M. Sze, *Semiconductor Devices, Physics and Technology*, John Wiley & Sons, Inc. (1985).

[23] S. K. Ghandi, *VLSI Fabrication Principles*, New York: Wiley (1994).

[24] P. J. Cousins and J. E. Cotter, The influence of diffusion-induced dislocations on high efficiency silicon solar cells, *IEEE Technol. Electron. Device* **53**, 457–64 (2006).

[25] U. Pignatel and G. Queirolo, Further insight on boron diffusion in silicon obtained with auger electron spectroscopy, *Thin Solid Films* **67**, 233 (1979).

[26] E. Dominguez, E. Lora-Tamayo, and B. Blanchard, Analytic study of the Si-B phase when B_2O_3 is diffused in Si, *J. Electrochemical .Soc.: SOLID STATE SCIENCE AND TECHNOLOGY* **125**, 1521 (1978).

[27] D. M. Brown and P. R. Kennicott, Glass source B diffusion in Si and SiO_2, *J. Electrochemical .Soc.: SOLID STATE SCIENCE AND TECHNOLOGY* **118**, 293 (1971).

[28] M. A. Kessler, T. Ohrdes, B. Wolpensinger, and N.-P. Harder, Charge carrier lifetime degradation in Cz silicon through the formation of a boron-rich layer during BBr_3 diffusion processes, *Semicond. Sci. Technol.* **25**, 055001 (2010).

[29] J. Zhao and A. Wang, High efficiency rear emitter PERT cells on Cz and FZ n-type silicon substrates, *Proceedings of the 4th World Conference on Photovoltaic Energy Conversion, Hawaii, USA*, p. 996 (2006).

[30] P. J. Cousins and J. E. Cotter, Misfit dislocations generated during non-ideal boron and phosphorus diffusion and their effect on high-efficiency silicon solar cells, *Proceedings of the 31st IEEE Photovoltaic Specialists Conference, Orlando, USA*, p. 1047 (2005).

[31] J.-H. Guo, B. S. Tajahjono, and J. E. Cotter, 19.2 % efficiency n-type laser-grooved silicon solar cells, *Proceedings of the 31st IEEE Photovoltaic Specialists Conference, Lake Buena Vista, USA*, p. 983 (2005).

[32] J. Zhao and A. Wang, *Proceedings of the 20th European Photovoltaic Solar Energy Conference, Barcelona, Spain*, p. 806 (2005).

[33] A. Froitzheim, K. A. Münzer, K.-H. Eisenrith, R. Tölle, and M. G. Winstel, N-type silicon solar cells based on industrial technology, *Proceedings of the 20th European Photovoltaic Solar Energy Conference, Barcelona, Spain*, p. 594 (2005).

[34] V. D. Mihailetchi, Y. Komatsu, and L. J. Geerligs, Nitric acid pretreatment for the passivation of boron emitters for n-type base silicon solar cells, *Appl. Phys. Lett.* **92**, 063510 (2008).

[35] T. Buck, R. Kopecek, J. Libal, A. Herguth, K. Peter, I. Röver, K. Wambach, and B. Geerligs, Industrial screen printed n-type silicon solar cells with front boron emitter and efficiencies exceeding 17%, *Proceedings of the 21st European Photovoltaic Solar Energy Conference, Dresden, Germany*, p. 1264 (2006).

[36] M. Tanaka, M. Taguchi, T. Matsuyama, T. Sawada, S. Tsuda, S. Nakano, H. Hanafusa, and Y. Kuwano, Development of new a-Si/c-Si heterojunction solar cells: ACJ – HIT (artificially constructed junction-heterojunction with intrinsic thin-layer), *J. Appl. Phys.* **31**, 3518 (1992).

[37] M. Tucci, R. De Rosa, and F. Roca, CF_4/O_2 dry etching of textured crystalline silicon surface in a-Si:H/c-Si heterojunction for photovoltaic applications, *Solar Energy Materials and Solar Cells* **69 (2)**, 175 (2001).

[38] Y. Tsunomura, Y. Yoshimine, M. Taguchi, T. Baba, T. Kinoshita, H. Kanno, H. Sakata, E. Maruyama, and M. Tanaka, Twenty-two percent efficiency HIT solar cell, *Solar Energy Materials and Solar Cells* **93 (6-7)**, 670 (2009).

[39] T. Sawada, N. Terada, S. Tsuge, T. Baba, T. Takahama, K. Wakisaka, S. Tsuda, and S. Nakano, High-efficiency a-Si/c-Si heterojunction solar cell, *Proceedings of the 24th IEEE Photovoltaic Specialists Conference* (1994).

[40] H. Fujiwara and M. Kondo, Impact of epitaxial growth at the heterointerface of a-Si:H/c-Si solar cells, *Appl. Phys. Lett.* **90**, 13503 (2007).

[41] Sanyo. http://sanyo.com/news/2009/05/22-1.html, (2009).

[42] E. Conrad, L. Corte, K. v. Maydell, H. Angermann, C. Schubert, R. Stangl, and M. Schmidt, Development and optimization of a-Si:H/c-Si heterojunction solar cells completely processed at low temperatures, *Proceedings of the 21st European Photovoltaic Solar Energy Conference, Dresden, Germany*, p. 784 (2006).

[43] A. Descoeudres, L. Barraud, R. Bartlome, G. Choong, S. De Wolf, F. Zicarelli, and C. Ballif, The silane depletion fraction as an indicator for the amorphous/crystalline silicon interface passivation quality, *Appl. Phys. Lett* **97**, 183505 (2010).

[44] H. Fujiwara, H. Sai, and M. Kondo, Crystalline Si heterojunction solar cells with the double heterostructure of hydrogenated amorphous silicon oxide, *Jpn. J. Appl. Phys.* **48**, 064506 (2009).

[45] Q. Wang, M. R. Page, E. Iwaniczko, Y. Q. Xu, L. Roybal, R. Bauer, B. To, H. C. Yuan, A. Duda, and Y. F. Yan, Crystal silicon heterojunction solar cells by hot-wire CVD, *Proceedings of the 33rd IEEE Photovoltaic Specialists Conference San Diego, USA* (2008).

[46] J. v. Duppen, *Handbuch für den Siebdruck*, Verlag Der Siebdruck (1986).

[47] P. Hahne, *Innovative Druck- und Metallisierungsverfahren für die Solarzellentechnologie*, PhD thesis, FernUniversität in Hagen (2000).

[48] D. E. Riemer, *Ein* B*eitrag zur* U*ntersuchung der physikalischtechnischen* G*rundlagen des* S*iebdruckverfahrens*, PhD thesis, TU Berlin (1988).

[49] P. J. Holmes and R. G. Loasby, *Handbook of Thick Film Technology*, Electrochemical Publications Ltd. (1976).

[50] J. L. Murray and A. J. McAlister, *Bull. Alloy Phase Diagrams* **5** **(1)**, 74 (1984).

[51] J. D. Alamo, J. Eguren, and A. Luque, Operating limits of Al-alloyed high-low junctions for BSF solar cells, *Solid-State Electron.* **24**, 415 (1981).

[52] D. A. Clugston and P. A. Basore, PC1D version 5: 32-bit solar cell modeling on personal computers, *Proceedings of the 26th IEEE Photovoltaic Specialists Conference, Anaheim, California, USA*, 207–10 (1997).

[53] D. L. Meier, H. P. Davis, R. A. Garcia, J. Salami, A. Rohatgi, A. Ebong, and P. Doshi, Aluminum alloy back pn-junction dendritic web silicon solar cell, *Solar Energy Materials and Solar Cells* **65**, 621 (2001).

[54] A. Cuevas, C. Sammundsett, M. J. Kerr, D. H. Macdonald, H. Mäckel, and P. P. Altermatt, Back junction solar cells on n-type multicrystalline and Cz silicon wafers, *Proceedings of the 3rd World Conf. on Photovoltaic Energy Conversion, Osaka, Japan*, p. 963 (2003).

[55] S. W. Glunz, E. Schneiderlöchner, D. Kray, A Grohe, M. Hermle, H. Kampwerth, R. Preu, and G. Willeke, Laser-fired contact silicon solar cells on p- and n-substrates, *Proceedings of the 19th European Photovoltaic Solar Energy Conference, Paris, France*, p. 408 (2004).

[56] C. Schmiga, H. Nagel, and J. Schmidt, 19% effcient n-type czochralski silicon solar cells with screen-printed aluminium-alloyed rear emitter, *Prog. Photovoltaics* **14**, 533 (2006).

[57] P. Hacke, J. Moschner, S. Yamanaka, and D. L. Meier, *Proceedings of the 19th European Photovoltaic Solar Energy Conference, Paris, France*, p. 1292 (2004).

[58] T. Buck, J. Libal, S. Eisert, R. Kopecek, K. Peter, P. Fath, and K. Wambach, Low cost p^+nn^+-type back junction solar cells by screen printing technique on Cz and mc-Si material, *Proceedings of the 19th European Photovoltaic Solar Energy Conference, Paris, France* (2004).

[59] R. Kopecek, T. Buck, J. Libal, I. Röver, K. Wambach, L.J. Geerligs, P. Sánchez-Friera, J. Alonso, E. Wefringhaus, and P. Fath, Large area screen printed n-type silicon solar cells with rear aluminium emitter: Efficiencies exceeding 16%, *Proceedings of the 4th World Conference on Photovoltaic Energy Conversion, Hawaii, USA* (2006).

[60] C. Schmiga, H. Nagel, R. Bock, J. Schmidt, and R. Brendel, Advances in the manufacturing of n-type silicon solar cells with screen-printed aluminium-alloyed rear emitter, *Proceedings of the 21st European Photovoltaic Solar Energy Conference, Dresden, Germany* (2006).

[61] V.C. Mihailetchi, D.S. Sainova, L. J. Geerligs, and A. W. Weeber, 17.4% efficiency solar cells on large area thin n-type silicon with screen-printed aluminum-alloyed rear emitter, *Proceedings of the 22nd European Photovoltaic Solar Energy Conference, Milan, Italy*, p. 837 (2007).

[62] P. Lölgen and C. Leguijit, Aluminium back-surface field doping profiles with surface recombination velocities below 200 cm/s, *Proceedings of the 23th IEEE Photovoltaic Specialists Conference, Louisville, USA* (1993).

[63] P. Lölgen, W. C. Sinke, C. Leguijt, A. W. Weeber, P. F. A. Alkemade, and L. A. Verhoef, Boron doping of silicon using coalloying with aluminium, *Appl. Phys. Lett.* **65**, 2792 (1994).

[64] F. Huster and G. Schubert, *Proceedings of the 20th European Photovoltaic Solar Energy Conference, Barcelona, Spain*, p. 1462 (2005).

[65] C. P. Sealy, M. R. Castell, and P. R. Wilshaw, Mechanism for secondary electron dopant contrast in the SEM, *J. Electron Microsc.* **49**, 311 (2000).

[66] V. Meemongkolkiat, K. Nakayashiki, D. S. Kim, R. Kopecek, and Ajeet Rohatgi, Factors limiting the formation of uniform and thick Al-back surface field and its potential, *Journal of Electrochemical Society* **153**, G53–G58 (2006).

[67] S. Narasimha, A. Rohatgi, and A. W. Weeber, An optimized rapid aluminum back surface field technique for silicon solar cells, *IEEE Transactions on Electron Devices* **46**, 1363 (1999).

[68] J. A. Amick, F. J. Bottari, and J. I. Hanoka, The effect of aluminum thickness on solar cell performance, *J. Electrochem. Soc.* **141**, 1577 (2002).

[69] J. R. Davis, A. Rohatgi, R. H. Hopkins, P. D. Blais, P. Rai-Choudhury, J. R. McCormick, and H. C. Mollenkopf, Impurities in solar cells, *IEEE Trans. Electron Devices* **27**, 677 (1980).

[70] J. Schmidt, Temperature- and injection-dependent lifetime spectroscopy for the characterization of defect centers in semiconductors, *Appl. Phys. Lett.* **82**, 2178 (2003).

[71] P. Rosenits, T. Roth, S. W. Glunz, and S. Beljakowa, Determining the defect parameters of the deep aluminum-related defect center in silicon, *Appl. Phys. Lett.* **91**, 122109 (2007).

[72] J. Schmidt, M. Kerr, and P. P. Altermatt, Coulomb-enhanced auger recombination in crystalline silicon at intermediate and high-injection densities, *Appl. Phys. Lett.* **88**, 1494 (2000).

[73] T. Lauinger, J. Schmidt, A. G. Aberle, and R. Hezel, Record low surface recombination velocities on 1 Ohmcm p-silicon using remote plasma silicon nitride passivation, *Appl. Phys. Lett.* **68**, 1232 (1996).

[74] P. P. Altermatt, H. Plagwitz, R. Bock, J. Schmidt, R. Brendel, M. J. Kerr, and A. Cuevas, The surface recombination velocity at boron-doped emitters: comperison between various passivation techniques, *Proceedings of the 21st European Photovoltaic Solar Energy Conference, Dresden, Germany* (2006).

[75] CA SENTAURUS, Synopsys Inc. Mountain View. www.synopsys.com/products/tcad/tcad.html, ().

[76] R. A. Sinton and A. Cuevas, Contactless determination of current-voltage characteristics and minotity cearrier lifetimes in semiconductors from quasi-steady state photoconductance data, *Appl. Phys. Lett.* **69**, 2510 (1996).

[77] D. T. Stevenson and R. J. Keyes, Measurement of carrier lifetimes in germanium and silicon, *J. Appl. Phys.* **26(2)**, 190 (1955).

[78] S. M. Sze, *Physics of semiconductor devices*, John Wiley & Sons, Second Edition, ISBN: 0471056618 (1981).

[79] R. Brendel, Note on the interpretation of injection-level-dependent surface recombination velocities, *Applied Physics A* **60 (5)**, 523 (1995).

[80] A. G. Aberle, J. Schmidt, and R. Brendel, On the data analysis of light-biased photoconductance decay measurements, *J. Appl. Phys.* **79 (3)**, 1491 (1996).

[81] J. Schmidt, Measurement of differential and actual recombination parameters on crystalline silicon wafers, *IEEE Trans. Electron Devices* **46 (10)**, 2018 (1999).

[82] D. E. Kane and R. M. Swanson, Measurment of the emitter saturation current by a contactless photoconductivity decay method, *Proceedings of the 18th IEEE Photovoltaic Specialists Conference*, p. 578 (1985).

[83] P. P. Altermatt, J. O. Schumacher, A. Cuevas, M. J. Kerr, S. W. Glunz, R. R. King, G. Heiser, and A. Schenk, Numerical modeling of highly doped Si:P emitters based on fermi-dirac statistics and self-consistent material parameters, *J. Appl. Phys.* **92**, 3187 (2002).

[84] P. P. Altermatt, S. Steingrube, Y. Yang, C. Sprodowski, T. Dezhdar, S. Koc, B. Veith, S. Herrman, R. Bock, K. Bothe, J. Schmidt, and R. Brendel, Highly predictive modelling of entire Si solar cells for industrial applications, *Proceedings of the 24th European Photovoltaic Solar Energy Conference, Hamburg, Germany*, p. 901 (2009).

[85] O. Krause, H. Ryssel, and P. Pichler, Determination of aluminum diffusion parameters in silicon, *J. Appl. Phys.* **91**, 5645 (2002).

[86] Y. J. Lee, J. von Boehm, M. Pesola, and R. M. Nieminen, First principles study of oxygen defects in silicon, *Phys. Rev. B.* **65, 8**, 085205 (2002).

[87] J. Schmidt, J. D. Moschner, J. Henze, S. Dauwe, and R. Hezel, Recent progress in the surface passivation of silicon solar cells using silicon nitride, *Proceedings of the 19th European Photovoltaic Solar Energy Conference, Paris, France* (2004).

[88] S. Dauwe, *Low-Temperature Surface Passivation of Crystalline Silicon and its Application to the Rear Side of Solar Cells*, PhD thesis, University of Hannover (2004).

[89] T. Lauinger, J. D. Moschner, A. G. Aberle, and R. Hezel, Optimization and characterization of remote plasma-enhanced chemical vapor deposition silicon nitride for the passivation of p-type crystaline silicon surfaces, *J. Vac. Sci. Technol. A* **16**, 530 (1998).

[90] D.L. Smith, *Thin-film depostion: Principles and practice*, McGraw Hill, Inc. (1995).

[91] B. Hoex, J. Schmidt, R. Bock, P. P. Altermatt, M. C. M. van de Sanden, and W. M. M. Kessels, Excellent passivation of highly doped p-type Si surfaces by the negative-charge-dielectric Al_2 O_3, *Applied Physics Letters* **91**(11), 112107 (2007).

[92] E. Langereis, J. Keijmel, M. C. M. van de Sanden, and W. M. M. Kessels, Surface chemistry of plasma-assisted atomic layer deposition of Al_2O_3 studied by infrared spectroscopy, *Appl. Phys. Lett.* **92**, 231904 (2008).

[93] B. E. Deal and A. S. Grove, General relationship for the thermal oxidation of silicon, *J. Appl. Phys.* **36, Nr. 12**, 3770–3779 (1965).

[94] E. Cartier and J. H. Stathis, Hydrogen-induced degradation of the Si/SiO_2 structure, *MICROELECTRON. ENG* **28**, 3–10 (1995).

[95] L. P. Johnson, K. R. McIntosh, B. S. Richards, H. Jin, B. Paudyal, and E. Klampaftis, Characterisation of the Si-SiO_2 interface after humidity exposure, *Proceedings of the 44th ANZSES CONFERENCE* (2006).

[96] T. C. Kho, K. R. McIntosh, J. Tan, A. F. Thompson, and F. W. Chen, Removal of hydrogen and deposition of surface charge during rapid thermal annealing, *Proceedings of the 33rd IEEE Photovoltaic Specialists Conference, San Diego, USA* (2008).

[97] L. Tsetseris and S. T. Pantelides, Migration, incorporation, and passivation reactions of molecular hydrogen at the Si/SiO_2 interface, *Phys. Rev. B* **70**, 245320 (2004).

[98] A. F. Thomson and K. R. McIntosh, Degradation of oxide-passivated boron-diffused silicon, *Appl. Phys. L* **95**, 052101 (2009).

[99] A. Bentzen, A. Ulyashin, A. Suphellen, E. Sauar, D. Grambole, D. N. Wright, E. S. Marstein, B. G. Svensson, and A. Holt, Surface passivation of silicon solar cells by amorphous silicon/silicon nitride dual layer, *Proceedings of the 15th International Photovoltaic Science & Engineering Conference, Shanghai, China* (2005).

[100] H. Plagwitz, Y. Takahashi, B. Terheiden, and R. Brendel, Amorphous Si/SiN double layers: A low-temperature passivation method for diffused phosphorus as well as boron emitters:, *Proceedings of the 21st European Photovoltaic Solar Energy Conference, Dresden, Germany* (2006).

[101] H. Fujiwara, Y. Toyoshima, M. Kondo, and A. Matsuda, Interface-layer formation mechanism in a-Si:H thin-film growth studied by real-time spectroscopic ellipsometry and infrared spectroscopy, *Phys. Rev. B* **60**, 13598 (1999).

[102] J. Schmidt, A. Merkle, R. Bock, P. P. Altermatt, A. Cuevas, B. Hoex N.-P. Harder, R. van de Sanden, E. Kessels, and R. Brendel, Progress in the surface passivation of silicon solar cells, *Proceedings of the 23rd European Photovoltaic Solar Energy Conference,Valencia, Spain*, p. 974 (2008).

[103] F. W. Chen, T. Li, and J. E. Cotter, PECVD silicon nitride surface passivation for high-efficiency n-type silicon solar cells, *Appl. Phys. Lett.* **88**, 263514 (2006).

[104] S. De Wolf, G. Agostinelli, G. Beaucarne, and P. Vitanov, Influence of stoichiometry of direct plasma-enhanced chemical vapor deposited SiN_x films and silicon substrate surface roughness on surface passivation, *J. Appl. Phys.* **97**, 063303 (2005).

[105] B. Bitnar, *Oberflächenpassivierung von kristallinen Silizium Solarzellen*, PhD thesis, University of Konstanz (1998).

[106] S. Bowden, D. S. Kim, C. Honsberg, and A. Rohatgi, Rapid thermal processing for front and rear contact passivation, *Proceedings of the 29th IEEE Photovoltaic Specialists Conference, New Orleans, USA*, p. 410 (2002).

[107] S. Narasimha and A. Rohatgi, Optimized aluminum back surface field techniques for silicon solar cells, *Proceedings of the 26th IEEE Photovoltaic Specialists Conference, Anaheim, USA*, p. 63 (1997).

[108] C. J. J. Tool, P. Manshanden, A. R. Burgers, and A. W. Weeber, Higher efficiency for thin multi crystalline silicon solar cells by improving the rear surface passivation, *Proceedings of the 29th IEEE Photovoltaic Specialists Conference, New Orleans, USA*, p. 1P2.3 (2002).

[109] M. Rauer, C. Schmiga, M. Hermle, and S. W. Glunz, Passivation of screen-printed aluminum-alloyed emitters for back junction n-type silicon solar cells, *Proceedings of the 24rd European Photovoltaic Solar Energy Conference, Hamburg, Germany* (2009).

[110] M. J. Kerr, J. Schmidt, A. Cuevas, and J. H. Bultman, Surface recombination velocity of phosphorus-diffused silicon solar cell emitters passivated with plasma enhanced chemical vapor deposited silicon nitride and thermal silicon oxide, *J. Appl. Phys.* **89 (7)**, 3821 (2001).

[111] A. Cuevas, P. A. Basore, G. Giroult-Matlakowski, and C. Dubois, Surface recombination velocity of highly doped n-type silicon, *J. Appl. Phys* **80 (6)**, 3370 (1996).

[112] A. Cuevas, M. Stuckings, J. Lau, and M. Petravic, The recombination velocity of boron diffused silicon surfaces, *Proceedings of the 14th European Photovoltaics Specialists Conference, Barcelona, Spain*, p. 2416 (1997).

[113] H. Plagwitz, M. Nerding, N. Ott, H. P. Strunk, and R. Brendel, Low-temperature formation of local al contacts to a-Si:H-passivated Si wafers, *Prog. In Photovolt.: Research and Applications* **12**, 47 (2004).

[114] C. Schmiga, M. Hermle, and S. Glunz, Towards 20% efficient n-type silicon solar cells with screen-printed aluminium-alloyed rear emitter, *Proceedings of the 23rd European Photovoltaic Solar Energy Conference, Valencia, Spain*, p. 982 (2008).

[115] T. Fuyuki, H. Kondo, T. Yamazaki, Y. Takahashi, and Y. Uraoka, Photographic surveying of minority carrier diffusion length in polycrystalline silicon solar cells by electroluminescence, *Appl. Phys. Lett.* **86**, 262108 (2005).

[116] K. Bothe, P. Pohl, J. Schmidt, T. Weber, P. Altermatt, B. Fischer, and R. Brendel, Electroluminescence imaging as an in-line characterisation tool for solar cell production, *Proceedings of the 21st European Photovoltaic Solar Energy Conference, Dresden, Germany*, 597–600. WIP, Munich (2006).

[117] P. Engelhart, S. Hermann, T. Neubert, H. Plagwitz, R. Grischke, R. Meyer, U. Klug, A. Schoonderbeek, U. Stute, and R. Brendel, Laser ablation of SiO_2 for locally contacted Si solar cells with ultra-short pulses, *Prog. Photovolt.* **15**, 521 (2007).

[118] P. Engelhart, A. Teppe, A. Merkle, R. Grischke, R. Meyer, N.-P. Harder, and R. Brendel, The RISE-EWT solar cell – a new approach towards simple high efficiency silicon solar cells, *Proceedings of the 15th International Photovoltaic Science and Engineering Conference, Shanghai, China*, p. 802 (2005).

[119] R. Brendel, Modeling solar cells with the dopant-diffused layers treated as conductive boundaries, *Prog. In Photovolt.: Research and Applications, (in press)* (2010).

[120] B. Fischer, *Loss analysis of crystalline silicon solar cells using photoconductance and quantum efficiency measurements*, PhD thesis, University of Konstanz (2003). (Cuvillier Verlag) Chapter 4.

[121] A. Cuevas, P. A. Basore, G. Giroult-Matlakowski, and C. Dubois, Surface recombination velocity of highly doped n-type silicon, *J. Appl. Phys* **80 (6)**, 3370 (1996).

[122] G. Schubert, *Thick Film Metallisation of Crystalline Silicon Solar Cells Mechanisms, Models and Applications*, PhD thesis, University of Konstanz (2006).

[123] R. Bock, R. Hesse, J. Schmidt, R. Brendel, J. Maier, B. Geyer, J. Koopmann, and E. Kasper, Industrial-type n-type ALU^+ solar cells on n-type Cz silicon, *Proceedings of the 5th World Conference on Photovoltaic Energy Conversion, Valencia, Spain*, p. 1449 (2010).

[124] A. Goetzberger, B. Voß, and J. Knobloch, *Sonnenenergie: Photovoltaik*, Stuttgart: B.G. Teubner: (1997).

[125] M.A. Green. *Solar Cells.* University of New South Wales, (1992).

[126] Schlussbericht BMU Projekt. Abbildende Verlustanalyse von Solarzellen für die industrielle Fertigungskontrolle und die Ausbildung, Kurzbezeichnung LOANA (LOss ANAlysis). Förderkennzeichen 0327661, (2010).

[127] J. Isenberg and W. Warta, Realistic evaluation of power losses in solar cells by using thermographic methods, *J. Appl. Phys.* **95 (9)**, 5200 (2004).

[128] ILLUMINATED LOCK-IN THERMOGRAPHY: EXPERIMENTAL VERIFICATION OF QUANTITATIVE SHUNT ANALYSIS, K. ramspeck, p. altermatt, n.-p. harder and r. brendel, *Proceedings of the 21st European Photovoltaic Solar Energy Conference, Dresden, Germany*, p. 1471 (2006).

[129] B. Hoex, J. J. H. Gielis, M. C. M. van de Sanden, and W. M. M. Kessels, On the c-Si surface passivation mechanism by the negative-chargedielectric $Al_2\ O_3$, *J. Appl. Phys.* **104**, 113703 (2008).

[130] N. M. Terlinden, G. Dingemans, M. C. M van de Sanden, , and W. M. M. Kessels, Role of field-effect on c-si surface passivation by ultrathin (2–20 nm) atomic layer deposited $Al_2\ O_3$, *Appl. Phys. Lett.* **96**, 112101 (2010).

[131] F. Werner, B. Veith, D. Zielke, L. Kühnemund, C. Tegenkamp, M. Seibt, J. Schmidt, and R. Brendel, Improved understanding of recombination at the si/al2o3 interface, *Proceedings of the 25th European Photovoltaic Solar Energy Conference, Valencia, Spain* (2010).

[132] S. Dauwe, L. Mittelstädt, A. Metz, and R. Hezel, Experimental evidence of parasitic shunting in silicon nitride rear surface passivated solar cells, *Prog. Photovolt. Res. Appl.* **10(4)**, 271–278 (2002).

[133] M. Pawlik, Spreading resistance: A quantitative tool for process control and development, *J. Vac. Sci. Technol.* **B10**, 388 (1992).

[134] S. R. Weinzierl, R. J. Hillard, J. M. Heddleson, P. Rai-Choudhury, R. G. Mazur, and C. M. Osburn, Detection of anomalous defect-enhanced diffusion using advanced spreading resistance measurements and analysis, *J. Vac. Sci. Technol.* **B12**, 322 (1994).

[135] E. Peiner, A. Schlachetzki, and D. Krüger, Doping profile analysis in Si by electrochemical capacitance-voltage measurements, *J.Electrochem.Soc.* **142**, 576 (1995).

[136] H. von Helmholtz, Studien über elektrische grenzschichten, *Wied. Ann.* **7**, 337 (1879).

[137] L. G. Gouy, Sur la constitution de la charge á la surface d' un électrolyte, *Compt. Rend.* **149**, 654 (1909).

[138] D. L. Chapman, A contribution to the theory of electrocapillarity, *Phil. Mag.* **25**, 475 (1913).

[139] O. Stern, Zur Theorie der elektrischen Doppelschicht, *Z. Elektrochemie* **30**, 508 (1924).

[140] V. Lehmann, *Electrochemistry of Silicon*, Wiley-VCH, Weinheim, Germany (2002).

[141] H. Föll, Properties of silicon-electrolyte junctions and their application to silicon characterization, *Appl. Phys. A* **53**, 8 (1991).

[142] G. Masetti, M. Severi, and S. Solmi, Modeling of carrier mobility against carrier concentration in arsenic-, phosphorus-, and boron-doped silicon, *IEEE Transactions on Electron Devices* **30**, 764 (1983).

List of Publications

Refereed journal papers

1. R. Bock, J. Schmidt, and R. Brendel, Effective passivation of highly aluminum-doped p-type silicon surfaces using amorphous silicon, *Appl. Phys. Lett.* **91**, 112112 (2007).
2. R. Bock, J. Schmidt, R. Brendel, H. Schuhmann, and M. Seibt, Electron microscopy analysis of crystalline silicon islands formed on screen-printed aluminum-doped p-type silicon surfaces, *J. Appl. Phys.* **104**, 043701 (2008.).
3. R. Bock, J. Schmidt, and R. Brendel, n-type silicon solar cells with surface-passivated screen-printed aluminium-alloyed rear emitter, *Phys. Stat. Sol.* (RRL) **2**, No. 6, 248-250 (2008).
4. R. Bock, S. Mau, J. Schmidt, and R. Brendel, Back-junction back-contact n-type silicon solar cells with screen-printed aluminum-alloyed emitter, *Appl. Phys Lett.*, **96**, 263507 (2010).
5. R. Bock, J. Schmidt, S. Mau, B. Hoex, and R. Brendel, The ALU+ concept: n-type silicon solar cells with surface-passivated screen-printed alluminum-alloyed rear emitter, *IEEE Transactions on Electron Devices*, **57** No. 8, 1966, (2010).
6. R. Bock, P. P. Altermatt, J. Schmidt, and Rolf Brendel, Formation of aluminum-oxygen complexes in highly aluminum-doped silicon, *Semiconductor Science and Technology*, **25**, 105007, (2010).
7. B. Hoex, J. Schmidt, R. Bock, P. P. Altermatt, M. C. M. van de Sanden, and W. M. M. Kessels, Excellent passivation of highly doped p-type Si surfaces by the negative-charge-dielectric Al_2O_3 *Appl. Phys Lett.*, **91**, 112107, (2007).
8. J. Schmidt, N. Theiman. R. Bock, and R. Brendel, Recombination lifetimes in highly-aluminum doped silicon, *J. Appl. Phys.*, **106**, 093707, (2009).

9. D. Hinken, K. Bothe, R. Bock, and R. Brendel Determination of the base dopant concentration of large-area crystalline silicon solar cells, *IEEE Transactions on Electron Devices*, **57** No. 11, 2831, (2010).

10. C. Mader, R. Bock, J. Schmidt, and R. Brendel, Formation of highly aluminum-doped *p*-type silicon regions by in-line high-rate evaporation, *Solar Energy Materials and Solar Cells*, submitted, (2010).

Papers presented at international conferences

1. R. Bock, J. Schmidt, and R. Brendel, Effective surface passivation of screen-printed Al-doped p^+-emitters for *n*-type c-Si solar cells using a-Si, *Technical Digest of 17th International Photovoltaic Science and Engineering Conference, Japan, Fukuoka*, 251, (2007).

2. R. Bock, J. Schmidt, R. Brendel, H. Schuhmann, and M. Seibt, Electron microscopy analysis of silicon islands and line structures formed on screen-printed al-doped p^+-surfaces, *Proceedings of the 33th IEEE Photovoltaic Specialists Conference, San Diego, USA*, Document 154, (2008).

3. R. Bock, Pietro P. P. Altermatt, and J. Schmidt, Accurate extraction of doping profiles from electrochemical capacitance voltage measurements, *Proceedings of the 23st European Photovoltaic Solar Energy Conference, Valencia, Spain*, 1510, (2008).

4. R. Bock, J. Schmidt, S. Mau, B. Hoex, E. Kessels, and R. Brendel The ALU^+ concept: *n*-type silicon solar cells with surface-passivated screen-printed aluminum-doped rear emitter, *Proceedings of the 34th IEEE Photovoltaic Specialists Conference, Philadelphia, USA*, 000030, (2009).

5. R. Bock, R. Hesse, J. Schmidt, R. Brendel, J. Maier, B. Geyer, J. Koopmann, E. Kasper, Industrial-type *n*-type ALU^+ solar cells on *n*-type Cz silicon, *Proceedings of the 5th World Conference on Photovoltaic Energy Conversion, Valencia, Spain*, 1449, (2010).

6. C. Schmiga, H. Nagel, R. Bock, J. Schmidt and R. Brendel, Advances in the manufacturing of n-type silicon solar cells with screen-printed aluminium-alloyed rear emitter, *Proceedings of the 21st European Photovoltaic Solar Energy Conference, Dresden, Germany*, 617, (2006)

7. P.P. Altermatt, H. Plagwitz, R. Bock, J. Schmidt, R. Brendel, M.J. Kerr, and A. Cuevas, The surface recombination velocity at boron-doped emitters: Comparison between various passivation techniques, *Proceedings of the 21st European Photovoltaic Solar Energy Conference, Dresden, Germany*, 647, (2006).

8. C. Voyer, T. Buettner, R. Bock, D. Biro, and R. Preu, Microscopic homogeneity of emitters formed using in-line diffusion and sprayed phosphoric acid as the dopant source, *Technical Digest of 17th International Photovoltaic Science and Engineering Conference*, Japan, Fukuoka, 759, (2007).

9. J. Schmidt, K. Bothe, R. Bock, C. Schmiga, R. Krain, and R. Brendel, *N*-type silicon – the better material choice for industrial high-efficiency solar cells?, *Proceedings of the 22st European Photovoltaic Solar Energy Conference, Milan, Italy*, 998, (2007).

10. J. Schmidt, A. Merkle, R. Bock, P. P. Altermatt, A. Cuevas, N.-P. Harder, B. Hoex, R. van de Sanden, E. Kessels, and R. Brendel, Progress in the surface passivation of silicon solar cells, *Proceedings of the 23st European Photovoltaic Solar Energy Conference, Valencia, Spain*, 974, (2008).

11. I. Köhler, W. Stockum, A. Meijer, O. Doll, M. James, E. Plummer, P. Brookes, K. Patterson, H. Qu(, R. Bock, S. Gatz, M. Prütz, B. Terheiden, and H. Plagwitz, New inkjet solution for direct printing of local diffusion barriers on solar cells, *Proceedings of the 23st European Photovoltaic Solar Energy Conference, Valencia, Spain*, 1352, (2008).

12. J. Schmidt, N. Thiemann, R. Bock, and R. Brendel, Lifetimes in aluminium-doped silicon, *Proceedings of the 34th IEEE Photovoltaic Specialists Conference, Philadelphia, USA*, 001732, (2009).

13. M. Kessler, R. Bock, B. Wolpensinger, and N.-P. Harder, Characterization and implications of the Boron Rich Layer resulting from open tube liquid source BBr_3 boron diffusion processes, *Proceedings of the 34th IEEE Photovoltaic Specialists Conference, Philadelphia, USA*, 001556, (2009).

14. P.P. Altermatt, S. Steingrube, Y. Yang, C. Sprodowski, T. Dezhdar, S. Koc, B. Veith, S. Herrman, R. Bock, K. Bothe, J. Schmidt, and R. Brendel, Highly predictive modeling of entire Si solar cells for industrial applications, *Proceedings of the 24st European Photovoltaic Solar Energy Conference, Hamburg, Germany*, 901, (2009).

15. J. Schmidt, F. Werner, B. Veith, D. Zielke, R. Bock, V. Tiba, P. Poodt, F. Roozeboom, A. Li, A. Cuevas, and R. Brendel, Industrially relevant Al_2O_3 deposition techniques for the surface passivation of Si solar cells, *Proceedings of the 5th World Conference on Photovoltaic Energy Conversion, Valencia, Spain*, 1130, (2010).

Invited Presentations

1. R. BOCK, Effektive Passivierung von siebgedruckten Al-p^+ Emitteroberflächen mit a-Si, *Silicon-FOREST Workshop 2007*, Falkau, (2007).
2. R. BOCK, Elektronenmikroskopische Untersuchung siebgedruckter Al-p^+ Oberflächen, *Silicon-FOREST Workshop 2008*, Falkau, (2008).
3. R. BOCK, Passivierung von siebgedruckten Al-p^+ Emitteroberflächen mit a-Si, *Kolloquium am Institut für Physikalische Elektronik Universität Stuttgart*, (2007).

Patent Applications

1. R. BOCK, J. SCHMIDT, Silicon solar cell comprising a passivated p-type surface and method for Producing the same, International Patent Application WO2010/003784 A4.
2. C. MADER, F. HEINEMEYER, R. BOCK, Verfahren zum Metallisieren eines Halbleitersubstrates, Verfahren zum Herstellen einer Solarzelle sowie Metallisierungsvorrichtung, DE Patentanmeldung 10 2009 024 472.9.

Awards

R. BOCK, Best Student Presentation Award, The ALU$^+$ concept: n-type silicon solar cells with surface-passivated screen-printed aluminum-doped rear emitter, *34th IEEE Photovoltaic Specialists Conference, Philadelphia, USA*, 2009.

Danksagung

Abschließend bedanke ich mich bei allen Menschen, die zum Gelingen dieser Arbeit beigetragen haben. Besonderer Dank gilt:

Prof. Dr. Rolf Brendel für die Möglichkeit diese Arbeit am ISFH durchführen zu können, für das Vertrauen in mich und die Freiheit, die er mir während der Arbeit einräumte und für die stets zügige Durchsicht meiner Publikationen.

Prof. Dr. Jan Schmidt für seine ausgezeichnete wissenschaftliche Betreuung, die hilfreichen Diskussionen und Anregungen sowie für die geduldige Unterstützung beim Anfertigen und Korrekturlesen der zahlreichen Publikationen. Die Freiheit, die er mir bei bei der Durchführung aller Vorhaben einräumte, hat ebenfalls maßgeblich zum Gelingen dieser Arbeit beigetragen. Auch die hervorragende Freizeitgestaltung auf diversen Workshops im Schwarzwald soll hier nicht unerwähnt bleiben.

Prof. Dr. Rolf Haug für die freundliche Übernahme des Korreferats.

Susanne Mau für die Einführung in viele Prozesstechniken sowie für die unermüdliche Unterstützung beim Prozessieren von unzähligen Solarzellen und Proben. Ohne den besonderen Einsatz von Susanne, hätten viele Ergebnisse dieser Arbeit nicht realisiert werden können.

Christian Schmiga für die ausführliche Einführung in die Siebdrucktechnik.

Martin Wolf und Arne Schmidt, die mich bei Messungen von Solarzellen tatkräftig unterstützt haben und sich auch am Wochenende nicht zu schade waren Messprobleme aus dem Weg zu räumen. Ich muss ihnen auch dafür danken, dass sie meine Launen im Falle eines größeren Messproblems mit Ruhe und Verstand stoisch ertragen haben.

Prof. Dr. Nils-Peter Harder für die zahlreichen fachlichen Gespräche, Tipps und Anregungen, die hier und da ein Licht haben aufgehen lassen und für die besondere Atmosphäre im Büro. Ich danke Nils auch für die Bestätigung dafür, dass eine gesunde Portion Chaos nicht a priori schlecht sein muss.

Bianca Lim für zügiges und gewissenhaftes Korrekturlesen dieser Arbeit und für den stetigen Strom an abgelaufenen Süßigkeiten.

Den Laser-Fuzzis *Till, Tobi und Peter* für die fachkundige und engagierte Laserbearbeitung meiner Solarzellen und nicht für die zweifelsohne qualifikationsfreien Kommentare.

Rene "Rönnibert" Hesse für seine Geduld und Ausdauer beim Prozessieren von Solarzellen im ALU$^+$ Projekt, die hohe Einsatzbereitschaft, den geduldigen Umgang mit Rückschlägen; und allet so, janz alljemein, wa? Ey?

Meinen Mitdoktoranden/Innen und Wissenschaftlern/Innen *Dr. Pietro Altermatt, Dr. Sonja Hermann, Dr. G, Dr. Klaus Ramspeck, Dr. Peter Engelhart, Dr. Peter Pohl, Dr. Andreas Wolf, Dr. Uli Eitner, David Hinken, Jens Müller, Christoph Mader, Michael Kessler, Christian Ulzhöfer, Marco Ernst, Felix Haase, Bianca Lim, Herr Gatz, Stephan Eideloth, Sandra Herlufsen, Ralf Gogolin, Nils Thieman, Florian Werner und Dr. Rafa Ferre* und allen weiteren Mittarbeitern für die hervorragende Zusammenarbeit und das positive, humorvolle und *gesellige* Arbeitsklima am ISFH.

Der *Japan Research Group* aus Fukuoka 2007 (*Klaus, Christoph, Felix, Dr. G*): Arigatoo gozaimasu!

Der *First Aid Research Group* aus Valencia 2010 (*Rafa, Dr. G, und Jens*) für die hervorragende, verantwortungsvolle und gewissenhafte medizinische Betreuung.

Dr. Peter Engelhart für die mehr oder minder fundierten Börsentipps. DAN-KE!

Dr. Carsten Hampe für die vielen Gespräche zu diversen Themen auch außerhalb von Solarzellen und natürlich für die notwendige Verpflegung.

Und *Willy* für … Er war stets bemüht, den an ihn gestellten Anforderungen gerecht zu werden und war stets pünktlich. Sein geselliges Wesen hat zur Verbesserung des allgemeinen Arbeitsklimas beigetragen. …

DANKE SCHÖN!

Persönliche Daten

Name	Robert Bock
Anschrift	Wettorstr. 19, 31785 Hameln
Geburtsdatum	19. Januar 1977
Nationalität	deutsch
Familienstand	verheiratet

Schulbildung

1984 - 1988	Grundschule in Wildfurt
1988 - 1989	Blücherschule (Grundschule) in Gütersloh
1989 - 1998	Anne Frank Schule (Gesamtschule) in Gütersloh Abschluss der allgemeinen Hochschulreife im Juni 1998

Ersatzdienst

September 1998 - Oktober 1999	Zirkel e. V. in Gütersloh

Universitätsausbildung

Oktober 1999 - Juli 2002	Christian-Albrechts-Universität zu Kiel Studium der Elektrotechnik
Oktober 2002 - Juni 2006	Christian-Albrechts-Universität zu Kiel Studium der Materialwissenschaft Diplom Ingenieur Materialwissenschaft im Juni 2006

Anstellung

seit Juli 2006	Institut für Solarenergieforschung (ISFH) Hameln/Emmerthal: Wissenschaftlicher Mitarbeiter im Bereich Materialforschung